Quantitative Estimation Method of Deep Sea Cobalt-rich Manganese Crust Distribution using Underwater Robots

A Thesis
submitted in partial fulfilment of the requirements for the degree of
Doctor of Philosophy

by

Umesh Neettiyath
(Student Number: 16899013)

Kyutech
Kyushu Institute of Technology

Graduate School of Life Science and Systems Engineering
Kyushu Institute of Technology
Japan
February, 2020

Quantitative Estimation Method of Deep Sea Cobalt-rich Manganese Crust Distribution using Underwater Robots

by

Umesh Neettiyath

Submitted to the Graduate School of Life Science and Systems Engineering
on December, 2019, in partial fulfillment of the
requirements for the degree of
Doctor of Philosophy

Abstract

A method to efficiently map the distribution of Cobalt-rich Manganese Crusts (Mn-crust) using data collected by autonomous underwater vehicles and remotely operated vehicles is developed. Volumetric measurements of Mn-crusts are made using a high-frequency sub-surface sonar and a 3D visual mapping instrument mounted on these vehicles. This thesis proposes a fully automated algorithmic approach to estimate Mn-crust distribution by combining the continuous sub-surface thickness measurements with the exposed surface area identified in the 3D maps. This method is applied to data collected from field surveys in the deep sea and the results are validated using physical samples.

Manganese crusts (Mn-crust) are a type of mineral deposit commonly found on seamounts and guyots at depths varying from $800\,m$ to $5500\,m$. They are precipitated from ambient seawater creating deposits up to $250\,mm$ in thickness. Mn-crusts are rich in Cobalt, Nickel, other rare minerals and rare earth metals, making it a potential target for deep sea mining. Since they contain the historical record of millions of years of ocean conditions and fossils of ancient crustaceans, it is of high scientific interest.

The present methods of studying Mn-crusts by collecting physical samples provides a low spatial resolution of the order of several km and cannot thus capture the local variability of its distribution. Since the deposits are thin compared to the typical resolutions of sub-bottom sonars, in-situ surveys using dedicated sensors are required to accurately measure the Mn-crust thickness. Towed camera surveys and ROV video feeds have been used by researchers to visually confirm the presence of Mn-crusts, but cannot be used to make accurate thickness or volume measurements. Automated methods for classification is suitable for analyzing large volumes of seafloor data to create estimates of Mn-crust coverage. 3D colour seafloor maps are more suitable to distinguish the unique texture and shape of Mn-crust deposits. The proposed method creates volumetric distribution estimates of Mn-crusts using data collected using a high-frequency sub-surface sonar and a 3D visual mapping instrument mounted on an underwater robot suitable for surveying Mn-crusts.

The proposed sensor fusion method consists of 3 algorithms for measuring the percentage cover (lateral coverage), thickness and unit mass coverage (mass of crust per unit area) of Mn-crusts respectively and can be scaled to large regions of seafloor. 3D colour reconstructions made by the visual mapping instrument is analyzed by using a Support Vector Machine classifier to identify Mn-crusts and other seafloor types present and estimate a percentage cover value. In the areas covered with exposed Mn-crust, the sub-surface sonar data is analyzed to measure the continuous thickness of Mn-crust. These thickness measurements are then extrapolated into the entire region containing exposed Mn-crust. From the extrapolated thickness map, the total volume of crust is calculated and the mass coverage estimates are calculated by integrating the thickness values over an area of influence. The density of Mn-crusts measured from samples is used in the mass calculations.

This method is applied to field data collected from three expeditions at Takuyo Daigo seamount in the northwestern Pacific ocean at depths ranging from $1350\,m$ to $1600\,m$. The total transect lengths add to about $11\,km$ with $12,510\,m^2$ mapped. The results showed that $52\,\%$ of the surveyed area is covered by Mn-crusts with a mean thickness of $69.6\,mm$. The mean Mn-crust occurrence is $69.6\,kg/m^2$ with a maximum of $204\,kg/m^2$ in the mapped region. In order to validate the proposed approach, the results of thickness were compared to Mn-crust samples retrieved from the surveyed area by researchers. The results generated by the method agree with estimates made from samples retrieved from the area, and shows more detailed distribution patterns. By looking at the variability of crust coverage in different transects, it is seen that the coverage of crust can vary by a large margin. Therefore, a continuous in-situ survey is required to accurately assess the distribution of Mn-crust over large regions. The proposed method is therefore effective for efficiently estimating Mn-crust distributions and inventories at hectare scale areas.

This is the first method suitable for estimating volumetric distribution estimates of Mn-crust for hectare-scale or larger areas at centimeter resolution. A method for sensor fusion using a 3D map and secondary sensor data and a method for high accuracy classification of seafloor 3D colour point clouds are developed. The information generated can provide valuable insights into the study of Mn-crust distribution, the ocean processes of Mn-crust formation and inputs for making policy decisions regarding deep sea mining and planning future courses of action.

Keywords

Cobalt-rich Manganese Crust (Mn-crust), Deep sea mining, Autonomous Underwater Vehicles (AUV), Support Vector Machines (SVM), Machine Learning, Volumetric estimation, Large area surveys, Remotely Operated Vehicles (ROV), Robotic surveys, Underwater robots, Ocean floor mapping, 3D mapping.

Contents

List of Figures

List of Tables

Nomenclature

ASV	Autonomous Surface Vessel
AUV	Autonomous Underwater Vehicle
CCZ	Clarion-Clipperton Zone
CSD	Cross Spectral Density
EEZ	Exclusive Economic Zone
JAMSTEC	Japan Agency for Marine Earth Science and Technology
Mn-crust	Cobalt-rich Manganese Crust, Ferromanganese Crust
Mn-nodules	Polymetallic nodules, Ferromanganese Nodules
NOC	National Oceanography Centre, UK
ROV	Remotely Operated Vehicle
SVM	Support Vector Machine

Notation

δ	Error
A	Area of seafloor
Ψ	Percentage cover of Mn-crust
t	Thickness of Mn-crust
M	Total mass of Mn-crust
Λ	Mass coverage per unit area of Mn-crust
ρ	Density of Mn-crust
ν	Speed of sound in Mn-crust

Chapter 1

Introduction

1.1 Motivation

The immensity and grandiosity of the ocean has amazed human beings since ancient times. People worshipped ocean as god since it was incomprehensible to their minds. It is interesting to note that even now, with all the advancement of technology, we know very little about this magnificent blue world.

From what we know, the ocean covers 71% of the earth's surface area and holds 97% of water present on earth. The longest mountain range, most active volcanoes, the highest peak (when measured w.r.t. the base) and the largest among animals are inside this. Nations around the world rely on the ocean for food, transportation, oil, communications and entertainment. Behind the scenes, the ocean play an even bigger role in sustaining human life. Algae in ocean absorbs carbon dioxide and produces about half the oxygen we breath. Top 10 meters of these waters hold as much heat as the atmosphere and controls the climate around the world and its balance (or the lack of it).

Still, a large portion of the ocean remains unexplored; only around 10% of seafloor has been surveyed by shipboard sonar systems (Becker et al. 2009). We have higher resolution maps of the moon than we have of the deep seabed XPRIZE (2019). Entire mountains have been discovered in the sea which previously unknown Wessel et al. (2010). Thousands of ships have sank since ancient times; a large number of them were never recovered (Michel & Ballard n.d.). Life on earth was thought to be impossible without oxygen until large colonies of animals were discovered around hydrothermal vents (Hashimoto et al. 2001, Ramirez-Llodra et al. 2007). On average, two new species of animals are getting discovered every month (Ramirez-Llodra et al. 2007). More and more mineral resources, petroleum and natural gas reserves are being identified on the ocean floor on a regular basis. Figure 1-1 shows an illustration of the earth's crust which indicates the diverse nature of ocean bed.

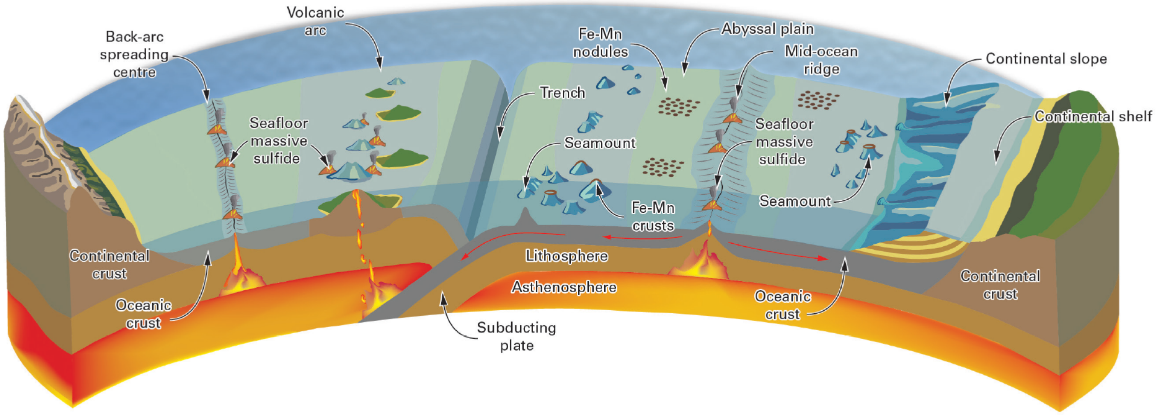

Figure 1-1: A cross-section through the Earth's crust showing the different types of plate boundary, the topography of the ocean floor and the distribution of the major metal-rich deep-ocean mineral deposits. Image: Ian Longhurst (Copyright British Geological Survey © UKRI 2018) is licensed under CC-BY 3.0 Lusty & Murton (2018).

The stunning lack of knowledge regarding the oceanic environments is a result of the challenging nature of this environment. Human divers cannot dive beyond a few hundred meters, considering the extreme cases. The pressure increases with depth specially built high pressure containers are needed which get bulkier as the depths increase. The seawater and winds corrode metals faster and damages equipment. Electromagnetic waves get attenuated fast making radio communication impossible in deep waters. The fastest wireless communication uses acoustic waves giving a few kbps of bandwidth at best. Ships and specially built underwater vehicles and sensors are needed for exploring the deep sea, which are very expensive. Surveys are therefore limited to a few hours per day and a few days per year and is always at the mercy of the fast changing weather of the ocean.

1.2 Deep sea mineral deposits

The challenging and hard to access deep seabed, which was once thought to be full of monsters was later revealed to be a hotbed of resources. As seen in Fig. 1-1, the deep seafloor, which is defined as depths exceeding 200 m, is an active landscape with volcanoes, tectonic plate boundaries, and relatively undisturbed seamounts and plains. This complex geomorphology of the seabed produces a wide variety of seabed containing different types of mineral deposits (Micallef et al. 2018).

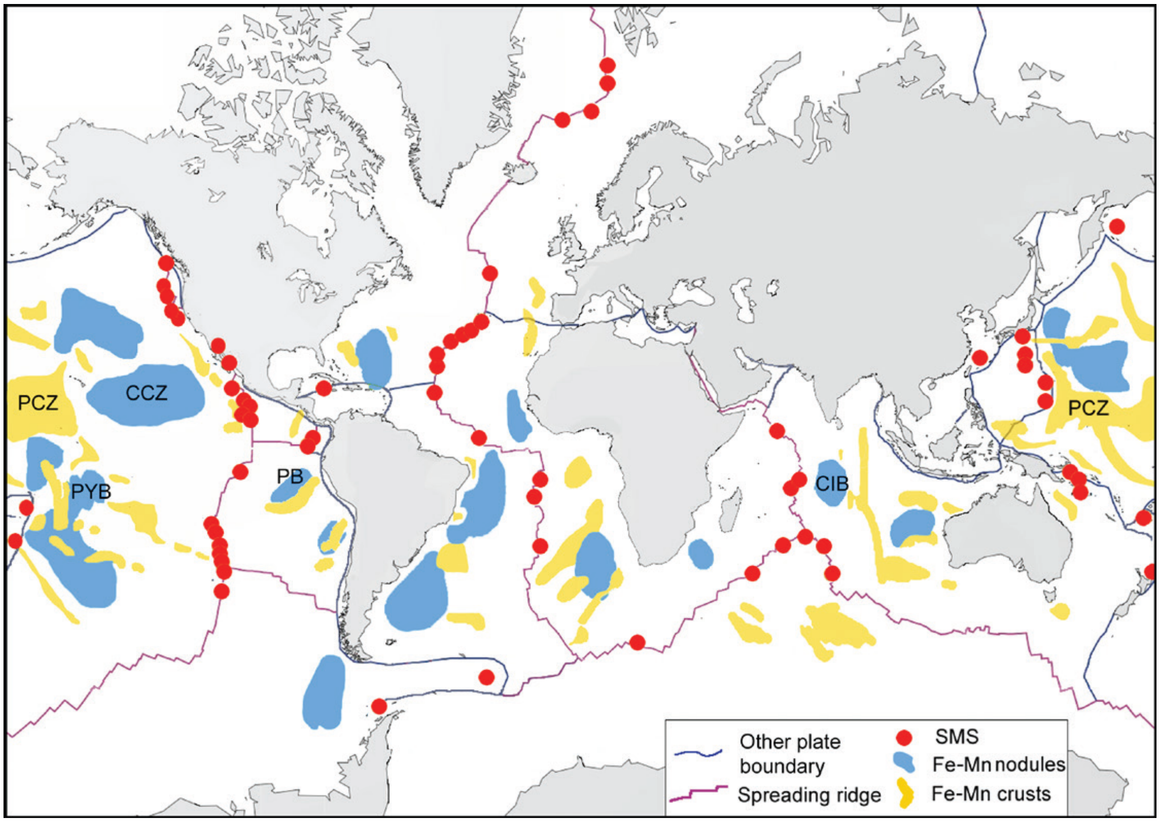

Figure 1-2: Global distribution of the three primary classes of metal-rich deep-ocean mineral deposits: seafloor massive sulfides (SMS); ferromanganese (Fe–Mn) nodules; and ferromanganese (Fe–Mn) crusts. Spreading ridges and other plate boundaries are shown. Abbreviations: CCZ = Clarion–Clipperton Zone; CIB = Central Indian Ocean Basin; PB = Peru Basin; PCZ = Prime Crust Zone; PYB = Penrhyn Basin. Map created using the NOAA National Geophysical Data Center and redrawn from multiple sources, including Murton et al. (2000), Beaulieu et al. (2013), and Hein et al. (2013). Copyright British Geological Survey, National Oceanography Centre ©UKRI 2018. Image from Lusty & Murton (2018) is licensed under CC-BY 3.0

Weathering from continents accumulated on the seabed over millions of years gives rise to the seabed deposits close to continental shelves, whereas plate tectonics and minerals from the earth's crust and mantle are responsible for the farther and deeper deposits (Lusty & Murton 2018). Recently, researchers of University of Tokyo has discovered a huge accumulation of rare earth metal deposits in the Pacific Ocean (Takaya et al. 2018). Gas hydrates and methane cold seeps are other deep sea deposits (Wakita 2010). However, three types of mineral deposits are of high interest to the academia, the industry and governments. These are seafloor massive sulfides, ferromanganese nodules (Mn-nodules) and ferromanganese crusts (Mn-crust). Figure 1-2 shows the distribution of these minerals around the world. They are distinct from each other in the methods of formation, compostion, geology, exploration challenges and economic potential.

Metal rich fluids seep out from the seafloor in tectonically active areas forming hydrothermal vents or chimneys (Halbach et al. 1993). These get deposited in nearby areas forming deposits which grow at a fast rate being replenished from below the earth's crust. Although they were discovered only in 1977 (Corliss et al. 1979), the research interest grew and several sites were found around the world. They host a very active benthic ecosystem under extreme conditions furthering the interest of biologists and other researchers (Bodenmann, Thornton, Nakajima & Ura 2017, Thornton et al. 2015, Yoshino et al. 2018).

Minerals in the seawater precipitate on a hard nucleus such as a small piece of rock, bone or old mineral deposit fragment, potato-like structures, rich in minerals are formed over millions of years. They are called ferromanganese nodules or polymetallic nodules (Mn-nodules). They are variable in sizes and shapes with dimensions ranging from 1 cm to 12 cm in diameter (Lusty & Murton 2018). A hypothesis suggests that Mn-nodules are formed by absorption of Mn by nodule substance, which is subsequently oxidized by bacteria resulting in a nodule matrix. They are formed on flat seafloor basins at depths exceeding 4000 m (Weydert 1985, Bunchuk et al. 1995, Kalyan et al. 2017).

Cobalt-rich manganese crusts (Mn-crusts) are formed in a process similar to Mn-nodules formation, but on existing seabed rock formations around seamounts. They are discussed in detail in the following section.

Metals such as manganese, cobalt, copper, aluminium, zinc, nickel and lithium are uniquely important in sustainable technologies such as solar cells, greener smart phones and batteries. Table 1.1 below summarizes applications of important minerals available in the seabed. The richness of minerals in these deposits have sparked interest in commercially exploiting them (Hein et al. 2013). The efforts in this direction, although started in 1970s, has been slow. Factors such as the availability of metals from land based mines, increasing costs and ecological concerns delayed the development of deep sea mining and exploration. Recently, a number of issues such as child labor in mining communities in undeveloped countries, population growth, political tensions and high demand for minerals caused a renewed interest in deep sea minerals.

Table 1.1: Uses of important minerals obtained by deep sea mining

Mineral	**Uses**
Manganese (Mn)	Construction industry (Sulfur fixing, Deoxidizing, Alloying properties with low-cost production)
Iron (Fe)	Steel manufacturing Various alloys
Cobalt (Co)	Production of aircraft parts and super alloys (high temperature resistance) Cathode in Li-ion batteries
Rare earth elements (Yb, Ym etc.)	Green/carbon-reducing technologies Energy efficient lighting, Catalysis
Copper (Cu)	Electricity, Communication
Silver (Ag)	Electronic gadgets, batteries, jewellery
Gold (Au)	Jewellery, Electricity as alloys
Zinc (Zn)	Production of brass, bronze, paint Galvanizing iron
Tin (Sn)	Component of solder in high-tech industries (smart phones, laptops)

Seabed mining has several advantages over terrestrial mining. They have higher ore grades and more minerals present than terrestrial mines. No local human population will be disturbed or displaced and permanent installations are not necessary (Lodge & Verlaan 2018).

However, the impact of seabed mining also needs to be considered before disrupting these ecosystems. Various aspects are being studied by researchers and there is a significant lack of information (Miller et al. 2018). The impacts include the permanent removal of top hard substrates, effects of sediments and wastes in the water column, noise, vibration and lights due to the mining equipment (Lodge & Verlaan 2018). Whether the seabed communities can repopulate or relocate once the activity has been completed is also a pertinent question Jones et al. (2018).

The ocean and its resources are considered to be "the common heritage of mankind" (United Nations Law of the Sea Convention). An international authority under the United Nations, called International Seabed Authority (ISA), is tasked with the responsibility of governing the deep seabed, including mining. by considering environmental, economic and other factors, they issue licenses for exploration and mining for deep sea mineral deposits to parties around the world (ISBA 2018, Lodge & Verlaan 2018, International Seabed Authority 2012).

1.3 Cobalt-rich manganese crusts

Cobalt-rich Manganese crusts (Mn-crust) are hydrogenetic deposits that form on the slopes and shoulders of seamounts and guyots in geologically stable regions. They are an important class of seafloor deposits and is considered to be the most difficult to estimate and exploit. They are also called as ferromanganese crusts or simply manganese crusts. These deposits contain Cobalt and Nickel in addition to various rare earth elements such as Tellurium and Platinum, making them a potential target for mining (He et al. 2011, Hein et al. 2013, Yeo et al. 2018). Due to the high Cobalt content, which is twice that of land based deposits, they are called Cobalt-rich crusts.

Figure 1-3 shows the mechanism of formation of Mn-crusts. The Mn-crust layer grows over millions of years by precipitation of metals and other elements dissolved in the ambient seawater (Clark et al. 2013, Usui et al. 2017, Usui & Someya 1997).

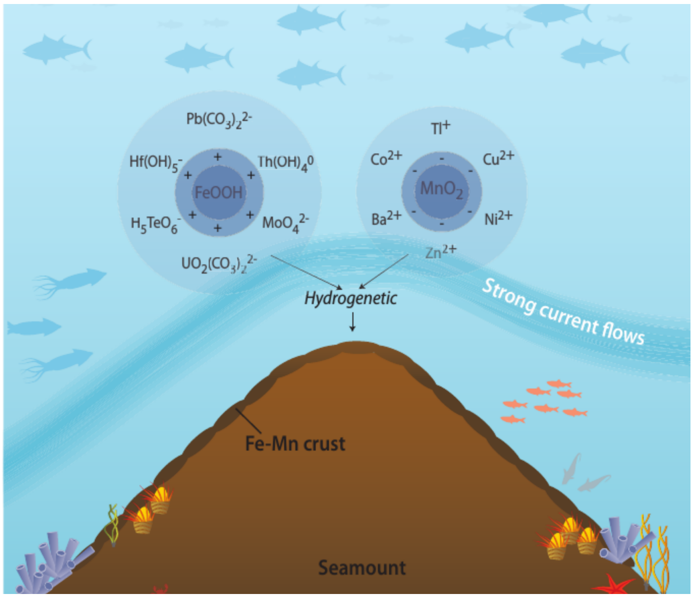

Figure 1-3: Mn-crust is formed by precipitation from the ambient seawater.Image from Clark et al. (2013) copyright Secretariat of the Pacific Community (SPC) 2013.

Manganese and iron oxides function as a platform for these dissolved minerals to get adsorbed on their surfaces and in the course of time forming Mn-crusts. The deposits spread over several hundreds of square kilometers (Usui et al. 2007, Yamazaki et al. 1994, Yamazaki & Sharma 1998, Lusty et al. 2018) and can be up to 250 mm in thickness. The depths ranges from 800 m to 2400 m, with reports of Mn-crusts found as deep as 5500 m.

However, they are also very hard to survey and exploit. Since crust is strongly attached to the base, it is more difficult to extract them. Since the thickness varies, accurate estimates cannot be made from a visual survey or acoustic multibeam surveys. This is the primary difference that makes surveys of Mn-nodules easier than Mn-crusts. Nodule surveys were conducted from shipboard multibeam surveys (Chakraborty et al. 2003)or using acoustic backscatter measured from a deep tow vehicle (Weydert 1991, 1985, 1990). Other researchers used Autonomous Underwater Vehicle (AUV) or Remotely operated vehicle based (ROV) photogrammetry and sidescan sonar imagery to estimate the distribution of seafloor polymetallic nodules (Hari et al. 2018, Schoening et al. 2017, Alevizos et al. 2018). However, these methods cannot be applied to Mn-crusts since their thickness cannot be determined

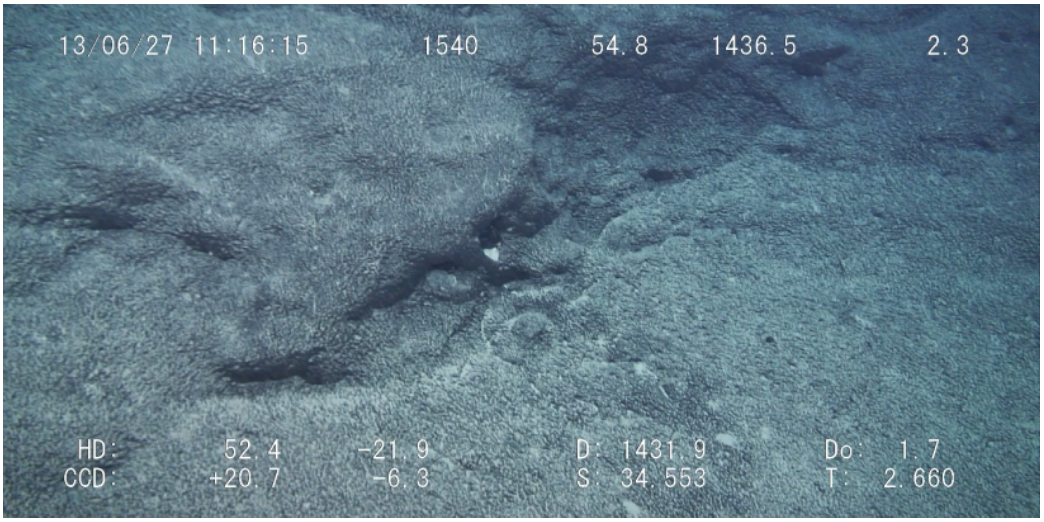

Figure 1-4: Image of Mn-crust deposits seen at Takuyo Daigo seamount in the northwestern Pacific ocean. This image is captured from the video feed of ROV Hyper-Dolphin during the NT13-13 cruise (JAMSTEC 2013).

from their surface appearance alone. Therefore, almost all current studies of Mn-crust relied on samples to estimate the tonnage Hein et al. (2013), Du, Ren, Yan, Shi, Liu & He (2017), Du, Wang, Du, Yan, Ren, Shi & Hein (2017).

1.4 Scope of the research proposed

Figure 1-5 show image of a Mn-crust sampled by an ROV. Figure 1-4 shows Mn-crusts spread on the seafloor as seen from ROV Hyper-dolphin JAMSTEC (2013). It can be seen that in order to create volumetric estimates of Mn-crust, which are essential for making informed decisions regarding mining or modeling the distribution, we need to estimate the thickness of these layers and the area of deposition.

The thickness of Mn-crust varies due to factors such as slope, seawater conditions, depth, historical landslides and sediment cover (Usui et al. 2017). This makes it difficult to make reliable thickness estimates for large areas by using the existing method of sampling. This difficulty can be overcome by in-situ measurements using sub-bottom sonars (Gaowen et al. 2005). This was first demonstrated by Thornton et al. (2009).

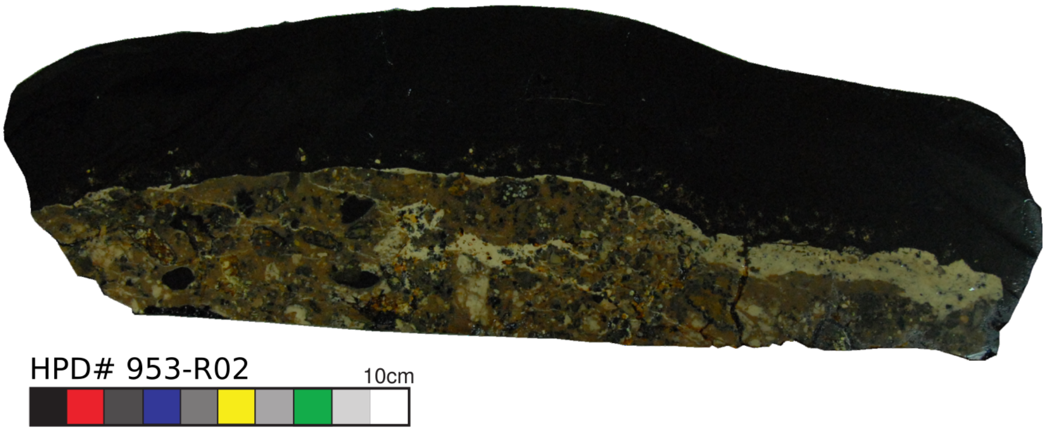

Figure 1-5: Cross-section of a Mn-crust sample, showing crust (black colour) deposited as a layer over a substrate rock (brown with intrusions). The sample has a thickness of 38 mm. This sample was collected by researchers during the NT13-13 cruise (JAMSTEC 2013).

The lateral distribution measurements can be done using a variety of sensors such as multibeam sonars or 3D mapping systems. Acoustic mapping is widely used for other seafloor surveys, because they can cover large areas at lower resolutions (Brown et al. 2011, Chakraborty & Paula n.d.). However, they provide less information for the task at hand. Since experts rely on ROV video feeds to manually locate Mn-crusts, visual mapping systems are a natural choice. By automating the detection of crusts using machine learning algorithms, large datasets can be analyzed quickly. Carrying both these sensors on a single robotic vehicle and conducting surveys together is further advantageous.

Having different sensors onboard is not sufficient without efficient algorithms. In addition, this gives rise to a new challenge in sensor fusion. The data from different sensors must be fused in a meaningful way so that maximum information regarding the distribution of Mn-crusts can be extracted. This is the focus of the current thesis.

A visual summary of the research background is provided in Fig. 1-6. The primary method for studying deep seafloor resources in the past was physical sampling done using big bulky vehicles such as ROVs. It costs time and money, yet provides low spatial resolution information. In the present, continuous surveys using different sensors mounted on robots such as AUVs are gaining popularity. In order to fully utilize the

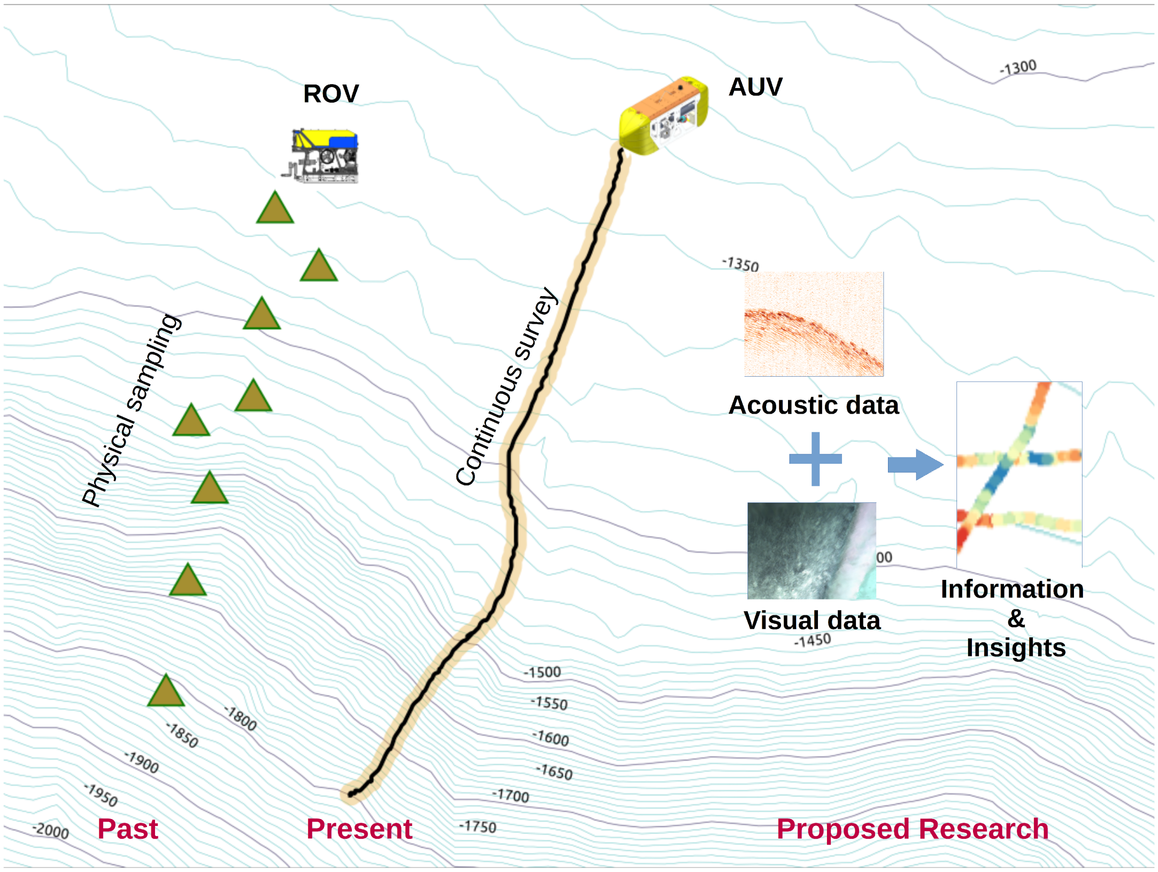

Figure 1-6: A summarizing illustration showing the background and scope for the proposed research

potential of such surveys, data fusion methods that combine different sensor data into meaningful information relevant for the survey being conducted is essential. In the proposed research, visual 3D data collected by a light-sectioning camera system and acoustic data collected by a subbottom acoustic probe are combined into volumetric distribution estimates of Cobalt-rich Manganese crust deposits.

1.5 Organizaton of dissertation

Chapter 1 provides an introduction to the importance of Mn-crusts and the opportunities and challenges in getting accurate information about their local distribution. **Chapter 2** details the relevant literature regarding past deep-sea mineral surveys and other relevant technologies which can be utilized for accurately surveying Mn-crusts.

The proposed work is outlined addressing the identified challenges using available technologies.

Chapter 3 describes the methods and algorithms in the proposed work in detail. The various assumptions, parameter selection and an estimate of errors is also explained.

Chapter 4 describes the results from implementing the proposed method on a large volume of seafloor data obtained from field trials. The results are analyzed in detail to observe the performance of the method and derive insights into the data.

Chapter 5 summarizes the contents of the dissertation, outlines the advantages, scope for future research in this direction and provides concluding remarks.

Appendix A provides a description of the underwater robots used to collect the data used in this dissertation.

Chapter 2

Literature Review and Research Objectives

This chapter describes the past efforts to study and survey Mn-crusts and identifies the objectives of the proposed research. From the point of view of exploiting these resources, it is necessary to find accurate volumetric distribution estimates. This in turn requires both the subsurface thickness of the crust layer and their lateral % coverage to be known (Glasby et al. 2015).

2.1 Past surveys of Mn-crusts

In order to compare different surveys of Mn-crust, from the perspective of volumetric estimation, Fig. 2-1 shows the survey resolution (number of measurements in fixed area) for different studies (not to scale). This is important because, although some studies collected large number of samples from seamount scale areas, they are not sufficient to study the Mn-crust variation in a given area. So the mere number of samples collected without regard to the area of survey is not enough.

Initial surveys of Mn-crusts were done using dredging from a ship (Hodkinson & Cronan 1991, Aplin & Cronan 1985), but samples recovered using this method are often damaged and cannot provide information about how representative the samples obtained are of the actual distribution since the method is inherently biased towards

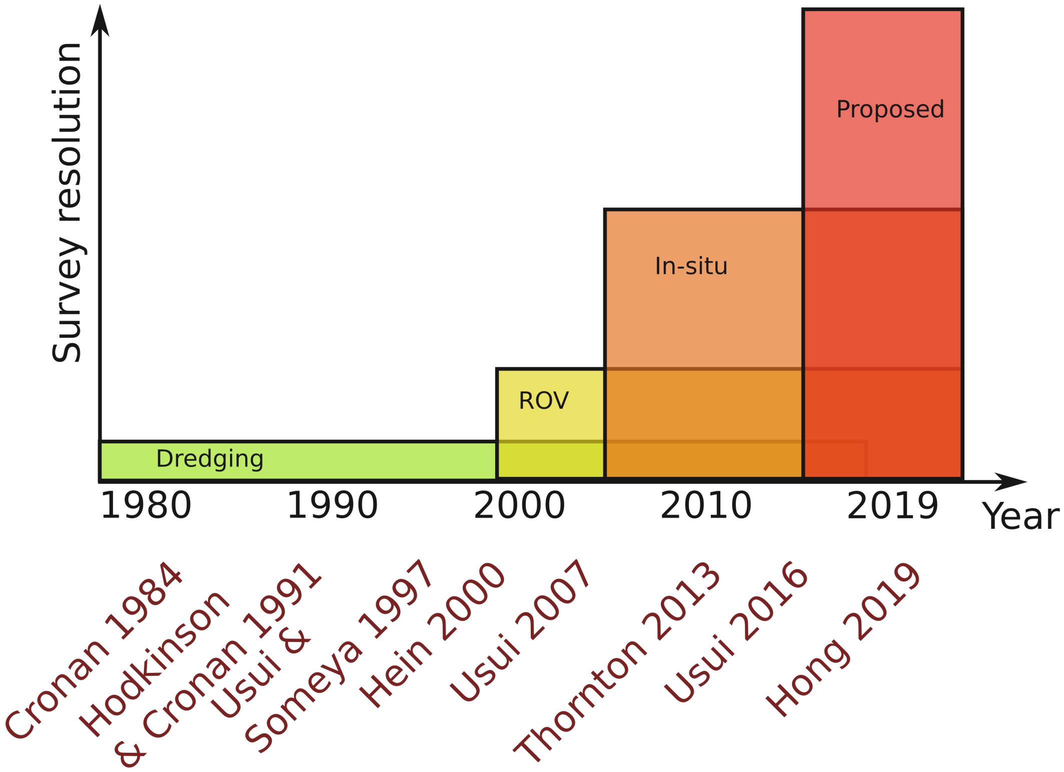

Figure 2-1: Timeline of Mn-crust exploration

loose rocks and edges that are more likely to be snagged. More recently, core drilling and sampling from ROVs has been shown to be effective to collect information about the thickness and elemental composition of samples whose context is understood from camera footage (Usui & Someya 1997, Usui et al. 2007, 2017). However, obtaining samples using this approach is time consuming, and the spatial resolutions that can be achieved through pointwise sampling is limited. Regarding the lateral distribution of exposed crusts, many studies have been carried out using video or still cameras mounted on towed sleds or ROVs, where the footage is manually labelled by human experts into categories such as Mn-crusts, nodules or sediment deposits, which are compiled into qualitative estimates of distribution (He et al. 2011, Yamazaki et al. 1994). However, manual labelling is time consuming, making it difficult to scale the operations to larger regions. In addition, measurements of distances within video streams or photos (without a reference measure in the image) is inaccurate due to perspective effect.

Mn-crust estimation at seamount scale regions have been attempted by researchers (Du, Ren, Yan, Shi, Liu & He 2017). Recently, efforts are underway to replicate the acoustic sub-bottom thickness measurement system from other countries around the world Hong, Feng, Huang, Wang & Xia (2019), Hong, Feng, Huang & Wang (2019).

Figure 2-2 shows the sampling of a Mn-crust from the ocean bed using an ROV and robotic arm.

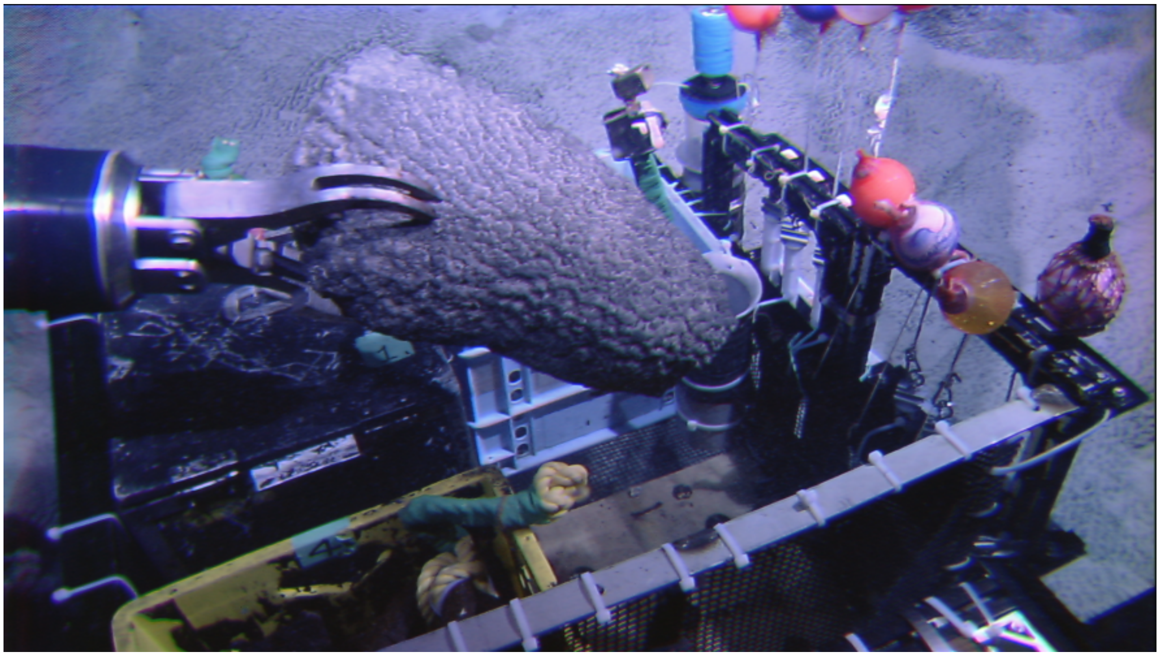

Figure 2-2: Sampling of Mn-crust from an ROV

2.1.1 In-situ Measurements of Mn-crust

In order to realise high resolution, scalable estimation of Mn-crust distribution, it is necessary to develop in-situ methods to determine the lateral distribution and thickness of Mn-crusts without physical sampling, and further develop algorithms to extract information concerning their distribution and abundance. Since Mn-crusts form a layer of deposit on top of a substrate rock, it is possible to distinguish the layers using acoustic methods and measure their thickness as long as the Mn-crusts and their substrates have distinct acoustic impedances (Thornton et al. 2009, 2013).

An AUV was developed for continuous in-situ survey of Mn-crusts (Nishida et al. 2016). The AUV is called Boss-A and is shown in figure A-1. It uses acoustic sub-bottom sonar sensors (Thornton et al. 2013) and a structured light 3D mapping system using a single camera and sheet laser (Bodenmann et al. 2012, Bodenmann, Thornton & Ura 2017, Bodenmann, Thornton, Nakajima & Ura 2017). This includes a real-time feedback of a double-gimbal system that orients the acoustic probe used to make measurements of crust thickness to be normal to the seafloor by analysing the 3D visual mapping data in real time (Sato et al. 2013). This allows acoustic measurements to be made on steeply sloped areas and over complex terrains. The 3000 m rated AUV weighs 600 kg and has successfully conducted several dives in the northwestern Pacific ocean. The data collected during these dives is analysed in the proposed research work.

2.1.2 Seafloor Classification

While acoustic methods are effective for determining subsurface structure, it can be difficult to determine if the signals obtained are of Mn-crust or different type of layered seafloor. Since one of the distinguishing features of Mn-crusts is their colour, visual methods can be effective to clarify this uncertainty as long as the process of identification can be automated. Automatic classification of seafloor imagery has been demonstrated for a variety of applications such as identifying coral species (Mehta et al. 2007, Stokes & Deane 2009, Friedman 2013, Gomes-Pereira et al. 2016, Alonso et al. 2019, Bongiorno et al. 2018) and seafloor fauna (Lüdtke et al. 2012, Lim 2017). In other studies of seafloor classification, researchers have attempted to classify the seafloor roughness using shipboard multibeams using neural networks (Chakraborty et al. 2003). Other researchers have attempted classification based on acoustic mapping data (Hamilton & Parnum 2011).

In Thornton et al. (2013), classification of Mn-crust covered seafloor was attempted for volumetric estimation. In this work, the seafloor was segmented into regions of crust, sediment and a mix of the two using Gaussian Mixture Models (GMM) and an average of acoustic measurements made was taken within each segment to estimate the abundance of crust in each region. A limitation of this approach is that the resolution of the volumetric distribution maps generated is dependent on the size of individual segments found in the data. Furthermore, the computational cost of the segmentation technique used is high and does not readily scale to the 2 orders of magnitude larger regions mapped in this work. However, this method requires the seafloor to be segmented into arbitrary sized patches, which is time consuming. A new method was proposed whose performance does not deteriorate as the seafloor area increases by the author in Neettiyath et al. (2015). The method segments the seafloor uniformly and uses a Support Vector Machine (SVM) for classification (Kubat 2015). The seafloor classes were expanded to include Mn-nodules as proposed by He et al. (2011) and transition regions were eliminated by increasing the resolution of segmentation.

2.1.3 Volumetric Estimation

The volume of Mn-crust present in the mapped area was estimated by combining the thickness measurements with the visual classification. In locations where Mn-crust is detected, a thickness value was estimated using the algorithms developed by the author (Neettiyath et al. 2017), building upon the algorithms developed by Thornton et al. (2013). This information was then extrapolated into areas where acoustic measurements were not made, but are identified to be crust using an inverse distance weighted averaging (Neettiyath et al. 2019). A percentage cover value was estimated from the classification information. Using the density of crust samples collected from the area in past ROV based surveys, a mass estimate can be calculated. This process is then repeated over other surveyed areas to cover large areas.

Mn-crust deposits are located thousands of metres below the sealevel as thin deposits only a few cm thick. Therefore, accurate measurements cannot be made from shipboard surveys or high-altitude cruising vehicles. A specialized sensor suite, nicknamed CRC system (Cobalt-Rich Crust mapping system) was developed for this task. Figure 2-3 shows a typical mapping scenario by the CRC system. The sensors which are part of the CRC system are described in section 2.2. The underwater robots which carried these sensors to the survey location is described in section A.

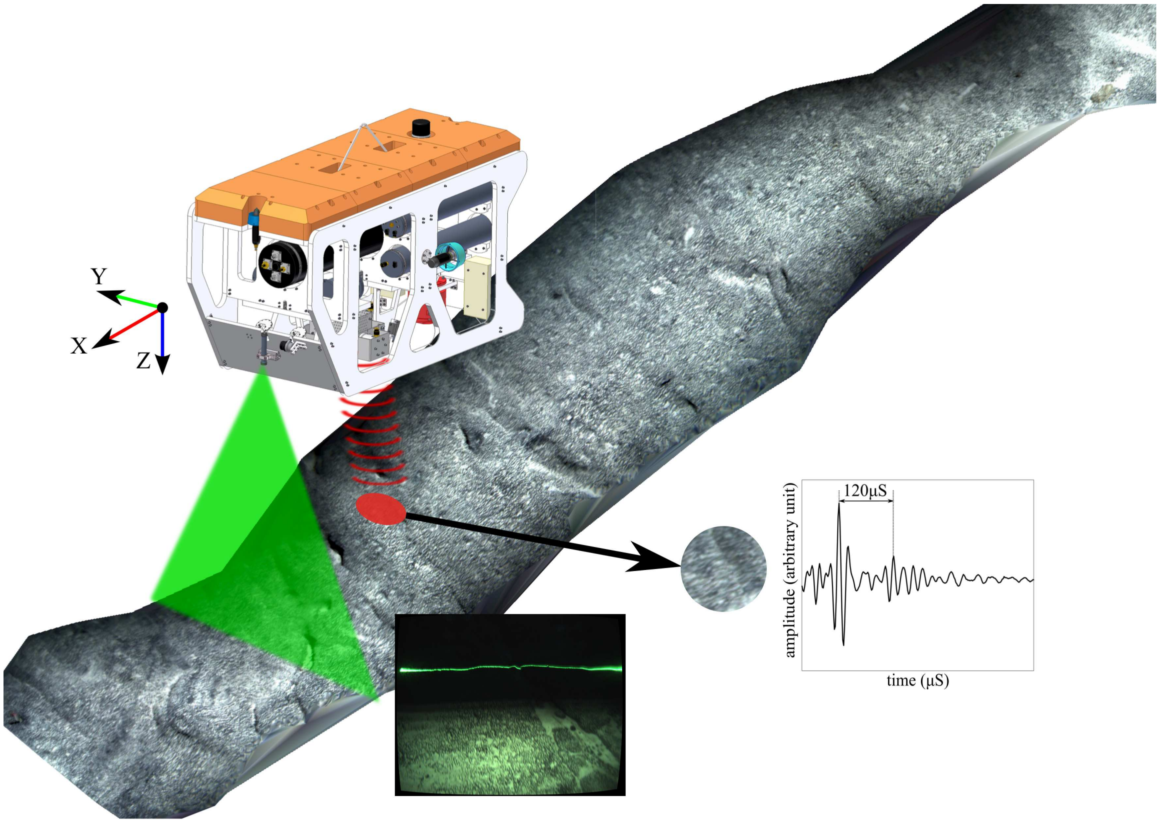

Figure 2-3: Mn-crusts are surveyed by acoustic and visual systems mounted on an underwater robot hovering at about 1.5 m above the seafloor.

2.2 Sensor suite for Mn-crust survey

The volumetric distribution of Mn-crusts can be estimated by measuring the thickness of the deposits and their lateral coverage. Section 2.2.1 describes the design and construction of the acoustic sub-bottom sonar developed for determining the Mn-crust thickness. The 3D mapping system described in section 2.2.2 generates a 3D mosaic of the seafloor, which was analysed to determine the lateral coverage.

2.2.1 Acoustic system

The acoustic system is built around a high intensity parametric sub-surface sonar that records sub-surface reflections of the seafloor. Figure 2-4 shows a typical measurement scenario on a Mn-crust sample. The recorded signal, in an ideal scenario, will consist of two major reflections, one from the top of the seafloor (i.e. top of the Mn-crust) and another from the interface between the Mn-crust and the substrate rock on which it is formed. The time delay between the reflections is twice the thickness of the crust multiplied by the velocity of sound in Mn-crust. Using the velocity measured in prior studies Thornton et al. (2009, 2011), the thickness is calculated.

The acoustic probe consists of a 5 channel annular array of 2 MHz piezoelectric transducers for transmission and a 200 kHz piezoelectric transducer in the centre for reception Thornton et al. (2013). The probe is dynamically focused on the seafloor at altitude ranges from 0.5 m up to 2.5 m. It focuses with a -3 dB footprint of 20 mm diameter on a target 1.5 m away. The probe has a vertical spatial resolution of about 1.4 mm and penetrates approximately 30 cm below the top-surface of the crust.

The measurements required the probe to be orthogonal to the measured surface for best results. This was achieved by mounting the probe on a two axis gimbal frame Sato et al. (2013). Using the light sectioned images recorded by the camera and DVL measurements of altitude, the slope of the seafloor is calculated in real-time. The optimal angle of the gimbals are calculated and transmitted to the gimbal actuators so that the beam is oriented normal to the seafloor. The processing of the

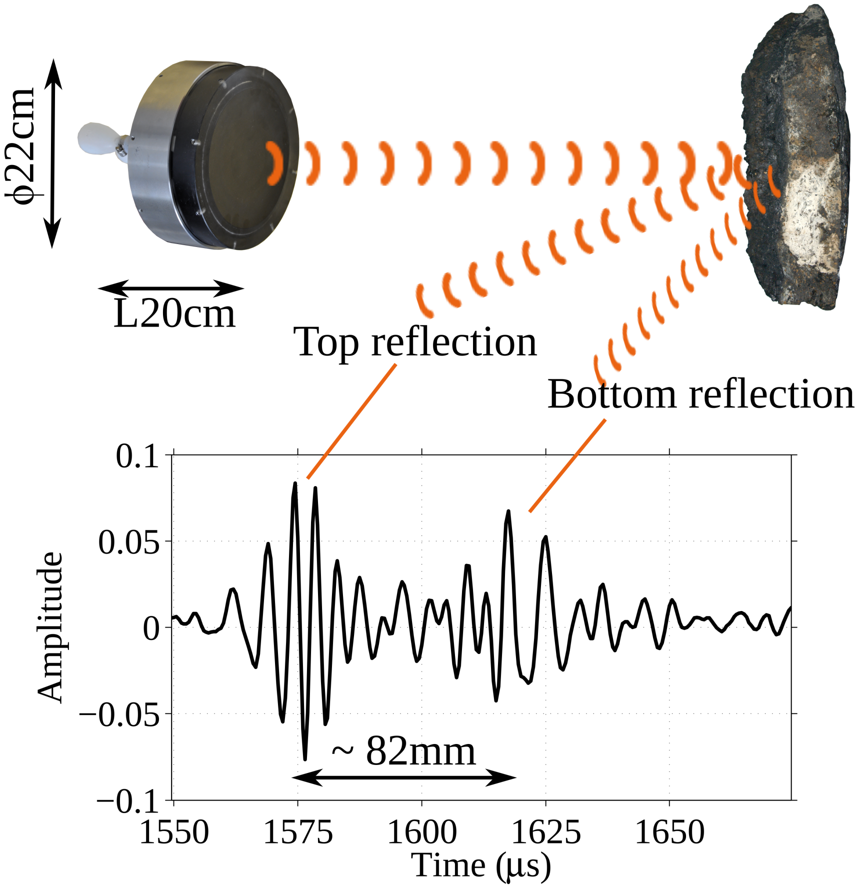

Figure 2-4: The acoustic subsystem works by calculating the time of flight between the reflections from the top and bottom of the crust layer. The deatiled description of the thickness measurement algorithm is described in section 3.3.

Table 2.1: Specifications of the acoustic sub-bottom probe

Frequency	2 MHz (carrier) 200 kHz (signal)
Footprint	$< 2\,cm$ (dynamic focusing)
Operating altitude range	$1.5 \pm 0.5\,m$
Mounting	2-axis gimbal
Range (roll gimbal)	±15°
Range (pitch gimbal)	±45°
Ping rate	20 Hz

recorded signals for calculating Mn-crust thickness is explained in detail in section 3.3.

2.2.2 Visual system

The visual system uses a light sectioning based 3D mapping system to generate 3D colour maps the seafloor using a single camera, a sheet laser and LEDs for illumination. The color 3D maps of the seafloor generated is analysed using the algorithm described in section 3.2 to calculate a lateral coverage of Mn-crusts.

The principle of operation of the visual system is shown in Fig. 2-5 Bodenmann, Thornton & Ura (2017). The images captured by the camera, which operates at 15 fps, consist of an illuminated section on the bottom and a dark section on the top. The sheet laser is configured so that the line falls into the dark section of the image at the operating altitude of the acoustic probe. The deformation of the laser line, which corresponds to the bathymetry of seafloor, can be used to calculate the xyz coordinates of the points that fall on the line, provided the position and orientation of the AUV and the accurate position and alignment of the sensors within the AUV are known. As the AUV moves, these points will come in the illuminated region of the image; the RGB color values of the point can then be identified. Thus, a point cloud containing the coordinates of the points on the seafloor and their RGB colour values can be generated for the region surveyed by the AUV.

Table 2.2 lists the specifications of the visual system. The swath of the transect (width of the 3D map) is a function of the camera opening angle and the altitude from

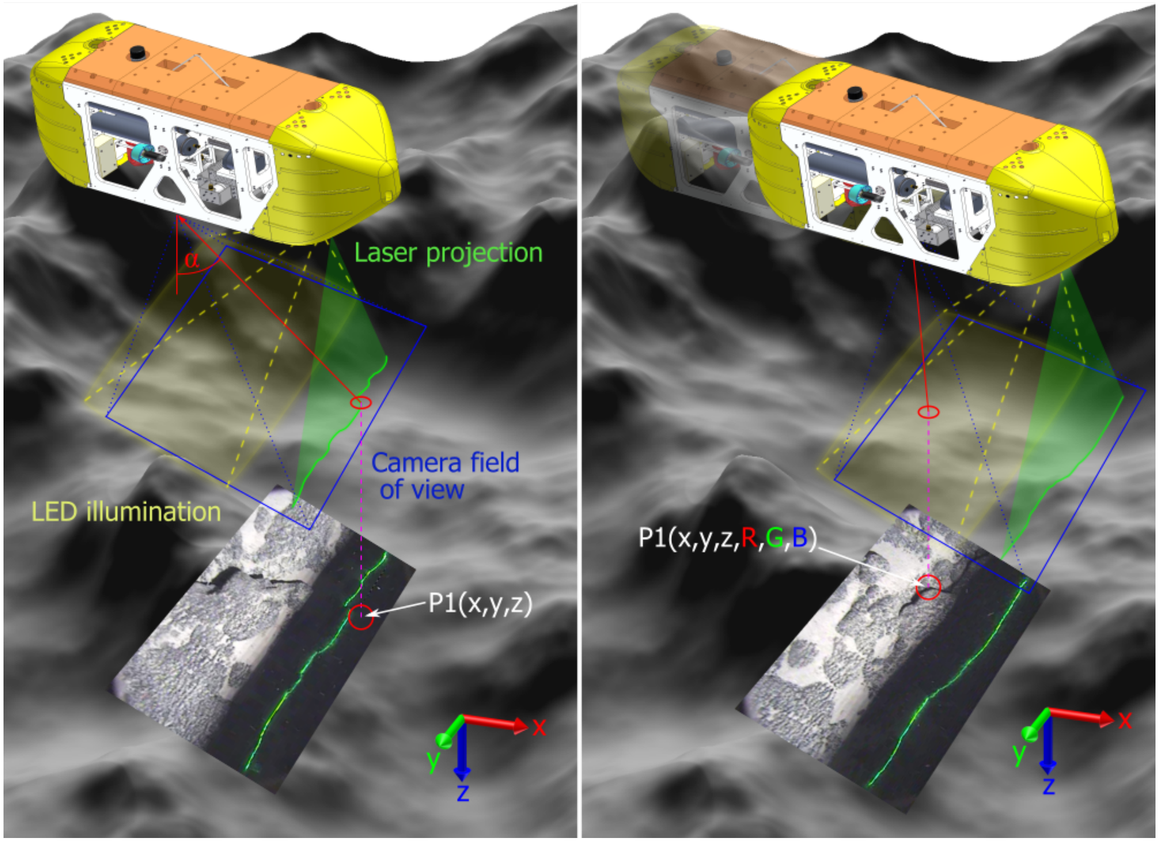

Figure 2-5: The bathymetry is measured by calculating the deformation of a sheet laser on the seafloor. When the same point comes into the illuminated part of the camera image, the colour values are measured.

Table 2.2: Specifications of the 3D visual mapping system

Type	Monocular vision and structured light using sheet laser
Illumination	2 x LED panels (20,000 lm/panel)
Laser power	120mW
Laser wavelength	532 nm
Camera resolution	1328 x 1048
Camera frame rate	15 fps
Laser to camera baseline	1.22 m
Swath (at 1.5 m)	1.5 m
Bathymetry resolution (at 1.5 m)	1.4 mm (cross-transect) 6.7 mm (along-transect) 3.0 mm (depth)
Image resolution (at 1.5 m)	1.4 mm
Target operating altitude	$1.5 \pm 0.5\,m$

which the survey was conducted. From an altitude of 1.5 m and a camera opening angle of 60°, the system used in this paper generates a map of about 1.5 m swath.

2.2.3 Navigational system

The navigational system supports the visual and acoustic systems by localizing the measurements. In AUV Boss-A, the navigation data of the AUV is shared, whereas for ROV, a separate dedicated set of sensors are mounted.

The navigational sensors include a Doppler Velocity Log (DVL), an Inertial Measurement Unit (IMU), and a pressure (depth) sensor. The data from all the sensors are combined using dead-reckoning to estimate the position of the robot. This position information is then used for processing the data generated by the visual and acoustic systems.

2.3 Research Objectives

Create a sensor fusion method that can identify the presence of Mn-crusts from visual 3D maps, calculate their thickness from acoustic sub-surface reflections and combine the two into volumetric estimates which can be used for studying distribution characteristics of Mn-crusts.

Chapter 3

Methods and Algorithms

This chapter describes the methods and algorithms developed for analyzing this large data to come up with volumetric distribution estimates of Mn-crusts, an overview of which is described in section 3.1. Three main algorithms were developed in this work which perform classification of seafloor 3D maps, analyse sub-surface reflections to calculate the thickness of the crust layer and extrapolate the thickness measurements into larger areas to perform volumetric estimations. These algorithms are respectively described in the following sections.

3.1 Overview of data analysis framework

The CRC system mounted on an AUV/ROV surveys the Mn-crust covered tops and shoulders areas of seamounts and collects data, including images, acoustic reflections, AUV navigational and other sensor logs and the metadata associated with them. A typical dive gathers several tens of gigabytes of data per hour. The workflow for processing the large amounts of data is explained in Fig. 3-1. The acoustic and visual data are processed separately and then combined using localization information from the navigation data.

The data generated by the systems is divided into seafloor sections of roughly 10m length, processed separately and the results are compiled. This division limits the process workload on the computer and allows for distributed processing. Visual data

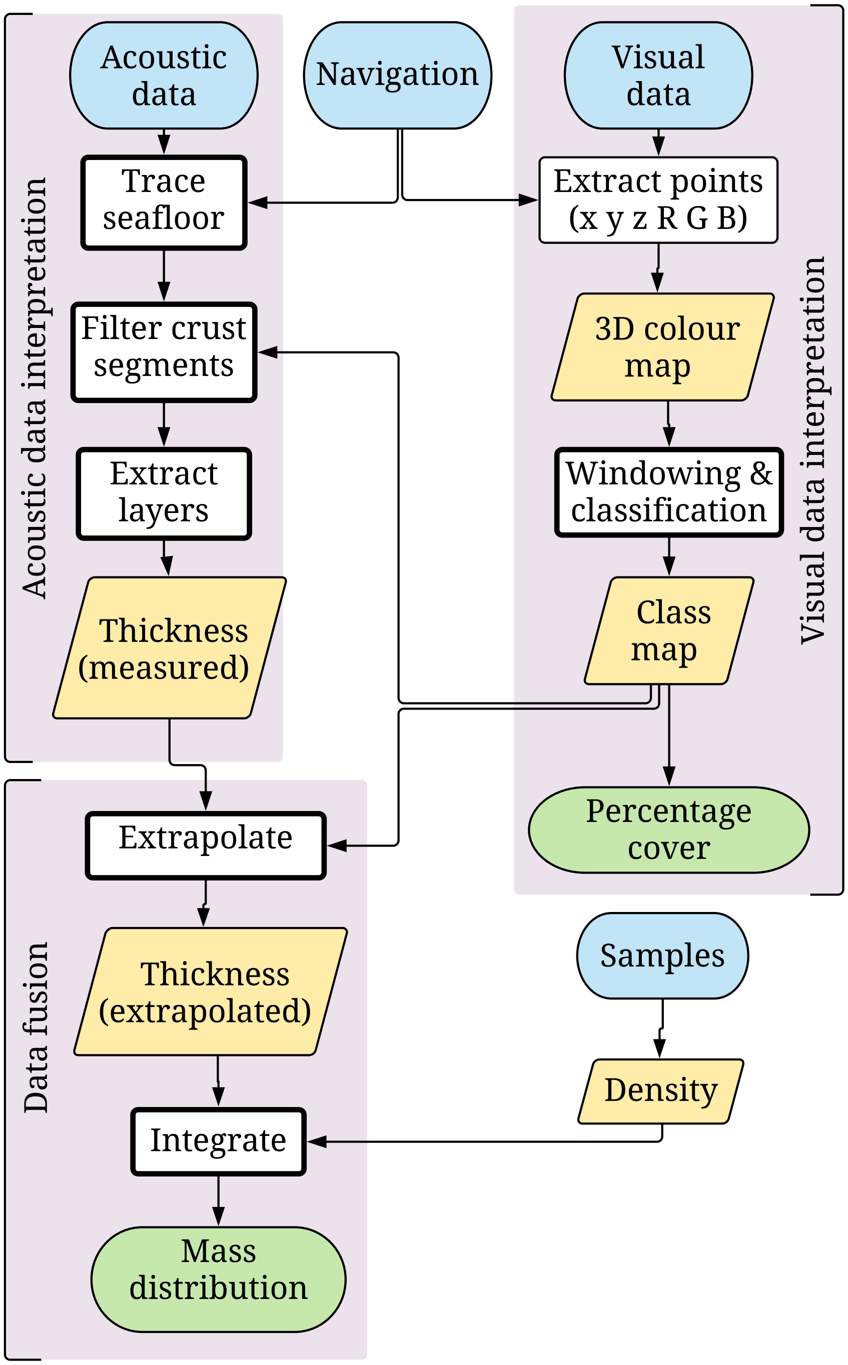

Figure 3-1: Flowchart of data processing framework.

is processed to generate 3D maps and is then classified into sections of crust, nodule and sediment to generate a class map, as described in section 3.2. The percentage coverage of exposed crust can be calculated from this map. The acoustic measurements over non-crust regions are discarded and crust reflections are processed to make filtered thickness measurements, as described in section 3.3. These thickness values are extrapolated into the available crust areas and the results are integrated to calculate the total volume of crust present in the region, as described in section 3.4.

3.2 Visual data interpretation

The visual system described in section 2.2.2 captures light sectioned images of the seafloors which are analysed to generate a 3D colour reconstruction of the seafloor as a point cloud (Bodenmann, Thornton & Ura 2017). Each point in the point cloud will have its position (xyz coordinates in cardinal directions) and colour (RGB values).

The 3D map is then classified into one of the 3 types of seafloor present in the region - namely continuous Mn-crust deposits, manganese nodules (Mn-nodules) and sediments (He et al. 2011). Examples of each type are shown in Fig. 3-2 and are denoted as crust, nodules and sediment respectively. Identifying the type of seafloor is usually performed by experts from the video streams generated by ROVs. A typical dive of an AUV/ROV is several hours long and gathers several gigabytes of data per camera per hour. Classifying all the data is a time consuming and repetitive task, which is poised favourably for automation.

Researchers have attempted to classify the seafloor using GMMs into crusts, sediments and transition areas, which are a mix of crusts and sediments (Thornton et al. 2013). This method however suffered from several drawbacks. The classification was performed of non-uniform sized segments extracted from the seafloor followed by extracting the shape and colour parameters of each segment. Segmentation is a computationally intensive process and the time increases exponentially w.r.t. the seafloor area; hence this method is not scalable. Other attempts to classify Mn-crusts into crusts and non-crust regions used Support Vector Machine (SVM) classifiers in

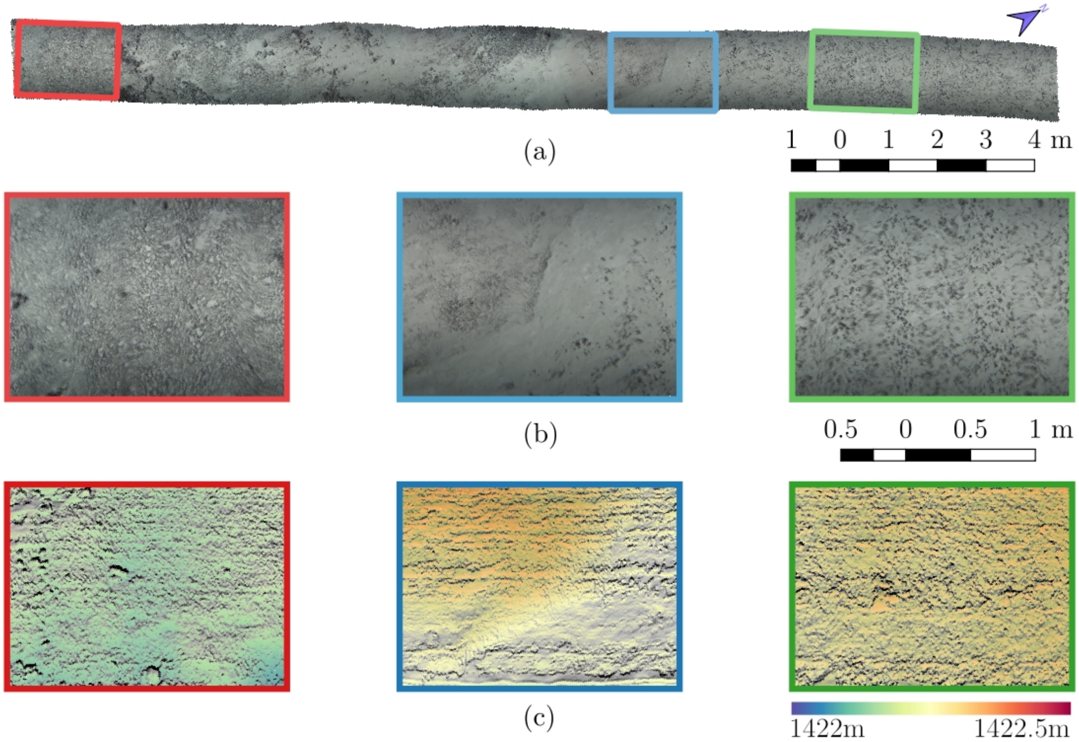

Figure 3-2: Different types of seafloor present in the area. (a) Top view of a 21 m section, with insets showing different types. (b) Detailed views of each type. (c) Bathymetric maps. The frames are colored as follows: (Red) Continuous Mn-crust deposits. (Blue) Sediment covered areas. (Green) Nodules of varying sizes.

order to filter out non-crust measurements (Neettiyath et al. 2015). However, the classification was restricted to small sections of seafloor where acoustic measurements were made. In other applications, classifying seafloor images to identify various animal, plant and coral species have been widely attempted (Friedman 2013, Lüdtke et al. 2012, Stokes & Deane 2009, Schoening et al. 2012), but were limited to image classification in the absence of bathymetric information. In terrestrial applications, researchers have used SVM to classify 3D point clouds in order to identify broccoli heads (Kusumam et al. 2017). Although neural networks are widely used in image classification tasks (Marcos et al. 2005, Kubat 2015), SVMs were found to perform better with well defined classes and large training datasets (Caruana & Niculescu-Mizil 2006, Bongiorno et al. 2018). Since the SVM classification is faster, processing

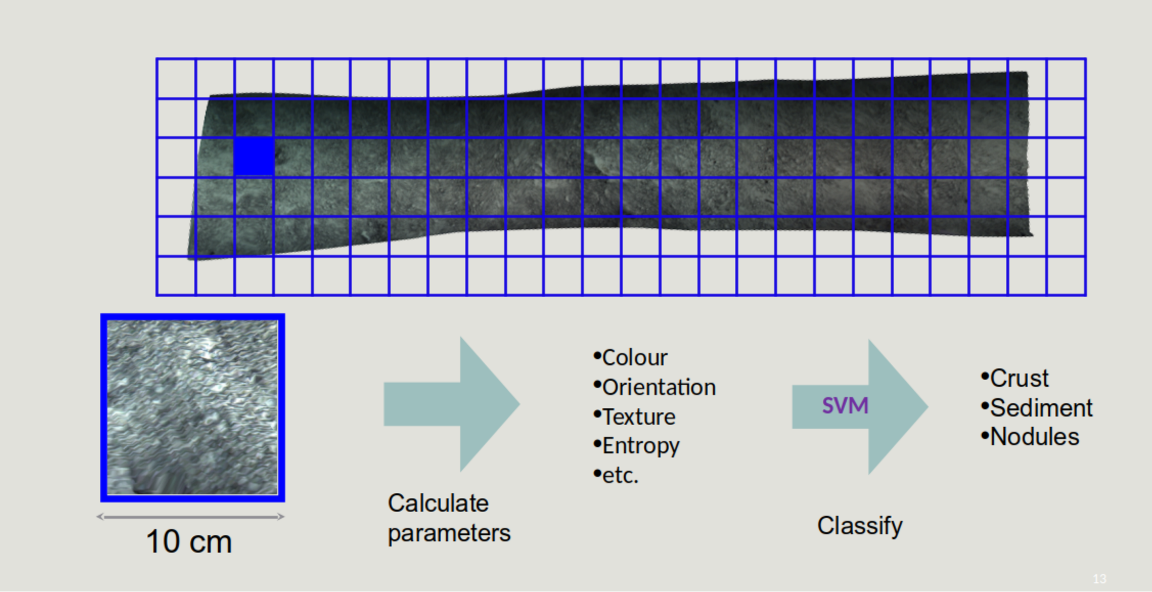

Figure 3-3: The seafloor map is divided into small sections called cells and the cells are analysed further.

times are reduced with large datasets. In addition, SVM is conceptually simpler and thus easier for post-analysis such as the impact of certain features on the classification.

A robust, high performance SVM classifier was constructed with a polynomial kernel using python for identifying Mn-crust from seafloor bathymetry and colour maps generated by the system (Unpingco 2016, Pedregosa et al. 2011). In order to make the classification scalable to large areas, the seafloor was sampled into uniform sections of 10 cm squares (called a cell) and classified, reducing the processing times to be linearly proportional to the area of seafloor being classified. Further improvements in processing times was achieved by rewriting the software to utilize parallel processing capabilities of modern microprocessors. Two large datasets (see Table 3.2 for details) were selected as training and testing, and cross validation sets to ensure that different variations of seafloor conditions are captured in the training data and can result in a robust classifier by preventing overfitting to particular lighting conditions or observation altitudes. By optimizing the cell size, choice of the feature vector and hyper-parameters of the classifier function, further improvements in classification performance was achieved.

Table 3.1: List of features calculated for each cell (Bold font indicate the features chosen for use in the final classifier based on the *F_1* scores calculated, see Fig. 3-7)

Bathymetric Features		Image Features	
$\boldsymbol{f_1}$	**Slope**	f_5	Luminosity mean
f_2	Vertical standard deviation	$\boldsymbol{f_6}$	**Luminosity standard deviation**
$\boldsymbol{f_3}$	**Roughness mean**	$\boldsymbol{f_7}$	**Luminosity entropy**
$\boldsymbol{f_4}$	**Roughness standard deviation**	$\boldsymbol{f_8}$	**Red intensity mean**
		f_9	Green intensity mean
		$\boldsymbol{f_{10}}$	**Blue intensity mean**
		$\boldsymbol{f_{11}}$	**Red intensity standard deviation**
		f_{12}	Green intensity standard deviation
		$\boldsymbol{f_{13}}$	**Blue intensity standard deviation**

A cell is defined as the unit seafloor area, which was classified into one of the 3 seafloor types. Each cell is an independent 3D point cloud with each point described by its colour (RGB) and location (xyz) values, and has no overlap with adjacent cells. Several parameters, called features, are calculated for each cell describing its colour or texture. A list of all the calculated features are given in Table 3.1. If a set of features (feature vector) that can accurately describe the cell can be identified, a high performance classifier can be built to classify the seafloor.

Bathymetric features describe the shape of the point cloud and are calculated from the xyz coordinates. The standard deviations in the vertical direction is a measure of the spread of the point cloud (f_2). The slope of the seafloor, independent of the direction it is facing is represented by f_1 (measured as the altitude angle or elevation angle) and is calulated as the deviation of the normal of the seafloor ($\mathbf{N}$, found by using Principal Component Analysis (PCA) on the point cloud).

$$f_1 = 90 - \cos^{-1}(\mathbf{N} \cdot \mathbf{V}) \tag{3.1}$$

Where $\mathbf{V} = [0, 0, -1]^T$ is the unit vector along Z axis facing away from the seafloor. The seafloor is relatively smoother in sediment covered areas and is more rough for crusts and nodules. This surface roughness is captured in two features, as defined in the ISO 4287:1997 standard, mean deviation and the standard deviation of the deviation from the plane of the cell in the normal direction (f_3 and f_4). Assuming that the cell consists of n points, with each point i being $(x_i, y_i, z_i, R_i, G_i, B_i)$, the deviation of each point can be calculated as

$$h_i = |\mathbf{N} \cdot [x_i, y_i, z_i]^T| \tag{3.2}$$

f_3 and f_4 are then calculated as the mean and the standard deviation of all the points within the cell respectively.

$$f_3 = \frac{\sum_i h_i}{n} \tag{3.3}$$

$$f_4 = \sqrt{\frac{\sum_i (h_i)^2}{n-1}} \tag{3.4}$$

Image features represent the features calculated from the colour of the seafloor. The simplest image features include the mean RGB values of the cell (f_8, f_9 and f_{10}) and their standard deviation (f_{11}, f_{12} and f_{13}). Since crusts and nodules appear darker than the sediment areas, a luminosity image of the cell is constructed. Luminosity of a point i is a measure of brightness of the point and can be calculated as

$$I_i = 0.21R_i + 0.72G_i + 0.07B_i \tag{3.5}$$

The mean and standard deviation of luminosity for each cell are calculated as f_5 and f_6 respectively.

$$f_5 = I = \frac{\sum_i I_i}{n} \tag{3.6}$$

$$f_6 = \sqrt{\frac{\sum_i (I_i - I)^2}{n-1}} \tag{3.7}$$

It can be seen that crust regions have a less uniform texture than the sediment and nodule regions. This is represented by entropy, a measure of randomness of the image. Entropy (f_7) is calculated from the luminosity image using the below equation.

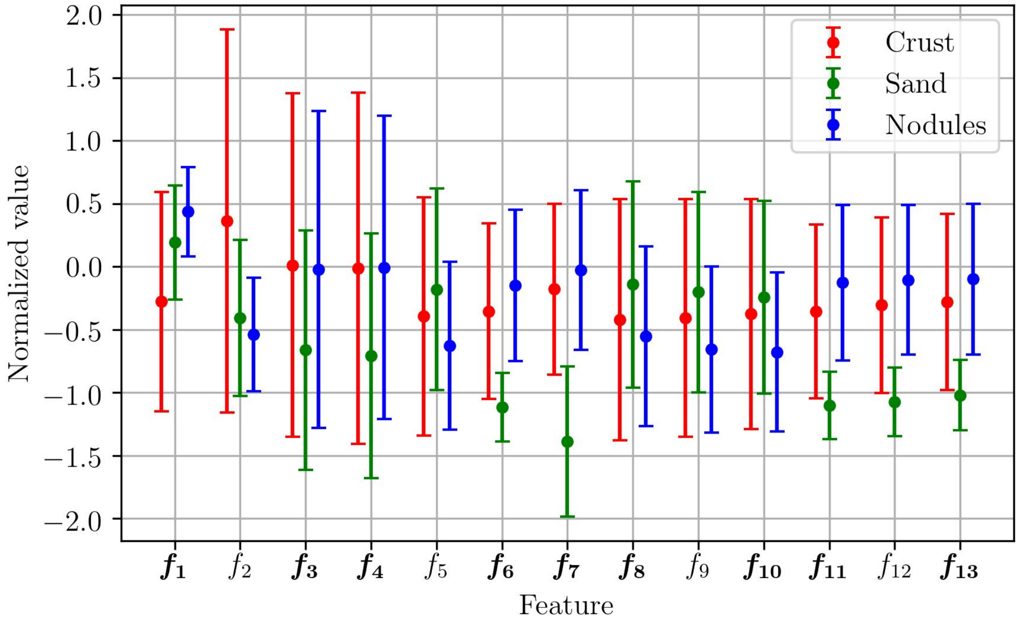

Figure 3-4: Features used and their variation w.r.t. seafloor types. The values are normalized to approximately zero mean and unit variance across the whole training data for a cell size of 10 cm. The bold font indicates features chosen for use in the final classifier based on the F_1 scores calculated, see Fig. 3-7.

$$f_7 = -\sum_j P(I_j)\log(P(I_j)) \tag{3.8}$$

where $P(I_j)$ is the probability that a random point j will have a luminous intensity I_j.

The normalised values of all features can be compared using Fig. 3-4. It can be noted that some features are good for identifying sediment cells (f_6, f_7, f_{11}, f_{12}, and f_{13}); f_2 shows high variations for crust sections and f_1 has high variation for all 3. Further investigations showed that combining features into feature sets can accurately distinguish between the three classes.

The size of the cell also plays an important role in accurately capturing the seafloor features. A small cell will have high variations for different seafloor types, but cannot capture large features of the seafloor, such as large rocks or low spatial frequency textures. A large cell will cause dilution of small features, but can capture large

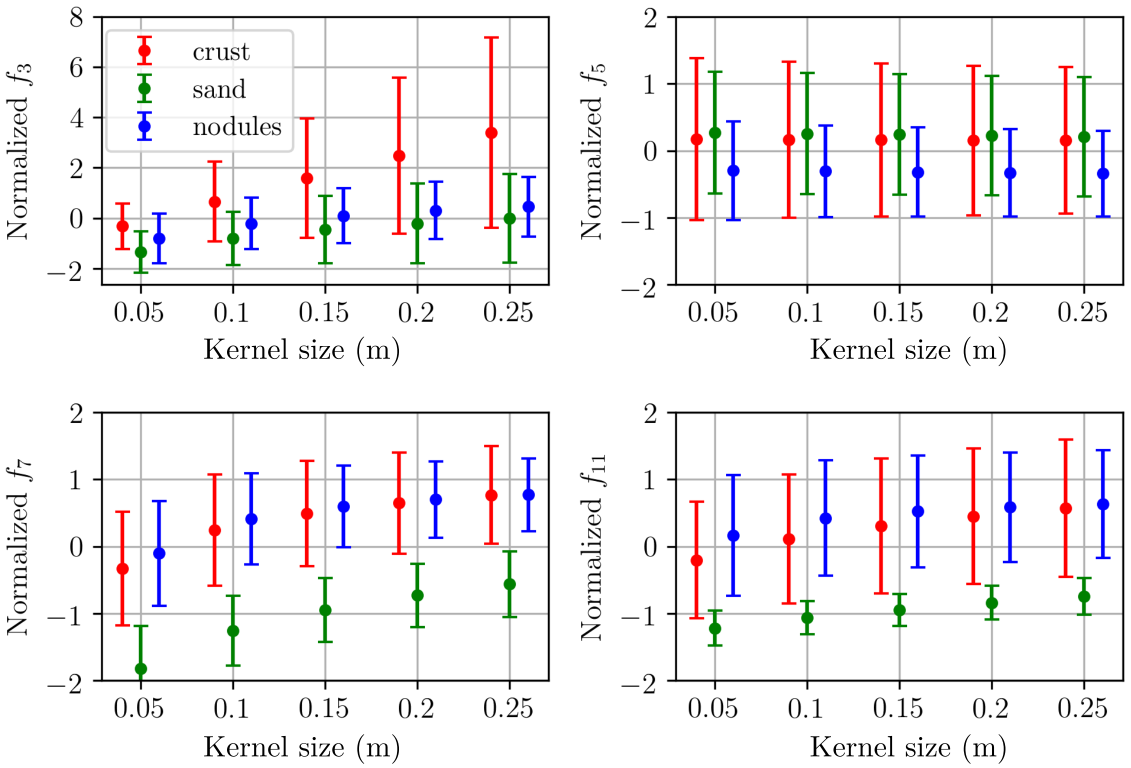

Figure 3-5: The variation in features when the cell sizes change. While the absolute values of the features vary, the relative difference between different seafloor types remains largely unaffected. This shows that the choice of cell size does not have a significant impact on the classification performance.

features. In order to check the effect of the size of cell w.r.t. the features, the training data was sampled at different cell sizes and the variation of parameters are observed. It can be seen that the size of the cell, though affects the absolute value of parameters, does not change their relative value among crust, sediment and nodules. Therefore, for the given resolution of seafloor 3D colour map data, classification can be performed using the above parameters without significant regard to the cell size. Since using a large cell will cause trimming larger areas near map edges, in order to maximise the area covered for volumetric estimation, a smaller cell size of 10 cm is selected. A representative set of features are shown in Fig. 3-5.

In order to identify the optimal feature vector, optimize the hyper-parameters and train the classifier, two datasets are selected and manually labelled. A summary of the two datasets is shown in Table 3.2. Dataset 1 consists of 58860 cells and dataset

Table 3.2: Statistics of manually labelled datasets used in building the SVM classifier.

Dataset	1. Training and testing	2. Cross validation
Dive number	BSA038	BSA031
Collected on	2017 January 21	2016 January 24
Crust area (m^2)	140	179
Sediment area (m^2)	164	107
Nodules area (m^2)	285	162

2 consists of 44830 cells. The training data was constructed by randomly selecting 5000 cells from dataset 1. The testing data for the classifier, whose results were used to tune the SVM, was constructed by randomly selecting a different set of 5000 cells from dataset 1. The entire dataset 2 was used as the cross validation dataset and was used in the final step for selecting the best performing feature set. Since the datasets are constructed from dives conducted at different times in different locations, the robustness of the classifier would be higher.

In order to select the optimal classifier, it is important to choose the right set of performance measures for the application (Kubat 2015, Stehman 1997). For example, Fig. 3-6(a) shows the confusion matrix of the classifier before optimization. Although the overall accuracy of the classifier is 84.3 %, only 76.0 % of the crust cells are classified accurately. This is not desirable since the objective of the proposed algorithm is to accurately determine Mn-crusts distribution. Therefore, the weight of the crust cells is increased to twice as that of nodules or sediments during training so that the classifier prefers crusts over other seafloor types. Also, F_1 score is used as the measure of performance instead of accuracy. Also, better measures of classification performance of crust as compared to overall accuracy was selected - precision and recall. Precision is a measure of the fraction of Mn-crust among all cells that was predicted as Mn-crust. Precision for class i is calculated as

$$Pr^i = \frac{N_i^i}{\sum_{j=1}^{3} N_i^j} \tag{3.9}$$

Where N_i^j is the number of cells of class i classified as class j.

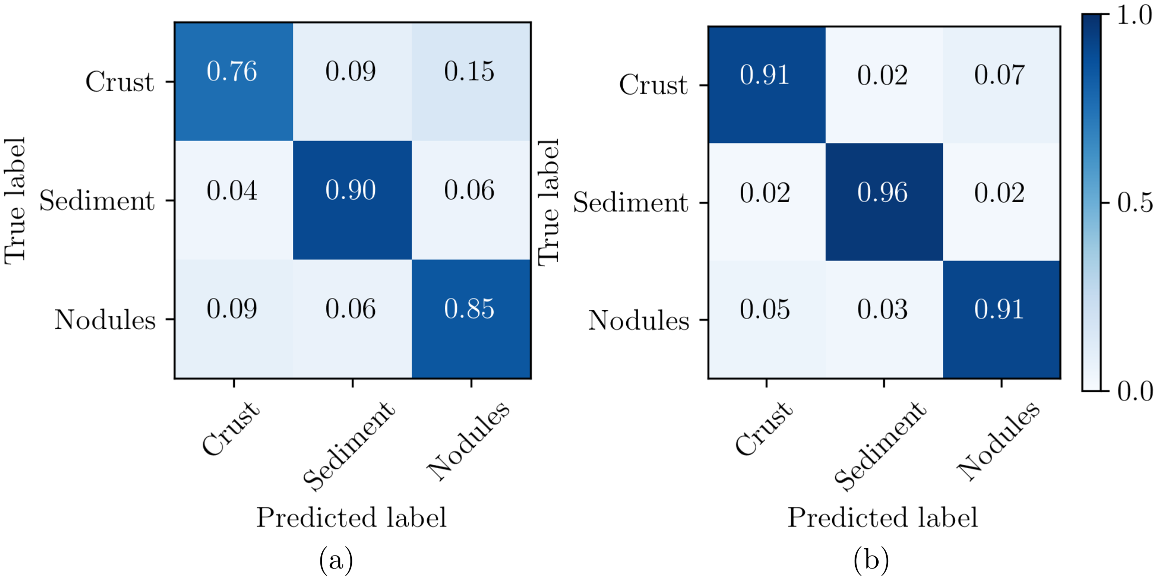

Figure 3-6: Confusion matrix of classifier a) before optimisation b) after optimisation.

Recall is a measure of the fraction of Mn-crust that was identified correctly. Recall for class i is calculated as

$$Re^i = \frac{N_i^i}{\sum_{j=1}^{3} N_j^i} \tag{3.10}$$

F₁ score combines Precision and Recall with equal consideration to both and is used as the single performance parameter objective for the classification task considered in this paper. Since accurately identifying crusts is important, F_1 score for class 1 (Crust) is calculated and optimized.

$$F_1^i = \frac{2}{\frac{1}{Pr^i} + \frac{1}{Re^i}} \tag{3.11}$$

The feature set with the best classification performance was identified by doing an extensive search of all possible feature vectors falling under three categories - image features only (C_1, which is the traditional image classification problem), bathymetric features only (C_2) and a combination of both image and bathymetric features (C_3). An exhaustive list of feature vectors are constructed and the classifiers with the highest F_1-scores are selected. Feature vectors from C_3 performed better than others indicating the usefulness of additional bathymetric data. Fig. 3-7 shows the accuracy values for the best two classifiers for each feature vector length from C_3. It can be seen that the score increases as the number of features increase. However this could also happen due to overfitting the classifier. To verify this, cross validation accuracy using dataset 2 is plotted alongside for each candidate. The classifier ζ_9, with 9 features (f_1, f_3, f_4, f_6, f_7, f_8, f_{10}, f_{11}, and f_{13}), has both the highest CV scores of 90.0% accuracy and 87.7% F_1-score. This feature vector was selected for the SVM classifier and is highlighted in bold in Fig. 3-7. Although only the red and blue channel features are present in the final feature vector, by looking at all the feature vectors in Fig. 3-7, the performance of the classifier appears to be mostly unaffected by the hue of the image. The decision boundary of the classifier ζ_9 shows that crust is more prevalent in steeper areas. The mean roughness value is higher than the standard deviation of roughness for nodules indicating an undulating texture. These results along with the high accuracy indicates a classifier suitable for classifying seafloor 3D colour point clouds.

The classifier was further tuned by optimizing the hyper-parameters which influence the SVM decision function. Two methods are typically used by researchers- grid search and random search (Bergstra & Bengio 2012). Grid search is exhaustive, time consuming, and limited in range of values, but provides accurate results; whereas random search is relatively faster, but gives approximate results over larger range of values. The best values were chosen by conducting a random search over a large range of parameter values followed by a extensive grid search in the vicinity of the best performing parameter values calculated by the random search. 3 kernel functions (Radial Basis Function - RBF, polynomial and linear) were considered in each case. This process was repeated for each kernel type and a polynomial kernel of 2nd degree was chosen for the final classifier.

Using the selected classifier, the seafloor data is classified and crust sections are identified. A thickness value is identified in the crust regions.

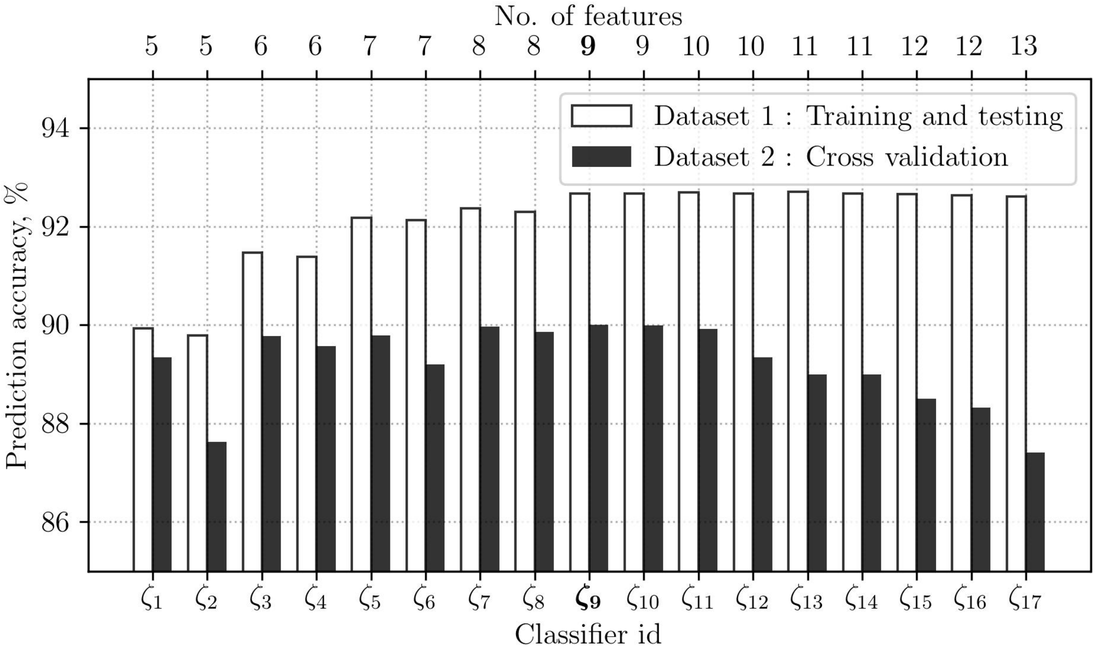

Figure 3-7: Performance of the feature vector size on classification. Beyond 7 features, increasing the number of features increases scores by a minimal amount. However, on cross-validation, the higher results turn out to be due to overfitting. The selected classifier (ζ_9) is highlighted.

3.3 Acoustic data interpretation

Figure 3-8 shows the operation of the double gimbal used to orient the beam normal to the seafloor.

Using the data acquired by the probe, the thickness of the crust layer can be determined from the acoustic signals based on the acoustic velocity. However, automated and reliable extraction of this information in the presence of noise due to scattering, multi-path reflections, local inclusions inside the crust layer, fluctuating signal levels and signal attenuation is not trivial. In order to constrain the outputs of algorithms to extract the thickness of exposed crust layers, the fact that the thickness of the layers is typically locally continuous is leveraged (Neettiyath et al. 2015). The proposed method uses a combination of image processing and acoustic signal processing, and instead of considering signals individually, translates successive measurements into a spatial frame and applies image processing techniques to find layers that are

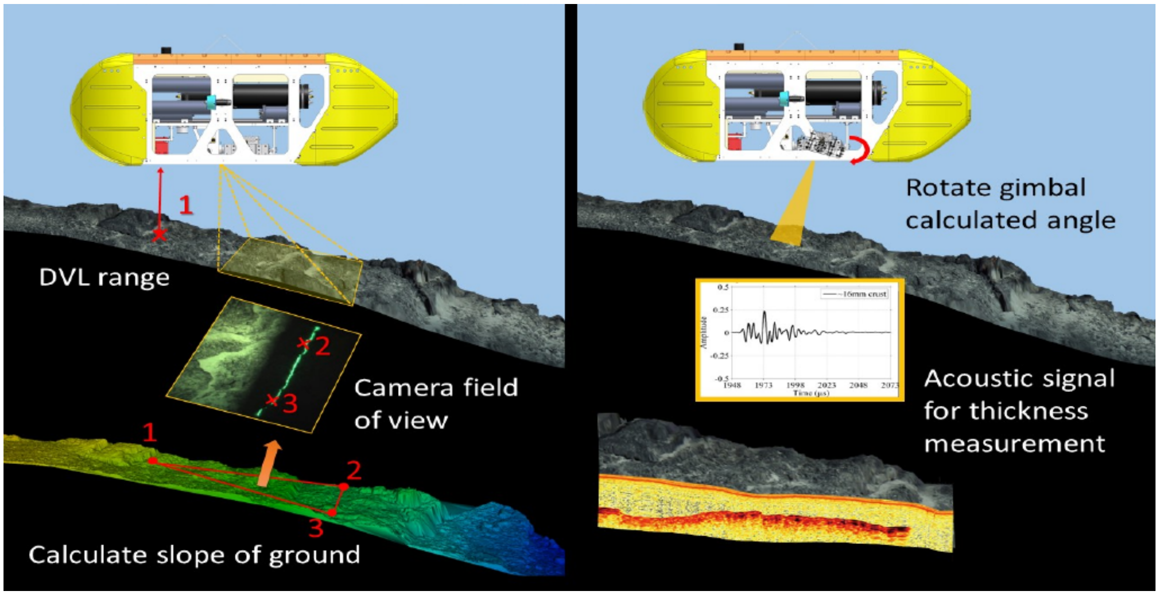

Figure 3-8: Operation of gimbal on AUV BOSS-A.

consistent, and that exposed crusts are more easily confirmed using visual rather than acoustic methods.

Acoustic reflections made over seafloor sections classified as crust are selected and a thickness value is estimated using an improvised version of the algorithm described in 3.2. The acoustic measurements are corrupted by noise generated by scattering, multi-path reflections, and local inclusions in the crust layer (Jackson & Richardson 2007). In order to identify a continuous layer of Mn-crust from successive measurements, spaced approximately one cm apart, a 4-step algorithm is used which is a combination of several image processing and signal processing tools. The 4 steps are filtering individual pulses, extracting signal boundaries, re-framing the signal into a distance based grid, and identifying secondary reflections to calculate thickness.

The measurements begin with the firing of a short amplitude modulated 2 MHz burst, and recording its reflections for 4.096 ms where measurements are repeated at a sampling interval of 50 ms. An arbitrary number of pulses (denoted as N) are stacked together to form a frame. N is decided by the user depending on the number of pulses to be processed. The frame is formed in such a way that each pixel is a signal value, each vertical line from top to bottom is the recording of a single pulse, and these are stacked consecutively from left to right. Each frame is treated as a 2-D

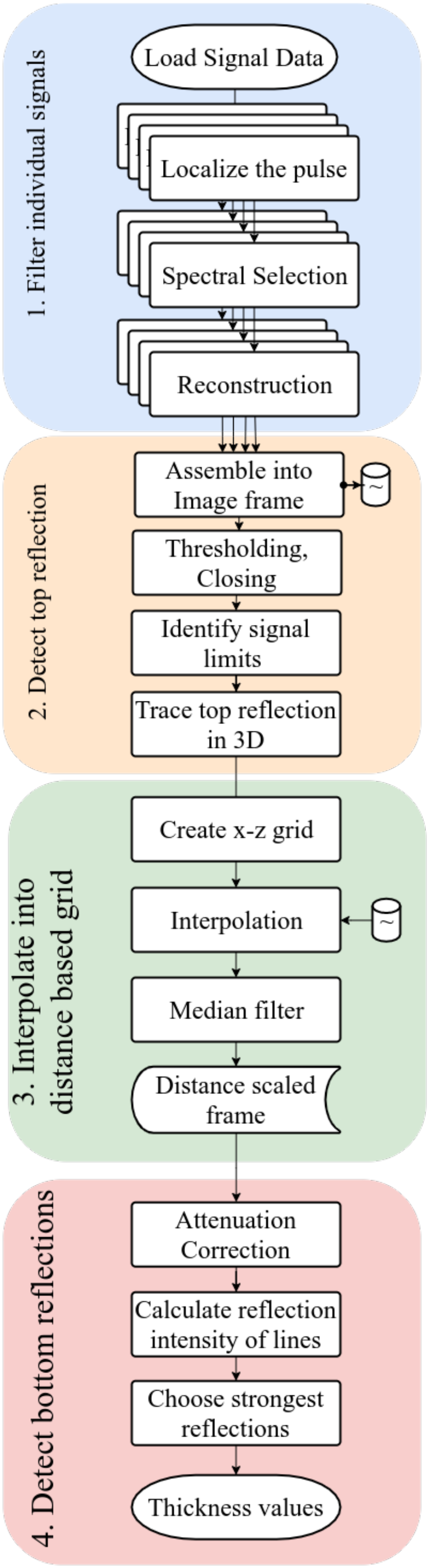

Figure 3-9: Flowchart of thickness measurement

grayscale image. Since the axes are aligned with respect to time, it does not always scale linearly to distance. In order to reconstruct the physical scales, the data are plotted on a distance scaled axes based on the vehicle's navigation data and the angle of the gimbals in later processing stages. The probe then enters a standby mode until the beginning of the next pulse.

The process of finding thickness of Mn-crust from the recorded data consists of four steps - filtering individual pulses, extracting signal boundaries, re-framing the signal into a distance based grid, and identifying reflections to calculate thickness.

The pulse transmitted from the acoustic probe is a parametric wave whose shape can be approximated into an exponentially decaying sine wave. By deconvolving this signal with the reflected signal, the exact instants where the reflections happened can be identified from the recorded signal. However deconvolution is highly sensitive to noise and noise levels are very high in underwater measurements. Therefore, an equivalent operation was performed by calculating the cross spectral density between the two signals. The recorded signal was cropped using a moving rectangular window and the cross spectral densities are calculated at regular intervals. An analysis of the resultant spectrum reveal that the strongest components in the spectrum occur around 200 kHz, the transmitted signal frequency, as shown in Fig. 3-10. The spectral components that fall within the 3 dB bandwidth - which was identified to be between 70 kHz and 300 kHz - are selected and a filtered pulse is reconstructed by adding these components to increase the signal to noise ratio.

The reconstructed signals are assembled into an image frame using the methodology explained in section 3.3. This image is then filtered using a median image filter in order to remove shot noise without blurring the image. In the frame, the reflections from the crust are continuous regions having relatively high intensity values. They are selected by thresholding the image using an adaptive threshold value. Otsu's method is used for calculating the threshold value Otsu (1979). The adaptive threshold will ensure that variations in signal levels across different datasets arising due to changes in the underwater environment and changes in the system tuning does not affect the results. The resulting binary image will have several small disconnected peaks. In

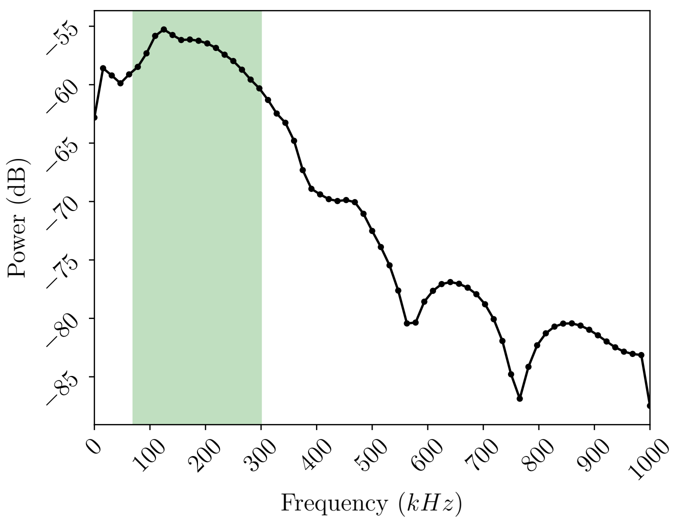

Figure 3-10: Cross correlation spectrum. The 3 dB bandwidth is highlighted

order to consider these into the signal region, a morphological closing operation is performed using a rectangular kernel of 6 × 11 pixels. The top and bottom boundaries of the signal region is then extracted as the first non-zero line with a minimum width (a value of approximately 7.5 mm was used) from the top and bottom of the image respectively. Further processing focuses only in this region to find the reflections and thickness.

The physical nature of Mn-crusts dictate a dependence on spatial scales and is independent of temporal aspects such as the frequency of measurement or the speed of AUV. Thus, for further processing, the signals are transformed into a spatial 2-D frame. A point in 3-D space is identified for each of the pulses as the highest point of the top line. The coordinates of these points are calculated using the localization information of the AUV and the pose of the acoustic probe using a coordinate transformation. A line is then traced through these points in 3-D space, which is considered as the top surface of the Mn-crust. The distance along the this line is calculated and is used as the horizontal coordinate for the frame. The trace distance is sampled at uniform intervals of defined horizontal resolution (the authors used a resolution of 0.01 m, which is the approximate average physical distance between two adjacent pulses). The vertical resolution was calculated using equation 3.12.

$$V_{res} = \frac{x_{shift} \cdot \nu_{sound}}{2 \cdot f_s} \tag{3.12}$$

where $\nu_{sound} = 2932\,{}^{\mathrm{m}}/_{\mathrm{s}}$ is the velocity of sound in Mn-crust Thornton et al. (2009), x_{shift} is the width by which the window is shifted while calculating the cross-correlation spectrum, and $f_s = 2\,\mathrm{MHz}$ is the rate of sampling of the measured signal. Although this vertical resolution does not accurately describe all parts of the image due to the change in speed of sound, it is valid throughout the region of interest of the signal calculated in the previous step and thus can accurately describe the reflections inside the crust.

The signals are plotted similar to the previous frame, left to right and top to bottom, with the vertical axis of the frame compensated for each pulse separately based on probe's depth for each pulse. The horizontal location of each pulse is interpolated using a one dimensional nearest neighbor interpolation using k-D trees. The result is an image frame consisting of signal reflection intensities with physical locations to scale, from which the reflections and therefore the thickness can be determined.

The image is then filtered using a 2D median filter for removing noise using a square kernel of approximately 5 mm size. The filtered image is then corrected for attenuation, between the top and bottom boundaries of the signal's region of interest. Equation 3.13 shows the calculation performed.

$$\gamma_{\alpha}^{i}\left[z\right] = \begin{cases} \gamma^{i}\left[z\right] \times 10^{2\alpha_f (z - z_{top})/20} & \text{if} \quad z_{top} \leq z \leq z_{bot} \\ \gamma^{i}\left[z\right] & \text{elsewhere} \end{cases} \tag{3.13}$$

where $\gamma^{i}\left[z\right]$ denotes the pixel at vertical coordinate z and horizontal coordinate i. The signal's region of interest, as identified in step 11 is between z_{top} and z_{bot}. $\alpha_f = 1.266{}^{\mathrm{dB}}/_{\mathrm{cm}}$ is the attenuation coefficient of Mn-crust at the measuring frequency, calculated using the value measured in Thornton et al. (2009).

The final steps of calculation consists of identifying the lines corresponding to the secondary reflections within the region of interest. The primary reflection is identified as the top of the signal region.

Figure 3-11: Topview of the seafloor showing the region from where acoustic reflections were obtained

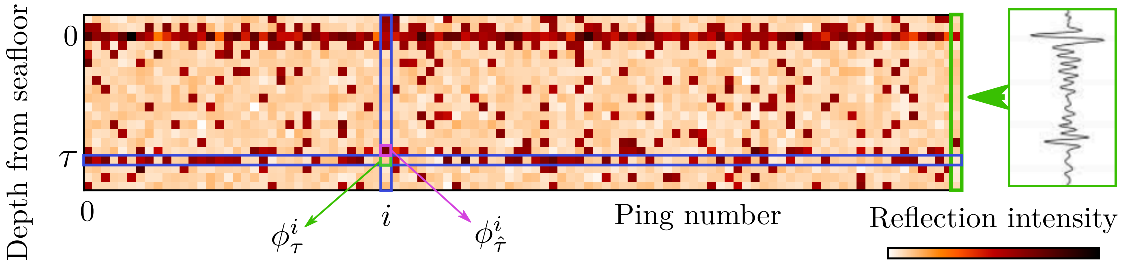

Figure 3-12: Representative figure showing acoustic thickness estimation. The reflections are arranged as an image aligned w.r.t. the top reflection. A cost function is calculated for each potential thickness (see (3.14))

In the third step, the reflections are bundled together into a single image frame, where each pixel represents the reflection intensity of a single point. The frame lies along the trace of the acoustic ping on the seafloor as the horizontal axis and depth of the respective point as the vertical axis. The signals are sampled into a uniform 2D grid in order to eliminate dependency on temporal parameters such as the frequency of measurement and the velocity of the AUV. A representative image is shown in Fig. 3-12, where darker colours indicate stronger reflections. The image is filtered using a median filter of about 5 mm square kernel in order to reduce noise. The signals are then corrected for attenuation in seawater within the signal region identified in step 2.

Since the top surface have been identified as Mn-crust by the SVM classifier, a secondary reflection is assumed to exist throughout the selected reflections and the best candidate is selected using an integral function that calculates the strength of reflections. The entire acoustic frame is denoted as Φ and an individual point in the image as ϕ^i_τ, where i denotes the X coordinate (ping number) and τ denotes the Y coordinate (depth from seafloor). A cost function is calculated for each potential thickness value of τ as shown in (3.14).

$$\Gamma_\tau = -\sum_{i \in X} |\phi^i_{\hat{\tau}}| \tag{3.14}$$

where $\phi^i_{\hat{\tau}}$ is the point with highest intensity within a threshold distance to τ, for each ping i. For example, in Fig. 3-12, the point directly above τ is used ($\hat{\tau} = \tau - 1$). This is done to account for minor local variations of thickness within the layer. The mean thickness is identified as the τ having the lowest cost Γ_τ and the secondary layer, which is the crust-substrate interface, is calculated as $\phi^i_{\hat{\tau}}$, for each ping i. Thus the thickness becomes

$$t_i = \hat{\tau}_i \tag{3.15}$$

This will result in a thickness value which is consistent over the range of several meters, yet accommodates for the local, minor variations in crust thickness.

The proposed method is verified on the data collected over a patch of seafloor of approximate length of 8.1 m, a visual 3D reconstruction of which is shown in Fig. 3-11. This data was collected during the BSA-032 dive using Boss-A. The initial processing steps are shown in Fig. 3-13. The acoustic data collected is shown in Fig. 3-13a as a colour-coded image frame. The values are scaled along a logarithmic axis with lighter colours indicating a higher signal amplitude level. After filtering the individual pulses and the signals are arranged into an image frame as shown in Fig. 3-13b.

The image is thresholded into a binary image followed by a morphological closing operation resulting in Fig. 3-13c. The limits of the signal region are identified and are shown in Fig. 3-13d overlaid on Fig. 3-13b. The top boundary is plotted as a blue line

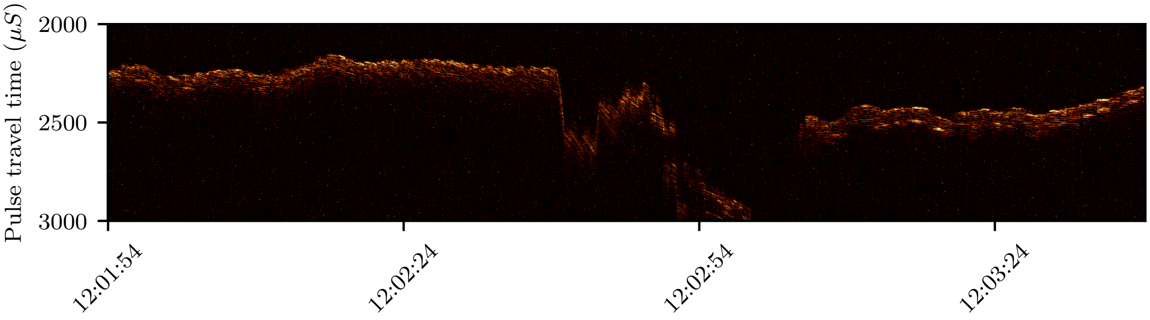

(a) Image frame consisting of 1800 recorded signals cropped to the region containing signals

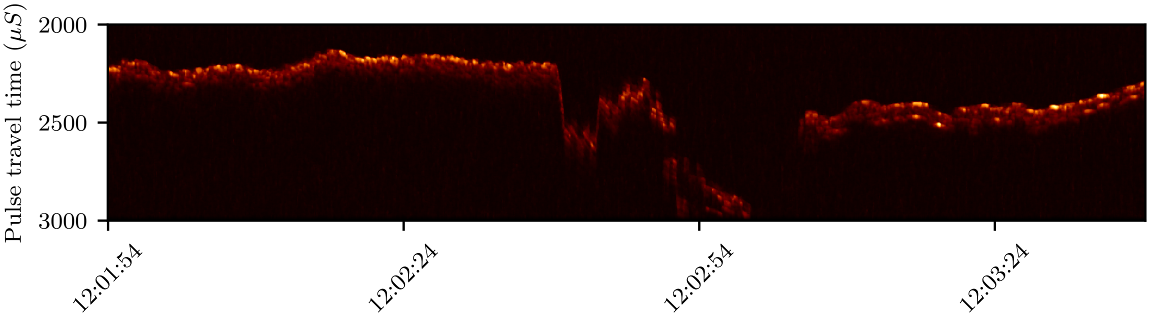

(b) Image after CSD and filtering

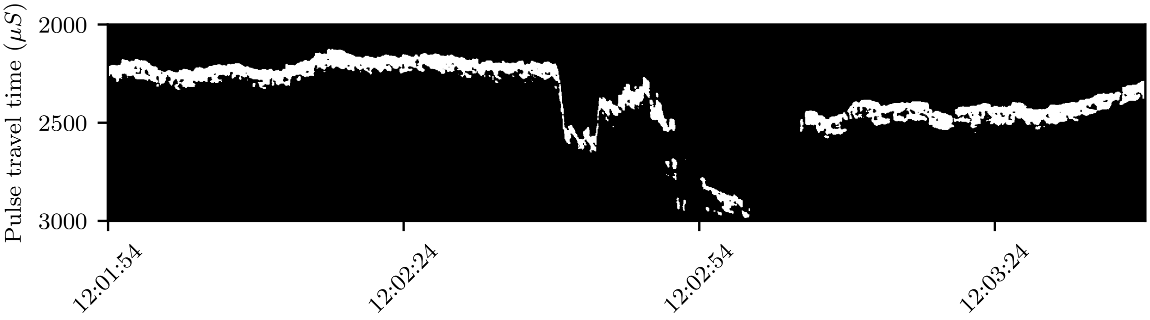

(c) Image after thresholding and closing

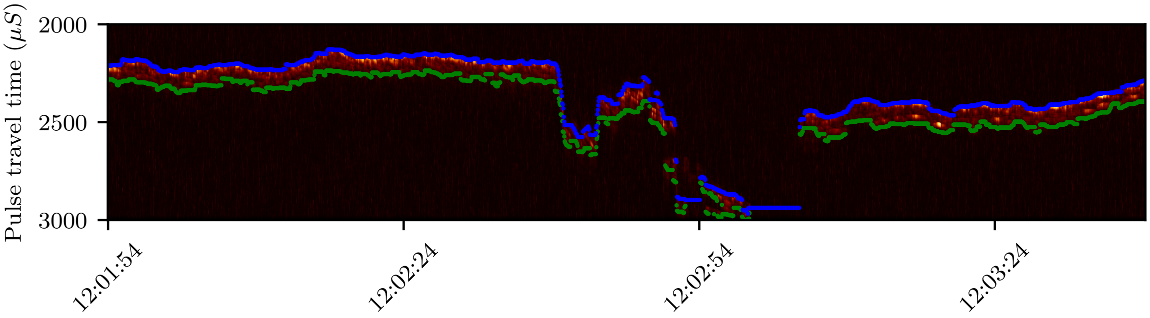

(d) Detected top and bottom boundaries of signal region, in blue and green colours respectively

Figure 3-13: Steps leading up to detection of the signal boundaries

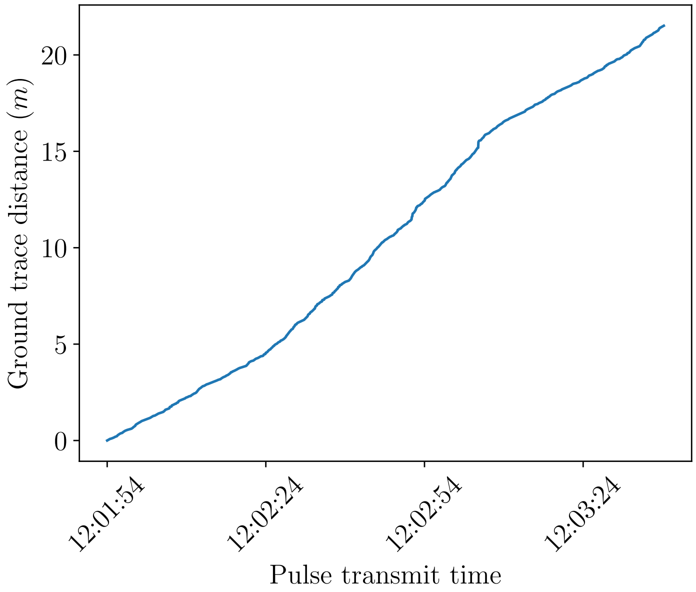

Figure 3-14: Integrated trace distance of the signal

and the bottom boundary is plotted as a green line. Tracing the top line in 3D space result in Fig. 3-14. The traced line has a length of about 22 m on a patch of about 8 m distance; this behavior arises due to the gimbals which causes the acoustic beam to move in a nonlinear fashion on the seafloor. The signals are then interpolated into a distance based axes resulting in Fig. 3-15a; the horizontal resolution of the axes is chosen to be 10 mm and vertical resolution is calculated to be about 1.9 mm.

After filtering and attenuation correction, in the image, within the limits identified in Fig. 3-13d, the potential secondary reflections are identified using progressive probabilistic hough transform. The calculation used a minimum line length of 60 cm and a maximum gap of 10 cm as parameters. These parameters ensured that long lines are detected despite smaller gaps, while small inclusions that result in pulses with ideal reflections are excluded. Optimal candidates for the secondary reflections are identified based on the intensity of reflections and thickness values are calculated. The estimated thickness values are shown in Fig. 3-15b.

The mean thickness of the crust in the region was calculated to be approximately 65 mm, which is consistent with the observations made during the cruise. The thickness values are plotted as a colour coded bar graph above the seafloor reconstruction

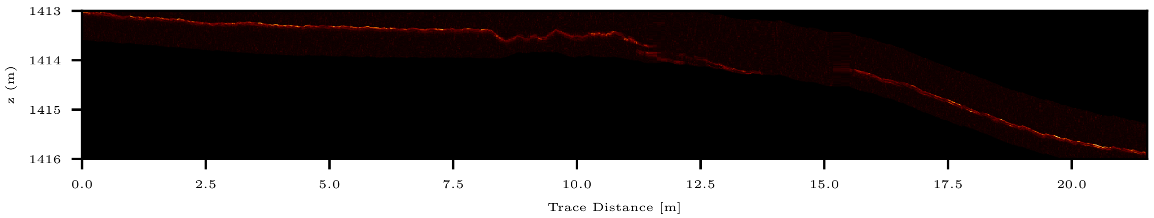

(a) Image frame after interpolation into distance axes

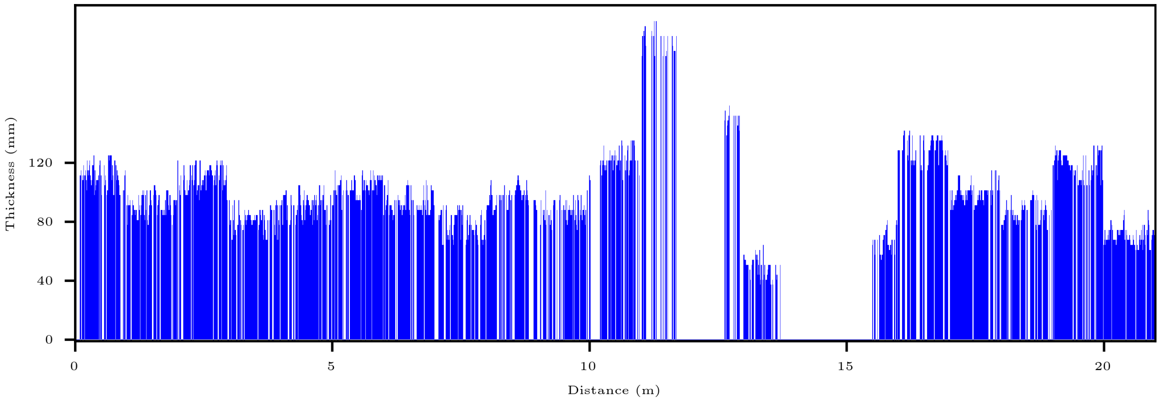

(b) Estimated thickness values

Figure 3-15: Edge detection and thickness estimation

in Fig. 3-16. The figure shows that the detection is consistent with the coverage of crust, with no reflections identified over sand section in the middle of the patch.

3.4 Data fusion and volumetric estimation

The thickness measurements made in the previous step lie along a zigzag line roughly along the approximately 1.5 m wide 3D map. While the whole 3D map is divided into uniform sized cells, only about 7 % of the cells would have a thickness calculated. Since the thickness of Mn-crusts are assumed to be constant over the range of several meters, the measured thickness value is extrapolated into all crust cells and the volume of crust present in the area is calculated by integrating the crust cover. By using a moving window technique, percentage coverage and mass coverage of crust are calculated along regular intervals.

In order to extend the thickness measurements to all the mapped areas, extrapolation techniques are employed. For a cell i, a window of influence J_i is defined as

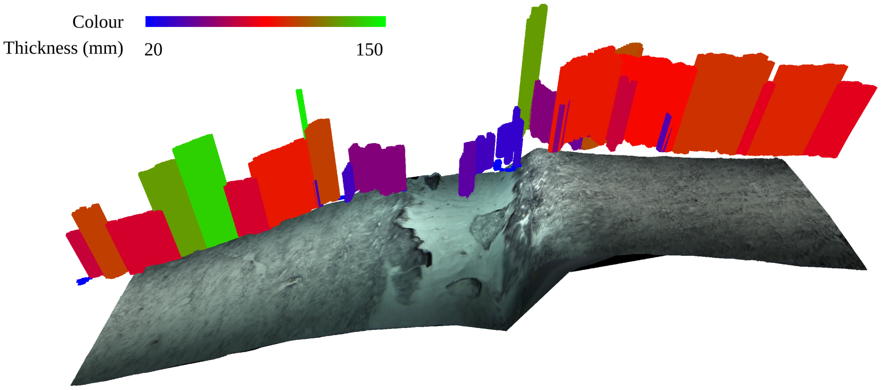

Figure 3-16: Colour coded output of thickness plotted over the 3D map

the set of all cells within a threshold distance d_{th} from the centre of i. The number of cells in set J_i is calculated to be N_{J^i} and the number of crust cells is calculated to be C_{J^i}. Assuming $\hat{J}_i$ to be the set of all cells inside J_i where a thickness measurement is made, the thickness of the crust at i is calculated as a weighted sum of thickness values of $\hat{J}_i$

$$t_i = \begin{cases} \frac{\sum_{j \in \hat{J}_i} w_j t_j}{C_{\hat{J}_i}} & \text{if } C_{\hat{J}_i} > 0 \\ 0 & \text{otherwise} \end{cases} \tag{3.16}$$

where $C_{\hat{J}^i}$ is the number of crust cells within $\hat{J}_i$. The weight w_j of each measurement t_j is calculated as an inverse function of euclidean distance from cell j to cell i (d_{ij}).

$$w_j = 1 - \frac{d_{ij}}{d_{th}} \tag{3.17}$$

The local percentage coverage of exposed Mn-crust deposits (Ψ_i) about i is calculated as

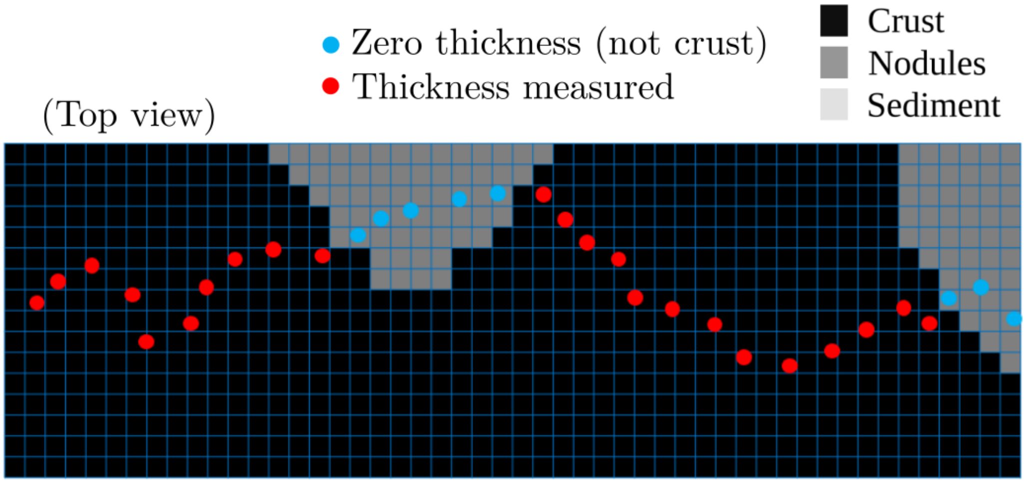

(a) Seafloor map classification and thickness measurements

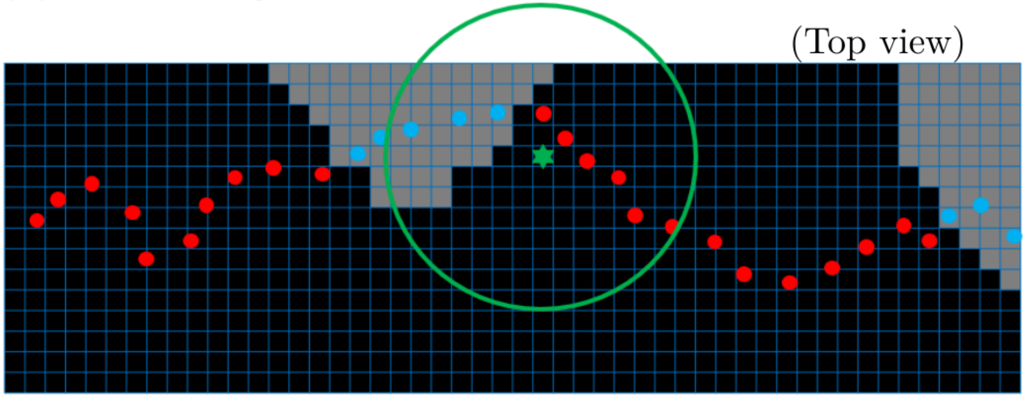

(b) Window of influence about the kernel denoted by green star

Figure 3-17: Representative diagram of thickness extrapolation to all areas classified as Mn-crust by the classifier

$$\Psi_i = \frac{C_{J^i}}{N_{J^i}} 100 \tag{3.18}$$

Using the density of Mn-crust (ρ) calculated from samples collected in the area, the local mass coverage per unit area of Mn-crust about i can be calculated as

$$M_i = \frac{\rho \sum_{j \in J_i} t_j}{N_{J^i}} \tag{3.19}$$

The window of influence J_i is then moved to the next point where a thickness measurement was taken and the calculations are repeated, to estimate the distribution of crust along the entire mapped area.

3.5 Error analysis

In this section, the error in the measurement process is analysed in detail in order to estimate an accuracy of the proposed method. The sources of error in the measurements are propagated as systematic errors depending on the parameters in the calculation.

The 3D mapping system has an 1-sigma uncertainty of 9.17 % affecting the total mapped area (δ_A). The thickness measurements are subject to a 6.1 % variability (δ_t) in the velocity of sound ($2932 \pm 179\, m/s$) in Mn-crusts Thornton et al. (2013).

$$\delta_t = 6.1\% \tag{3.20}$$

The percentage cover has 10 % uncertainty (δ_Ψ) from classification (cross validation accuracy - see section 3.2).

$$\delta_\Psi = 10\% \tag{3.21}$$

In calculating the total amount of Mn-crust present in the area, a 1.9 % variability in the density of crust ($1920 \pm 36\,kg/m^3$) is also considered Thornton et al. (2013) (δ_ρ). Thus the total error in the mass of the Mn-crust becomes

$$\delta_M = \delta_A + \delta_t + \delta_\Psi + \delta_\rho = 27.2\ \%. \tag{3.22}$$

Counter-intuitively, since the mass per unit area is calculated by the averaging the thickness of kernels and multiplying by the density within the threshold region, the error in area measurements do not have an influence.

$$\delta_\Lambda = \delta_t + \delta_\Psi + \delta_\rho = 18\ \% \tag{3.23}$$

3.6 Summary

This chapter described the methods developed for identifying crusts, calculating thickness and extrapolating results to the entire mapped region. The implementation of the methods on the field data collected and analyses will be described in the next chapter.

Chapter 4

Field Survey Results

Takuyo Daigo seamount is a guyot in the northwestern Pacific ocean, part of the Marcus-Necker seamounts group and is known to have thick deposits of Mn-crusts Usui et al. (2017). The southern slopes of Takuyo Daigo seamount was selected for the field trials of the proposed system. This area is surveyed by researchers for the past decade, several systems have been deployed and samples were collected. The CRC system was used in 4 cruises conducted over 5 years from 2013 until 2017 and multiple transects in a hectare scale region was surveyed at depths between 1350 m and 1600 m below sea level.

This is the largest ever dataset collected of Mn-crusts in a multi-modal survey. An overview of the the surveys and the data available is described in section 4.1. A detailed analysis is described in the following sections. Finally, a statistical analysis of the samples available from the area is compared with the results of the proposed framework.

4.1 Overview of field surveys conducted

During the first cruise to the area, the system was mounted on ROV Hyper-Dolphin to follow a continuous crust deposit. The remaining dives were done during the latter cruises using the AUV Boss-A, and surveyed the seafloor following predefined waypoints. A summary of the dives are shown in Table 4.1.

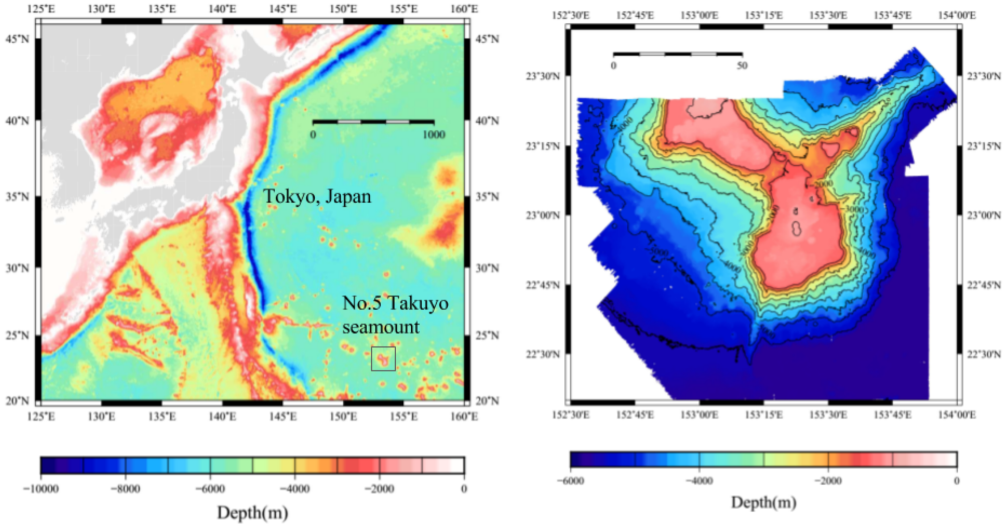

Figure 4-1: Takuyo Daigo seamount is a guyot located in the northwestern Pacific ocean.

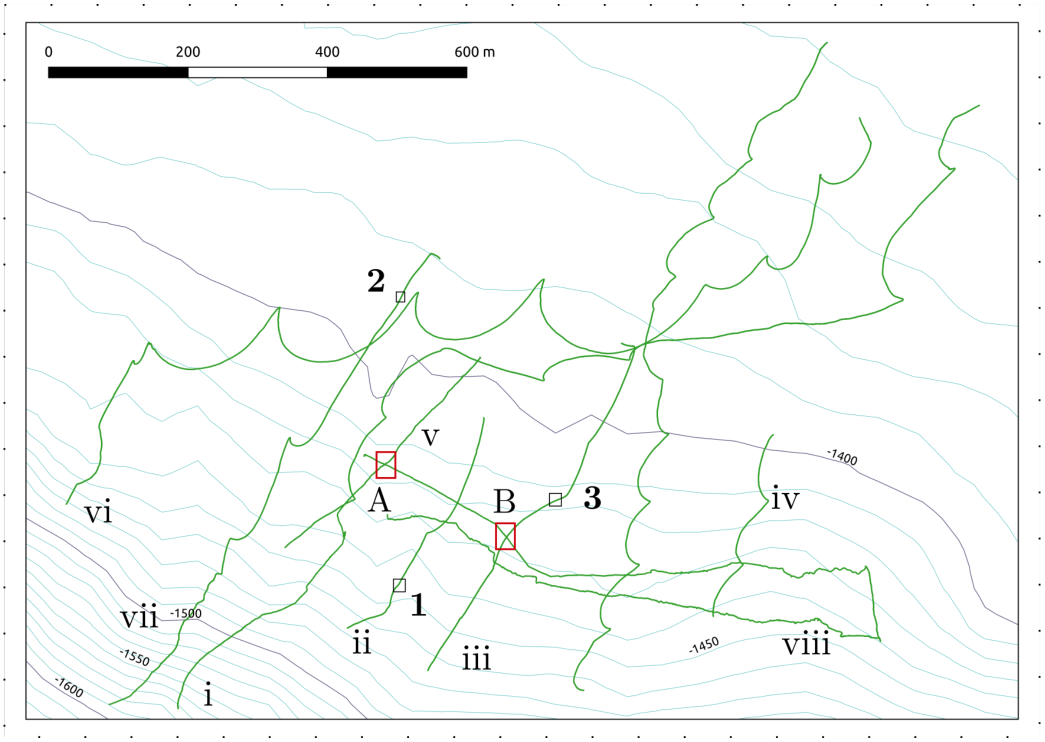

Figure 4-2: Navigation transects of all the surveys done at the location.

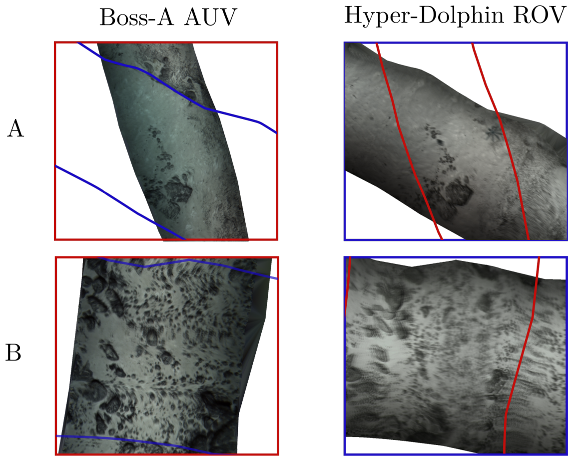

Figure 4-3: Two locations where the transects intersect are selected for inter-comparison between AUV and ROV collected data (See Fig. 4-2 for the locations). The blue outline shows the ROV transects and the red outline indicates the AUV transects.

Table 4.1: Summary of field experiments conducted at Takuyo Daigo seamount in the northwestern Pacific ocean.

Vehicle	Number of dives	Lateral distance surveyed (m)	Observation speed (m/s)	Observation time (min)
Hyper-Dolphin (ROV)	1	3636	0.15	312
Boss-A (AUV)	5	7217	0.1	931

4.2 Typical seafloors examples

Various types of seafloor and the variation in crust type and coverage The implementation of the proposed workflow on various types of seafloor observed during the dives are shown in the following subsections. Section 4.2.1 describes the analysis of a continuous flat crust deposit. Section 4.2.2 describes a seafloor section with transitions from sediment to nodules, followed by section 4.2.3 which describes a seafloor section containing all seafloor types. Compiling results from all dives, section 4.3 describes the regional distribution of Mn-crust in the surveyed region. Section 4.4 analyses the results obtained in section 4.3 in detail and estimates the errors involved.

4.2.1 Continuous flat Mn-crust deposits

The steps in analysing a seafloor section to estimate crust distribution is shown in Figs. 4-4 and 4-5. They show a seafloor section consisting of a flat continuous Mn-crust layer which is about 6 m in length and 1.5 m in width. Fig. 4-4(a) shows the top view of the 3D reconstruction with the red dots showing the locations of acoustic measurements. Towards the right, a short vertical drop, seen in the reconstruction as a white vertical strip, is present where the crust breaks off and the broken slabs can be seen immediately afterwards. A small sediment section separated the two. The acoustic reflections recorded by the probe are shown in Fig. 4-4(b). The seafloor is classified into crusts, sediments or nodules using the algorithm presented in section 3.2 and the results are shown in Fig. 4-4(c). A breakage in the map can be seen near the vertical drop, caused by the shadowing of the 3D map near the cliff. It can be observed that, other than a small section in the middle, all the measurements are made over Mn-crust. A thickness value is calculated for points (red dots in Fig. 4-4(a)) which lie on kernels classified as crust as shown in Fig. 4-4(d). The horizontal axis of the plots represents the distance corresponding to the trace of the acoustic measurements on the seafloor. Due to the gimbals continuously orienting the acoustic probe so that the pulse is normal to the seafloor, the trace of the measurement locations is significantly longer than the length of the 3D reconstruction. The percentage cover calculated

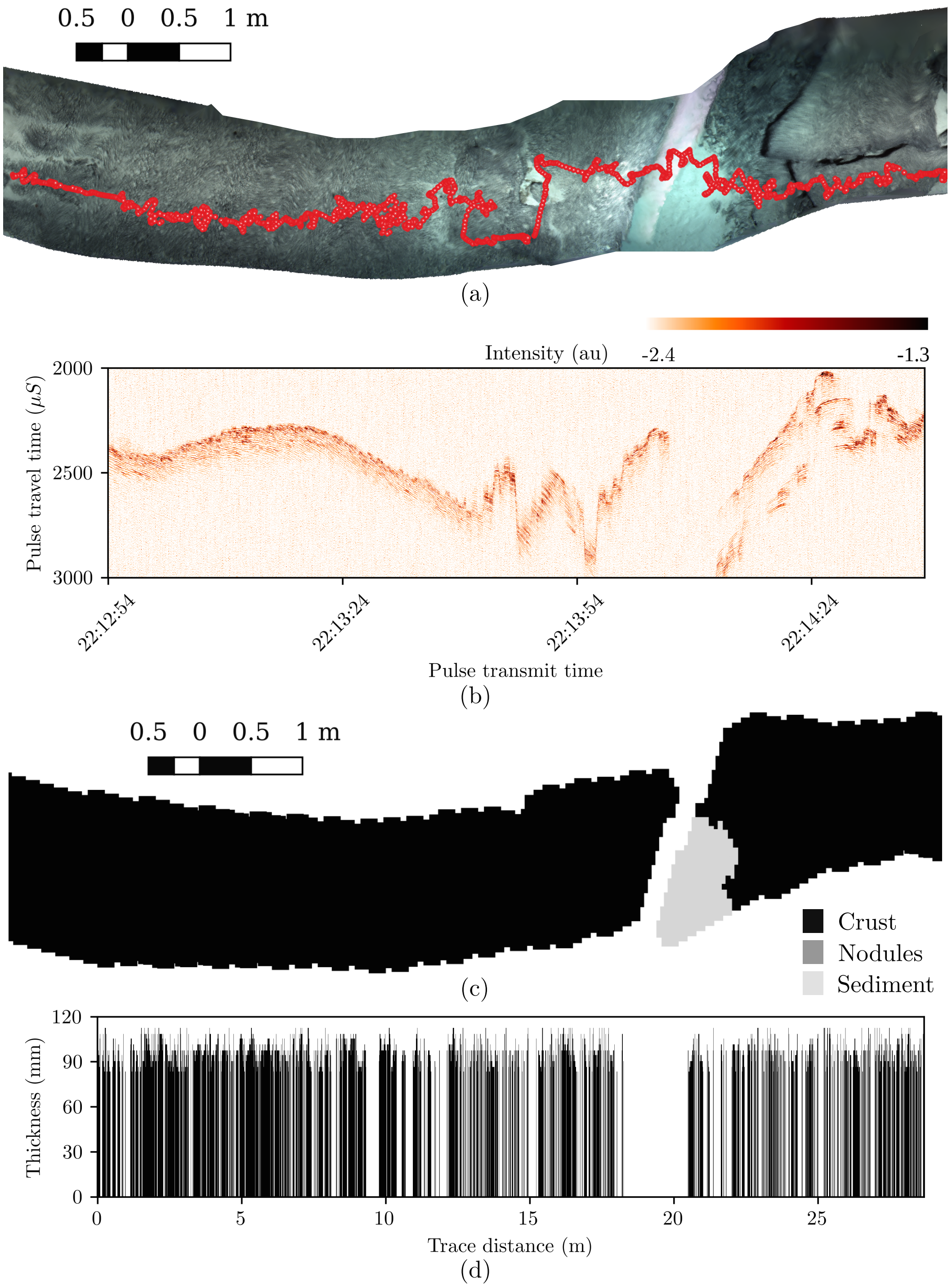

Figure 4-4: Steps in processing the data collected over a flat crust section. The crust layer breaks towards the right and the broken pieces can be seen at the extreme right. A short vertical drop and a small section of sediment separates the two. (a) Top view of seafloor section with locations of acoustic measurements shown as dots. Due to the gimbals continuously orienting the acoustic probe normal to the seafloor, the trace of the measurements follows a zigzag pattern. (b) Acoustic signals recorded. (c) SVM classification. (d) Estimated thickness values.

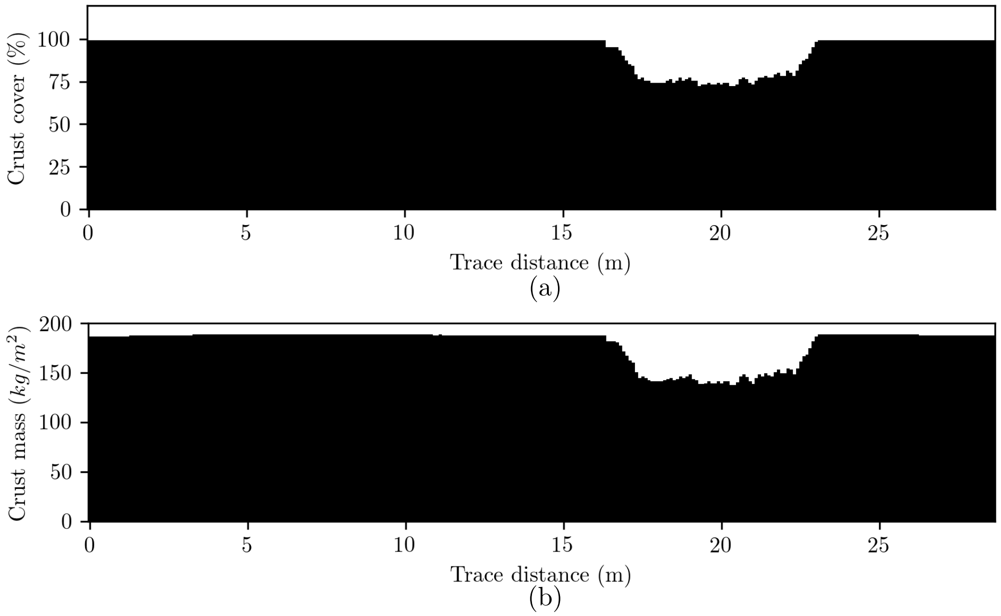

Figure 4-5: (Continued from Fig. 4-4) In processing the data collected, coverage estimates are calculated as described in section 3.4. Since the seafloor is mostly continuous flat crust, the coverage is nearly full throughout, except where the slabs have broken off from the flat crust layer. The horizontal axis denotes the interpolated trace distance along the red dots and is significantly longer than the length of the seafloor section. (a) Percentage coverage. (b) Mass coverage of crust.

using (3.18) is plotted in Fig. 4-5(a). The graph clearly shows the dip in coverage in the middle due to the breakage of crust and a small sediment covered area in the middle. The estimated mass coverage is shown in Fig. 4-5(b). Since the areas are almost completely covered by crust, a high mass per unit area is present.

4.2.2 Sediment to nodules transition

Fig. 4-6 shows a roughly 12 m section of the seafloor scanned using Boss-A and transitions from full sediment cover to full nodule cover. The acoustic signals also shows a clear change from a weak top reflection in sediment covered areas to sharper reflections with change in the type of seafloor. Since no crust coverage is present, a second reflection is not present in the graph and no thickness values were calculated. However, in the beginning and middle areas of the acoustic reflections, a weak second reflection can be seen. These reflections shows a buried layer, which was ignored

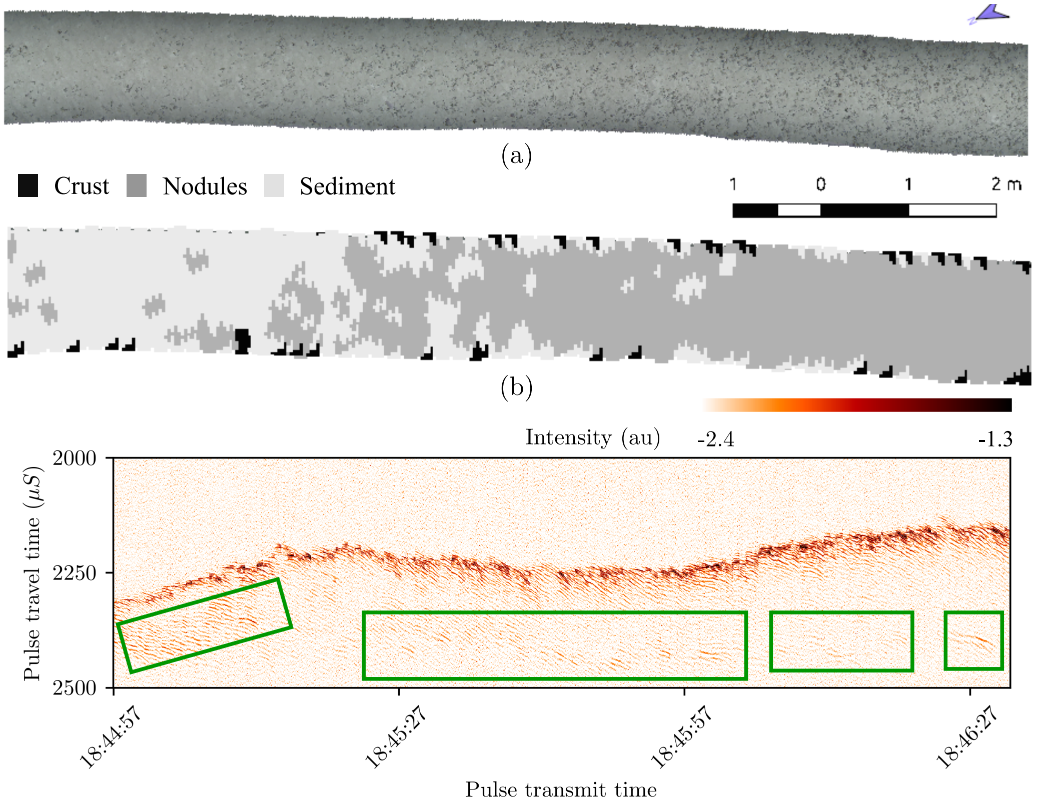

(a)

(b)

(c)

Figure 4-6: A sediment section transitioning into a nodule section. Because no crust kernels were found, thickness values are not calculated. (a) Top view of the 3D reconstruction. The trace of acoustic measurements (see Fig. 4-4(a)) has been omitted for clarity of visualisation. (b) SVM classifier output. Although, some edge artifacts are visible misclassified as crust, they do not affect the final mass estimates. (c) Acoustic signals recorded by the probe, showing no consistent layer of crust. The image shows weak second layers of reflections in areas shown in boxes, presumably from a buried layer of crust.

since the thickness of crusts, if present as a buried layer, cannot be calculated and no visual confirmation can be made of the layer. It can be seen that some edge kernels are misclassified as crust; this is due to the limitation of the color correction method used in generating the 3D maps. In the presented example, this creates a 2.7% error in the percentage cover estimates. However, since the acoustic data is collected along the middle of the transect, which is classified correctly as sand/nodules, acoustic reflections were discarded. Therefore, the error in thickness measurements and final mass calculations are negligible.

4.2.3 Sediment covered flat Mn-crust near a ledge

Figs. 4-7 and 4-8 shows a nearly 12 meter section of the seafloor containing all types. It is centred on a ledge of flat Mn-crust and partially covered by a layer of sediment. Below the ledge, a thick layer of sediment is visible, followed by broken slabs of Mn-crust. Since Mn-crusts are exposed partially, the coverage estimate oscillates between near zero and 80 %. Towards the left, the sparse and weak acoustic reflections indicate a sand layer and a second layer becomes clearer where the crust is exposed. Towards the right, the seafloor is covered in nodules and it shows in the acoustic reflections as strong reflections, but with no secondary layer visible. To the left of the nodules, where a sand section of about 0.8 m is present, a secondary layer is visible in the acoustic reflections; however, the type of the layer cannot be determined with the proposed techniques.

4.3 Final results

The data collected from all the dives are analysed patch by patch as shown in the previous sections and combined together to produce the final results. The measurements are subsampled to 50 cm resolution for clear visualization. These results are shown as Figs. 4-9, 4-10, and 4-11.

4.3.1 Percentage Cover of Mn-crust

Fig. 4-9 shows the percentage cover estimates for the entire mapped area. Since the ROV was used to follow a crust layer, the results show a high percentage cover throughout. These four transects, mapped during a single dive, are indicated using green arrowheads. The remaining transects, mapped by AUV shows a varying landscape that can have anywhere between zero and one hundred percent crust coverage.

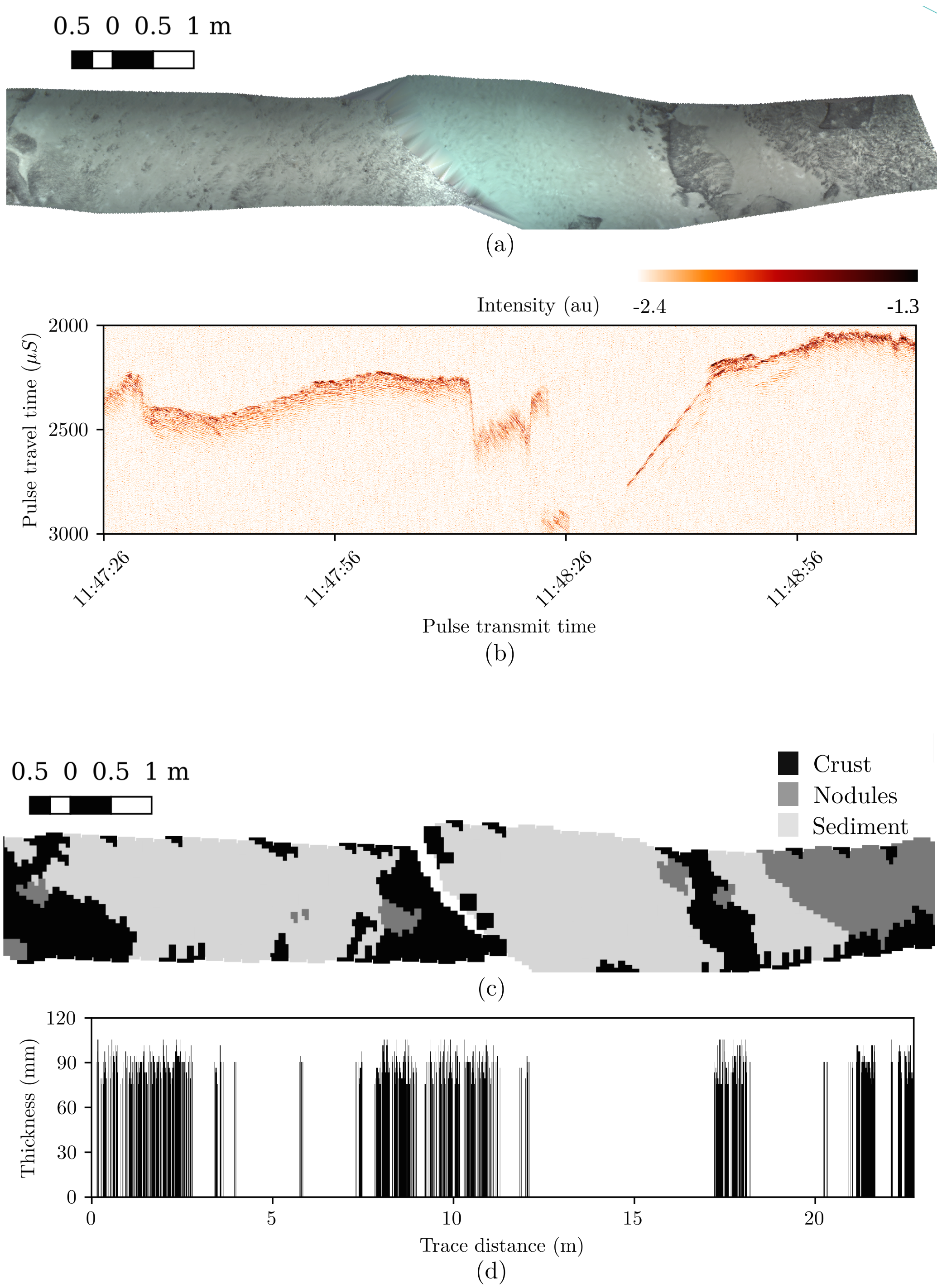

(a)

(b)

(c)

(d)

Figure 4-7: Seafloor section containing a variety of types. Towards the left, the layer of crust is partially covered by sediment and gets broken in the middle. Farther to the right, the sections are covered by nodules. (a) Top view of seafloor section. (b) Acoustic signals recorded by the probe. (c) SVM classification of the seafloor section. (d) Thickness values estimated.

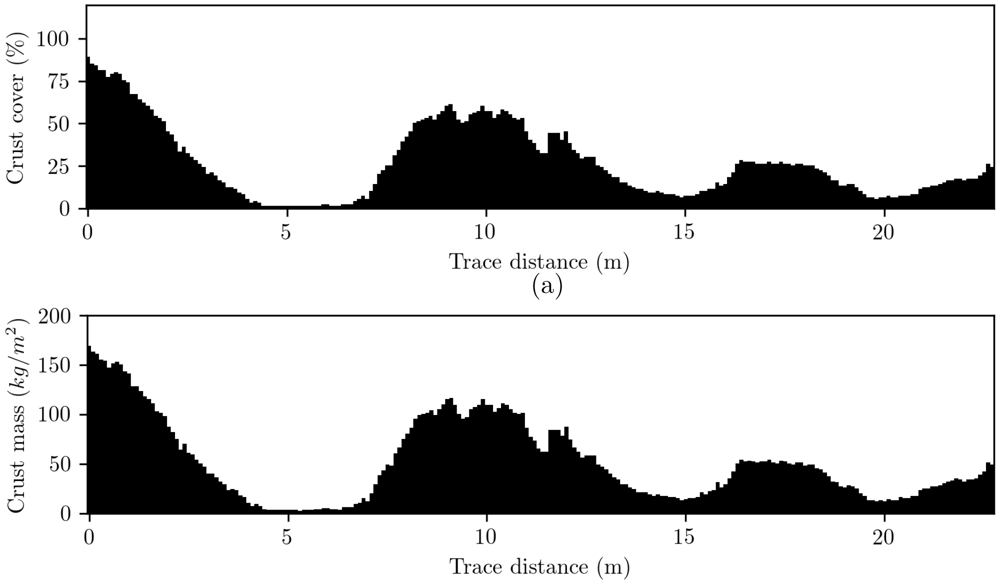

(a)

(b)

Figure 4-8: Analysis results from the seafloor patch with different classes shown in Fig. 4-7. (a) Percentage coverage of crust. (b) Mass coverage of crust. Towards the left side, although it is nearly 100% covered by crust, the layers are thin and hence the mass coverage is only about 75% of the maximum coverage expected in the area.

It can be seen that the lower sections of the seamount, which are also steeper, has a high crust coverage. In some areas, the coverage is seen to vary rapidly. For example, consider the section marked by ★ scanned by the AUV. The upper section has flat continuous Mn-crust deposits, whereas the lower section, only 10 m away, shows a sediment covered seafloor. This high variability in the seafloor classes indicate the need for a continuous measurement system in order to assess the crust volume accurately. Two locations, indicated as A and B in Fig. 4-9, were identified for inter-comparison between AUV and ROV collected data. A close-up view fo the intersections are shown in Fig. 4-3. Crossing A is a sand covered crust area (exposed crust can be seen to the right and top of the intersection) with some rocks. Crossing B is covered with nodules of various sizes.

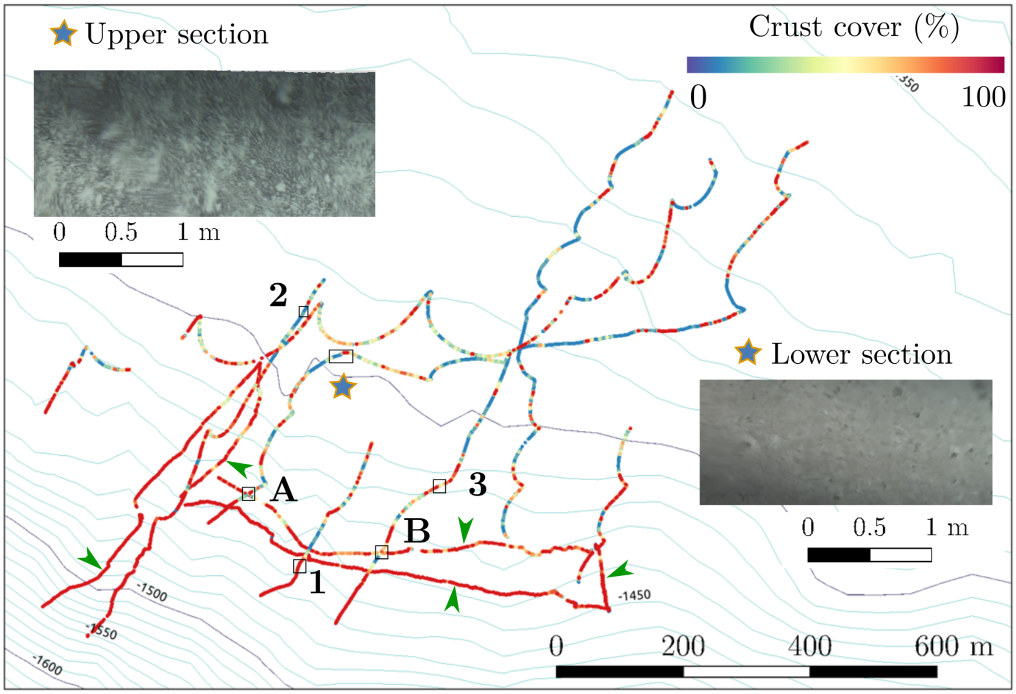

Figure 4-9: Percentage cover of Mn-crust along mapped transects. The 4 ROV transects (shown by arrows) have a higher % cover as regions with exposed crusts were followed manually by the ROV pilots, whereas the AUV used for all other transects followed pre-planned trajectories. Crust coverage can vary rapidly such as in the area marked by ★; very different landscapes only 10 m apart (3D maps shown in insets).

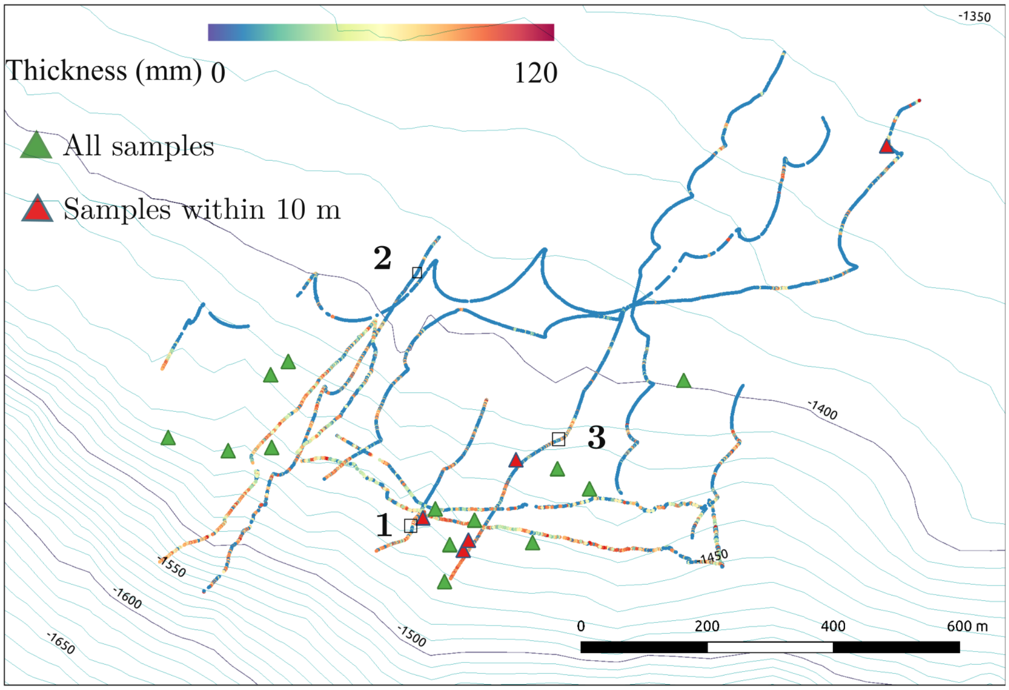

Figure 4-10: Thickness of Mn-crust along mapped transects. The thickness is higher in deeper and steeper sections of the seamount (left bottom area). The samples collected from the visible area and the samples which are close to the mapped area are shown as green and red triangles respectively.

4.3.2 Thickness

The thickness values measured and the samples collected from the area are shown in Fig. 4-10. The relative abundance of crust in the upper and lower sections of the map and the lack of crust in the central regions is observed. Nevertheless, isolated points of thickness can be seen in the central region which originates from single rocks projecting out of the sediment or nodule covered regions. The thickness varies from about 40 mm to a maximum of 114 mm, with a mean thickness of 69.6 mm. A total of 26 samples were collected by researchers in the past in the area covered in the map. The locations of these samples are shown as green triangles. Although there is no overlap between the samples collected and the surveyed regions, 7 samples from 5 locations are close to the mapped within 10 meters of the transect. These samples, shown as red triangles are used for further analysis for comparing the results of the present survey with sampling based methods. This is detailed in section 4.4.

4.3.3 Mass coverage

The final volumetric estimates are shown in Fig. 4-11, which shows the unit crust coverage for every part of the mapped regions. The results vary from zero up to a maximum of 204 kg/m^2. As observed from Figs. 4-9 and 4-10, the lower, steeper sections of the seamount contains maximum coverage of crusts, even though the coverage can vary abruptly in a short range of a few tens of meters.

4.4 Analysis

Due to the harsh inaccessible nature of the deep sea environment, validating the results is an extremely difficult task. Due to the inherent errors in acoustic localization systems, which can be as high as 15 m at the survey depths (assuming a 1% error), it is difficult to visit precisely the same place multiple times. Any validation, therefore must consider the localization error and the varying nature of Mn-crusts.

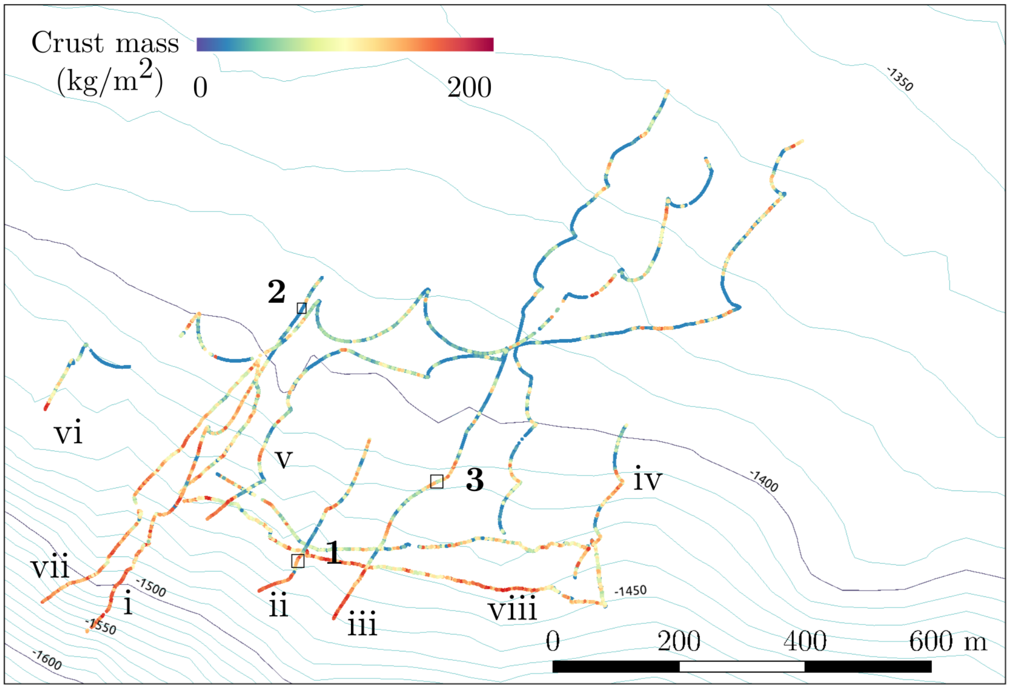

Figure 4-11: Final volumetric coverage estimate along mapped transects. The results vary from nil to 204 kg/m^2, with the maximum crust coverage found in the steeper lower sections of the mapped region.

Table 4.2: List and key specifications of the samples used to validate the proposed method. All the samples are located within 10m of distance from the robotic survey transects.

No.	Date collected	Thickness (mm)	Dimensions (cm x cm x cm)	Weight (kg)
s1	2013.6.30	90	30x30x10	10.8
s2	2013.6.27	65	77x48x9	50
s3	2009.02.17	30	9x8x7	0.6
s4	2009.02.17	25	9x14x5	1.1
s5	2009.02.16	80	41x31x12	15
s6	2009.02.16	90	15x11x9	0.9
s7	2009.02.16	30	26x18x11	6.4

Since the operation of the acoustic probe has been validated using samples recovered from the site in a laboratory environment Thornton et al. (2010), this research only focuses on validating the results in the field. The primary method of validation is the comparison of sample thicknesses with the nearest measurements; this is done in section 4.4.1. A statistical comparison of the overall samples and overall measurements is made in section 4.4.2. Finally, the assumption concerning the variability of Mn-crust deposits is examined in the section 4.4.3.

4.4.1 Validation using samples collected

Using the samples collected within the survey area by other researchers during past cruises, the results of the proposed method was validated. Although at no point, the survey transects overlapped with the sampling locations, a total of 7 samples were identified from 5 locations, which were reasonably close (less than 10 m away) from the robot transects. These were collected by scientists during previous cruises (JAMSTEC 2009, 2011, 2012, 2013).

Table 4.2 lists all the samples and their specifications. These samples are compared with the nearest thickness measurements as shown in Figs 4-12-4-16.

Sample s1 is shown in Fig. 4-12. This sample was collected from a point about 9 m away from the BSA31B dive, in the direction indicated by the red arrow. Top view

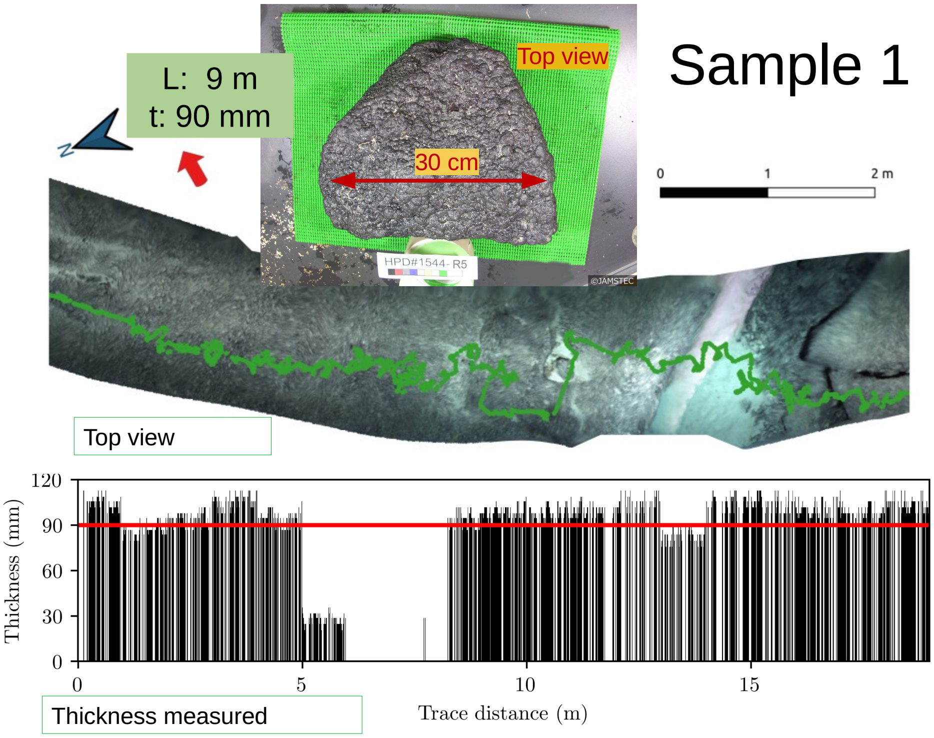

Figure 4-12: Validation using sample 1

of the 3D reconstruction of the nearest seafloor section is shown with the thickness calculated by the proposed algorithm is plotted below. The locations of the thickness measurements are plotted as green dots on the 3D map. A red horizontal line shows the thickness of the sample for easy comparison. It can be seen that the sample thickness is 90 mm and falls within the range of thickness values measured by the proposed system in the area.

Sample s2, collected from a sand covered crust region, is shown in Fig. 4-13. With a thickness of 65 mm, this is almost same as the thickness levels observed in the area. Samples s3-s7 are also shown in the following figures. Despite being collected from a variety of landscapes, and varying thicknesses, the match between the measurements and the samples is clearly observable.

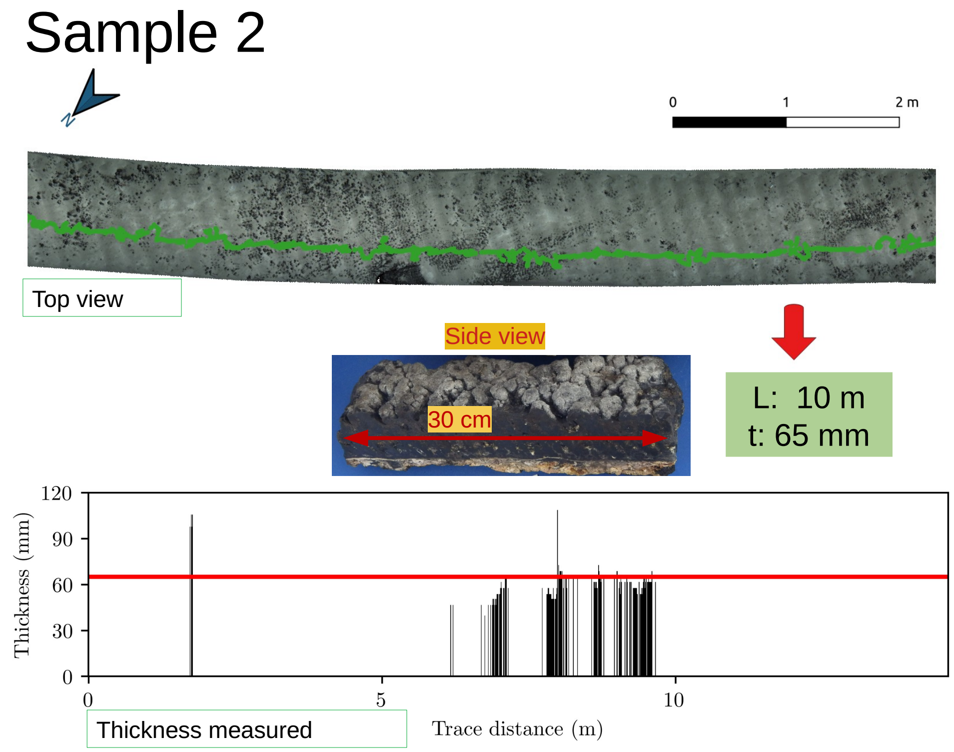

Figure 4-13: Validation using sample 2

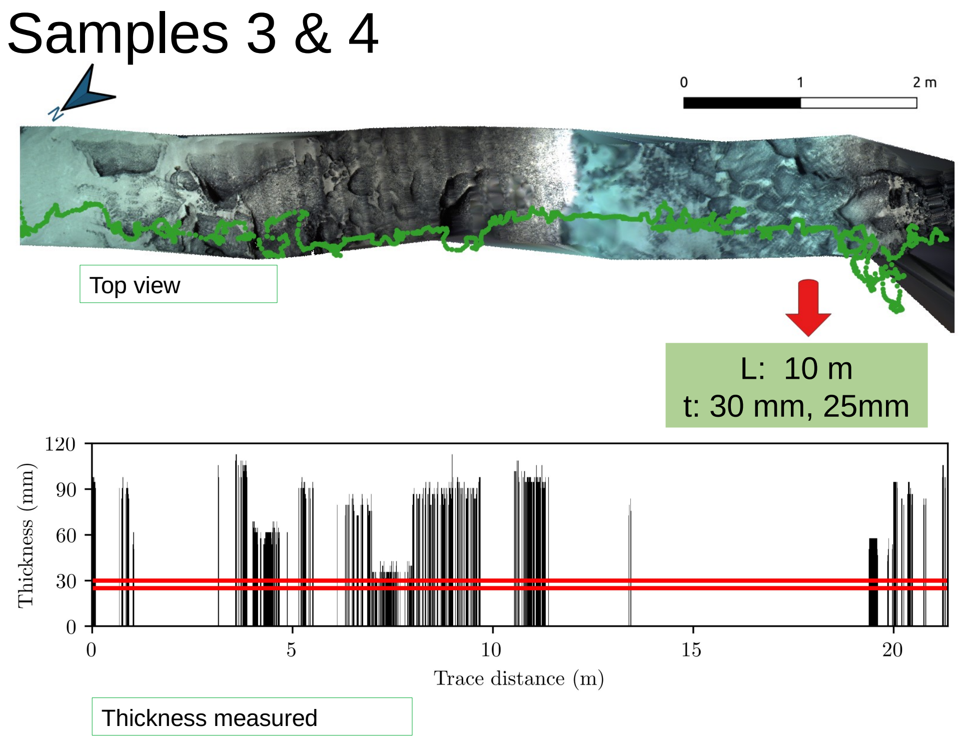

Figure 4-14: Validation using samples 3 and 4

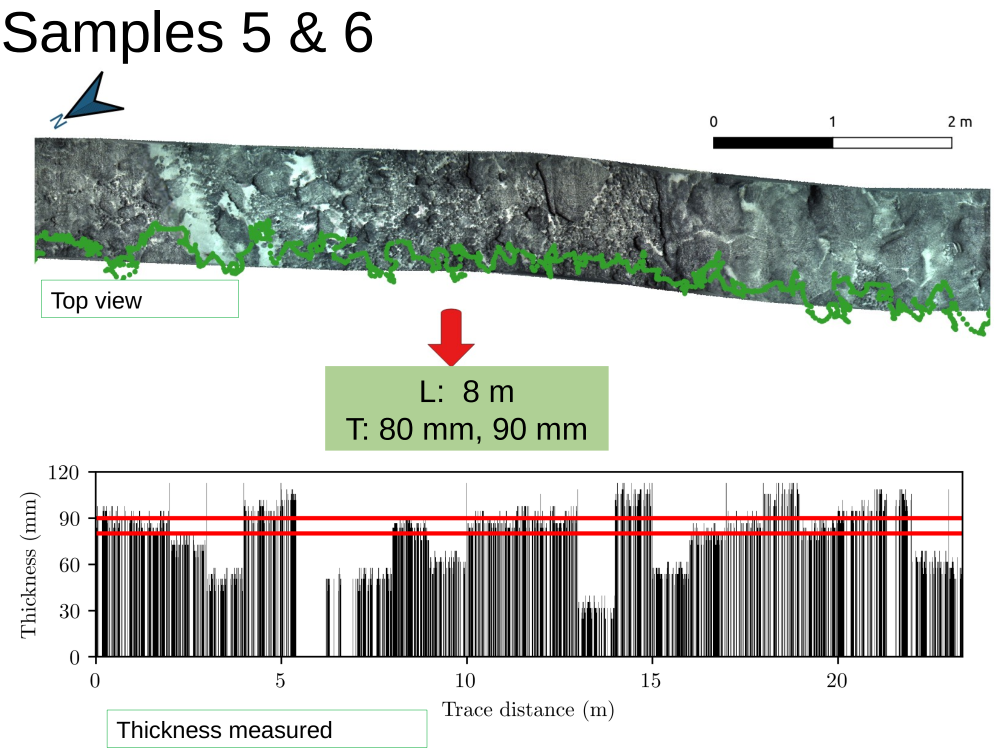

Figure 4-15: Validation using samples 5 and 6

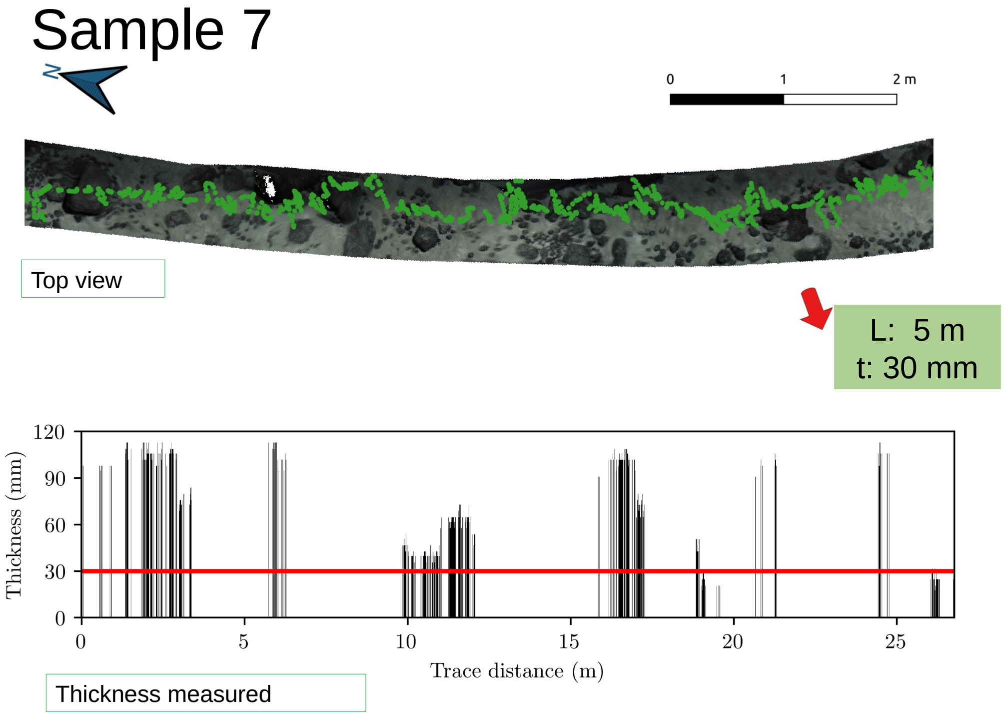

Figure 4-16: Validation using sample 7

Table 4.3: A summary of the estimated Mn-crust resources at Takuyo Daigo seamount measured along a total transect length of 10.9 km (see Table 4.1 for survey details). An uncertainty value is provided in the brackets for each of the estimates. The variability of estimated values indicates the contrasting nature of the Mn-crust deposits. An indicative estimate using only samples collected from the same area, shows that a continuous in-situ survey is required to assess Mn-crusts with high accuracy.

Parameter	Proposed method		Samples N=7	
	Mean ($\pm\sigma$)	Variability ($\pm\sigma$)	Mean ($\pm\sigma$)	Variability ($\pm\sigma$)
Total area mapped (m^2)	12,510 (±1150)	-	-	-
Percentage cover (%)	52.0 (±5.20)	±39.0 (±3.90)	-	-
Thickness of crust (mm)	69.6 (±4.25)	±18.7 (±1.14)	63.3 (23.9)	29.5 (11.2)
Crust per unit area (kg/m^2)	69.6 (±12.5)	±59.7 (±10.7)	63.2* (±31.4)*	22.1* (±10.1)*
Amount of crust (t)	870 (±237)	-	791* (±466)*	-

* Visual mapping data for area estimates is used to calculate this value.

4.4.2 Error analysis and validation of results

Accurate quantitative estimates of Mn-crust was obtained over large areas using the instruments and methods described, showing an abundance of Mn-crust in the surveyed region. A summarized description of the results along with the variability and estimates of uncertainty for each measurement is provided in Table 4.3. The variability is calculated as the one-sigma deviation from the mean value. The uncertainty is estimated as the error in measurements on the mean and variability values.

The calculations of error levels was presented in section 3.5. It is estimated that there is 870 tonnes of Mn-crust in the mapped area, with an uncertainty of 237 t. The value of crust per unit area has an uncertainty of 18 % and the calculations show the amount of crust per unit area to be 69.6 kg/m^2 with an uncertainty of 12.5 kg/m^2. However, particularly notable is the variability of $59.7(\pm 10.7) kg/m^2$, which is 85.8% of the mean value. This value is consistent with the initial observation that crust deposits are highly variable and therefore require a continuous in-situ measurement scheme to accurately map its distribution, such as the AUV survey conducted in the present work.

A comparison of the results along with the estimate values made using only samples is included to show the advantages of the proposed method. Since a percentage cover estimate cannot be calculated from ROV sampling dives, percentage cover estimates calculated in the previous step are used instead. Samples taken in an area within a distance of 10 meters of the mapped region was considered, which show a mean thickness of 63.3 mm with a standard deviation of 29.5 mm. A total of 7 samples are selected, which are collected from 5 locations as indicated in Fig. 4-10. The limited number of samples constitute a large statistical error of 37.8 % in sample thickness measurements. It can be seen from Table 4.3 that the final estimated crust mass per unit area and the total amount of crust in an area equal in size to the mapped area has an uncertainty of 49.7 % and 58.9 % respectively, which is extremely high and renders any estimates of crust distribution practically invalid. This arises due to the high variation in crust coverage, with the percentage cover being 52.0 % with a variability of 39.0 %. This information can be calculated only by doing a detailed seafloor survey such as the present one.

In order to study the spatial distribution of Mn-crust over the scale of hundreds of metres, crust per unit area and its variance for each transect (see Fig. 4-11 for transect numbers) is compared in Fig. 4-17. These transects are roughly parallel in most places and are spaced between 100 to 250 m in the lower sections. The bar charts to the right show estimates made by randomly selecting a fixed number points, equally from each transect, to simulate sampling where the total number of points considered is shown. The error bars indicate the systematic error for the full data, and the standard deviation of 50 iterations for each random selection of point location. The systematic error is not shown in the random point samples to illustrate the level of uncertainty that would be expected if an equivalent number of samples was recovered. A larger number of points provide a more representative estimate of the crust coverage where the statistical error levels become comparable to the systematic errors in the proposed

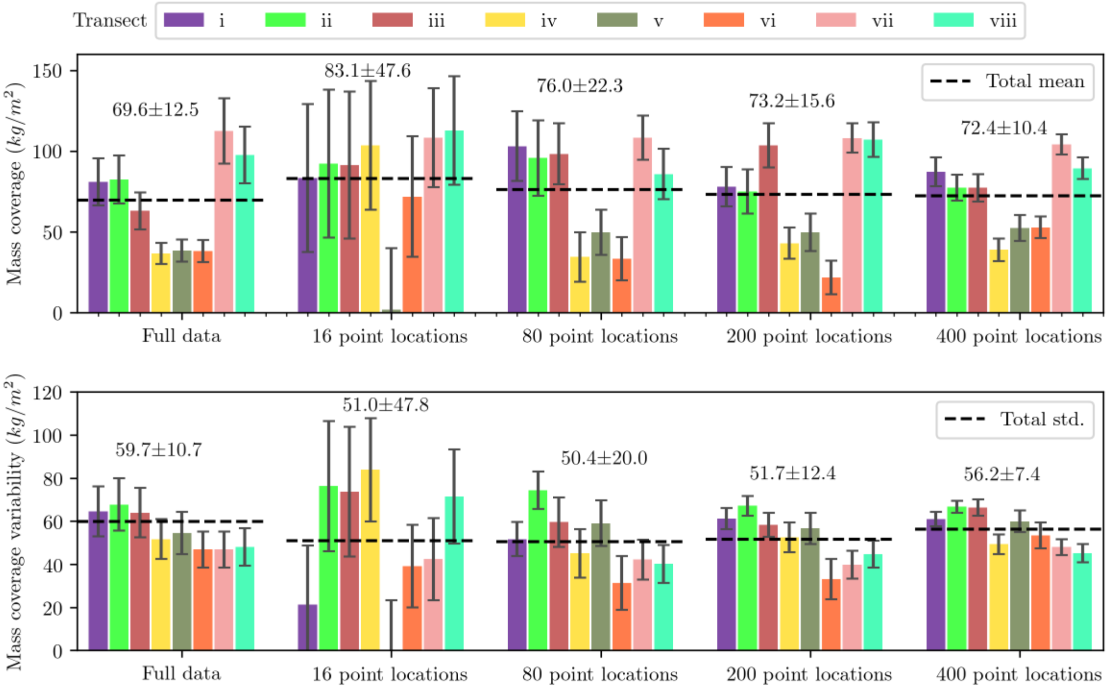

Figure 4-17: Mass coverage of each transect shown in Fig. 4-11 and its variability. This is compared with a simulated sampling scenario, by randomly selecting points from the surveyed data. Mean value and error for each dataset is written above the bars. Variations among transects shows that extrapolating the results from a single transect to the whole area can result in erroneous estimates. The error values indicate that >200 random samples are required for getting an accuracy comparable to the proposed method.

method after 200 random points. Even with 200 locations sampled, which would take approximately 8 days of bottom time for ROV sampling, the spatial variability still influences the estimates (e.g transect iii), indicating further sampling is required to capture the variability between adjascent transects. The variation in estimates among transects indicates that extrapolating results from a single transect over the entire mapped area can lead to highly inaccurate results. Multiple surveys at different locations are required to accurately estimate crust coverage and volume.

The high presence of uncertainty in surveys based on sampling, as compared to AUV surveys, arises due to the significantly smaller number of measurements. In acoustic surveys from an AUV, there are over one million measurements and thus the statistical error is negligible. Only the 6.1 % systematic error, due to the variability

Table 4.4: Divewise comparison of results. The variation in thickness and percentage cover of crusts in the nearly parallel transects indicates the variable nature of the distribution of Mn-crusts.

Transect	Dive	Length (m)	Area (m^2)	Thickness (mm)		Percentage cover (%)	
×	number	×	×	Mean	Variability	Mean	Variability
i	BSA31A	956	970	78.0	15.0	54.1	39.3
ii	BSA31B	413	462	81.7	13.1	52.5	40.3
iii	BSA32	722	921	78.0	15.0	42.0	38.7
iv	BSA38	1523	1759	64.8	16.6	29.3	36.7
v	BSA39	1934	2314	69.1	17.4	28.9	35.6
vi	BSA40	1798	1286	59.9	19.8	33.0	34.6

in the speed of sound, needs to be considered. On the contrary, the thickness of samples can be measured with high accuracy, making the systematic error almost zero. Nevertheless, the statistical error is high and can be reduced only by increasing the number of samples in the given area. However, in order to produce an uncertainty less than the systematic error in the acoustic measurements, a minimum of 268 samples have to be collected from the surveyed region. Since sampling using ROVs takes approximately 40 min to 1 h Usui et al. (2017), collecting so many representative samples is practically unfeasible.

4.4.3 Local Variability of Mn-crust

In order to study the spatial distribution of Mn-crust over the scale of hundreds of metres, the results from each dive is compared in Table 4.4. These transects are roughly parallel in most places and are spaced between 100 to 250 m in the lower sections. It can be seen that the thickness varies a maximum of 17 % from the average thickness over the entire area; while the percentage cover shows high variations of upto 46 %. This indicates that extrapolating results from a single transect over the entire mapped area can lead to highly inaccurate results. Multiple surveys at difference locations is required to accurately estimate crust coverage and volume.

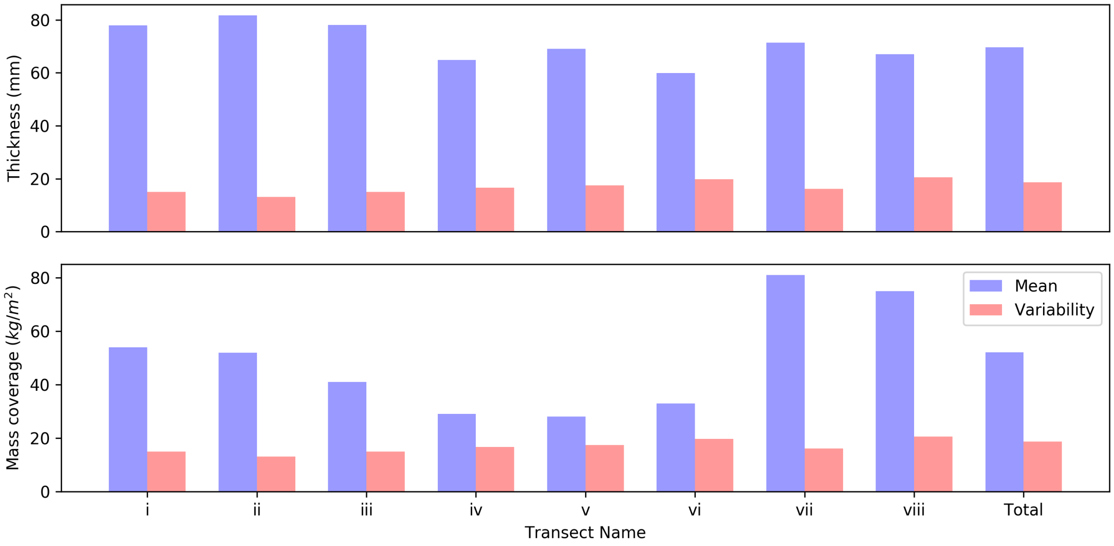

Figure 4-18: Comparison of results by transect. It shows that extrapolating results from a single dive to a large region can be highly erroneous.

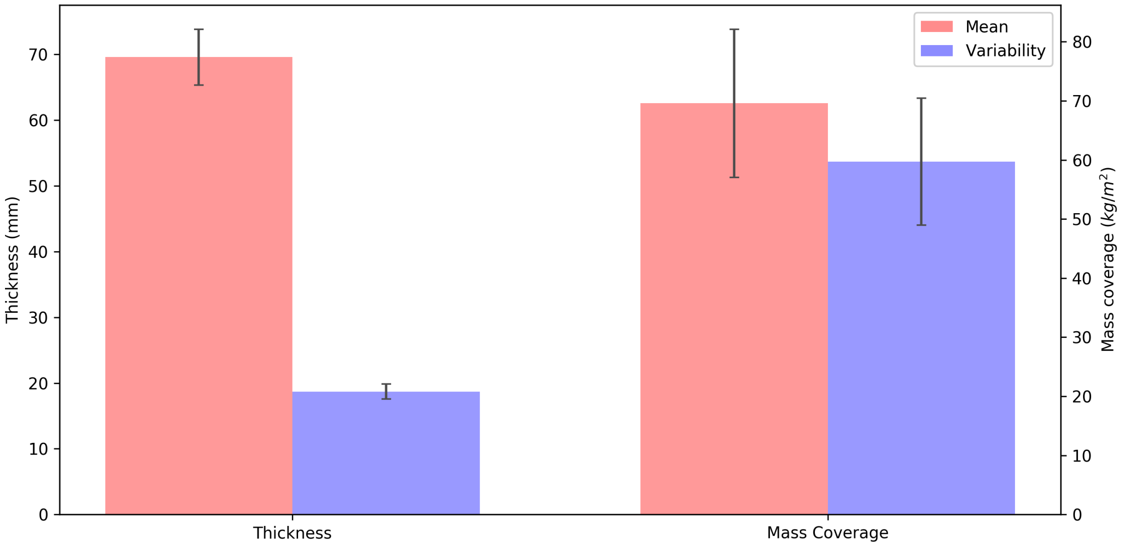

Figure 4-19: Results of the crust distribution values in the surveyed region.

The results obtained can be expanded to larger areas using traditional methods such as kriging (Cressie 1990) in order to compare results. However, this is beyond the scope of the present topic.

4.5 Summary

This chapter described the results from applying the proposed method on the data collected by the field surveys conducted.An analysis of the results indicated the scope and necessity of continuous in-situ measurements for assessing the distribution of Mn-crusts.

Chapter 5

Conclusions and Future Work

In-situ measurements of the distribution of Mn-crust in hectare scale regions have been performed using unmanned robots for the first time. Building upon previous works for Mn-crust in-situ surveys, a scalable data processing framework and improved algorithms made large data processing possible. By using machine learning tools to analyze visual 3D maps to accurately identify exposed crusts and acoustic sub-bottom sonar measurements to identify its thickness, the results are combined to calculate the total mass and distribution of the Mn-crust available in the region. The measurements were validated using samples collected from near the survey area, which showed a comparable level of thickness values. The proposed method has several advantages over sampling such as more and detailed measurements and continuity in output. Also, sampling is inherently biased towards samples that are easy to collect, and do not characterise regions with no samples, such as nodules, sediments and shallow buried crusts.

The surveys utilized ROVs for following a crust deposit by manual steering and AUVs using predetermined waypoint navigation. While the ROV dives showed high crust coverage due to sample bias, the AUV dives were representative observations of the distribution of Mn-crusts on the seafloor; which clearly showed the high variability in the seafloor types. Further, the smooth, constant altitude navigation of AUV is found to introduce less errors into the generation of 3D maps and thus improving the classification of seafloor. Therefore in-situ acoustic measurements using an AUV and the proposed data processing framework presents a reliable technical approach for surveying large hectare-scale areas for manganese crust volumetric distribution surveys in a span of several days.

5.1 Major contributions of this thesis

- A method was developed for accurately estimating the continuous thickness of Mn-crust deposits with millimetre resolution using in-situ surveys.
- A method was developed for fast and accurate classification of seafloor 3D colour reconstructions. Accuracy levels of >90% was achieved by utilizing both the bathymetric and colour information.
- This is the first attempt for creating high-resolution volumetric estimates of Mn-crusts for hectare-scale areas.
- A framework was developed for processing large amounts of data to estimate the amount and distribution of Mn-crusts.
- The observed results could capture the rapidly varying coverage of Mn-crusts. This points to the need for a continuous in-situ survey for surveying and assessing them accurately.

5.2 Research Impact

The International Seabed Authority has currently issued 4 survey licenses to Japan, Korea, Russia and China for economic and technical assessment of Mn-crust exploitation (ISBA 2018). A total area of $3000\,\mathrm{km}^2$ is assigned to each party. One-third of this area has to be released after 5 years and a further one-third after 10 years. The remaining area can be kept for exploitation. Different methods such as ship-board multibeam surveys, towed video surveys and core drilling are used for surveys are being used by the stakeholders for surveying (Joo et al. 2020, Du et al. 2018).

The proposed method is part of the tools used by Japan Oil, Gas, and Minerals National Corporation (JOGMEC) for surveying Mn-crusts. JOGMEC is the Japanese national agency in charge of the Mn-crust survey and exploitation on behalf of the Japanese government. A press release regarding this is attached in the appendix Institute of Industrial Science (2019).

It is worth noting that, following the example of this system and associated algorithms, a similar acoustic probe was built by a Chinese team of researchers based on the same principles and using some of the proposed algorithms Hong, Feng, Huang, Wang & Xia (2019).

5.3 Limitations and Scope for Future Work

A limitation of the presented system is the inability to identify and quantify buried crust below thick layers of sediment. Researchers have shown the presence of layers of Mn-crust below sediment layers up to several metres thick. Since the current version of acoustic probe can only be used upto 30 cm below the seafloor, while shallow layers are visible, deeper layers of Mn-crust cannot be located. Furthermore, only exposed crusts can be classified using the machine learning system as it only looks at the top surface. Higher power acoustic probes, which in turn require bigger AUVs, are needed to measure deeper into the sediment layer.

Another limitation of the work is that swath of 3D map is only 1.5 m and hence distribution is limited to this area. A better acoustic probe which can operate at higher altitudes may be useful in this regard. An immediate advancement of this dissertation work would be extending analyzing capabilities to wide area long range maps. Scope for future work in this regard, is listed below:

- Use only acoustic data for classification or using a combination of both acoustic and visual data for classification.
- Use long range 3D maps for extrapolating thickness
- Use of multi-robotic systems for wide area mapping

- Use AI based methods for cleaning acoustic signals and better thickness estimates
- Use multibeam backscatter and bathymetric data for seafloor classification in the absence of visual data
- Use of autonomous deployment and recovery of robots, saving costs, labour work and ship duration
- Create larger area estimates of Mn-crust distribution using traditional methods such as kriging and compare the results

Furthermore, this method can be used as a template for extrapolating spatial measurements using a visual or 3D bathymetric map as a basis. This can be used in surveys of benthic colonies and biomass assessments, surveys of methane seeps and hydrothermal vents, etc.

Marine surveys are in a transition phase; while technological capabilities were the biggest bottlenecks in the past, significant progress has been made, and the quality and quantity of data is becoming the new challenge - and hence the opportunity. The proposed algorithm can be an effective step in discovering and extracting useful information.

Figure 5-1 shows an illustration of the deep seafloor survey scenario as imagined by the authors. From pointwise sampling using big bulky vehicles in the past, continuous in-situ surveys using autonomous robots are gaining traction. As the coordination, control and environmental comprehension capabilities of the robots improve, multi-robot systems will become the choice of oceanographic studies. This thesis will be a significant step in improving the comprehension skills - currently implemented offline, but can be made online as computational capabilities improve. By collecting data over larger areas using a wide variety of sensors mounted on multiple robots mapping the seabed simultaneously, large areas can be surveyed in shorter time scales and the resulting data can be analysed automatically to provide valuable information to understand the deep sea environment.

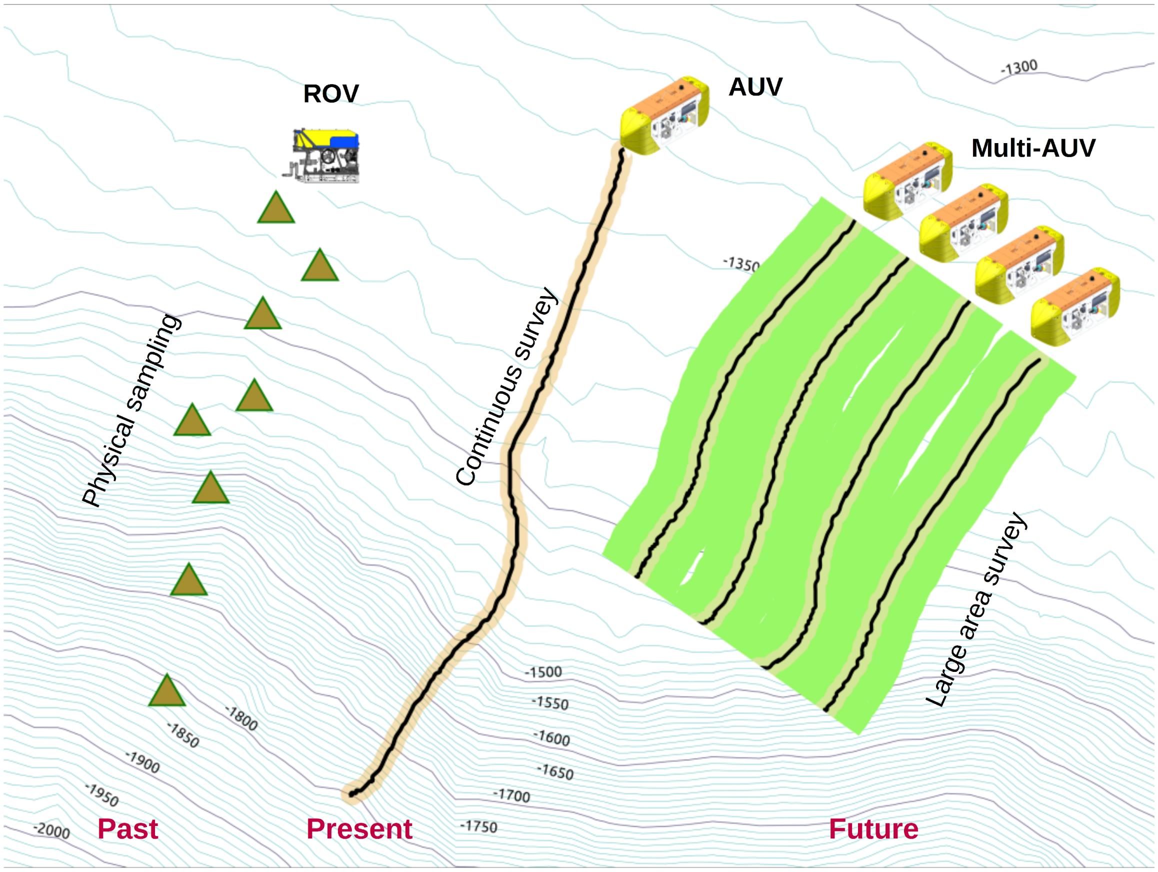

Figure 5-1: Past, present and future of deep sea surveys

Appendix A

Robots

ROVs and AUVs are important tools for deep sea exploration Blidberg et al. (1991), Capocci et al. (2017). In the initial stages of the present research, surveys were done by mounting these sensors on a general purpose ROV, called Hyper-dolphin, described in section A.2. Later, AUV Boss-A, described in section A.1, was developed for this task and was used for collecting a major part of the data.

A.1 AUV Boss-A

Boss-A is an AUV developed for the dedicated task of surveying Mn-crust by the Institute of Industrial Science at the University of Tokyo Nishida et al. (2016). It is rated for 3000 m, which is sufficient for surveying the upper sections of the crust covered seamounts in the Pacific ocean.

Figure A-1 shows the various parts and their location within the AUV. The specifications of Boss-A are shown in Table A.1. The 3 systems - acoustic, visual and navigation systems are marked. The navigation system runs on the main computer of the AUV and is used for real-time control and navigation of the robot and after the dive for post-processing sensor data. The robot uses drop weight ballasts for diving and surfacing, thus conserving battery for the seafloor observation task. The AUV communicates to the surface vessel using an acoustic link which relays critical mission control commands and status information. Also, the AUV can be localized from

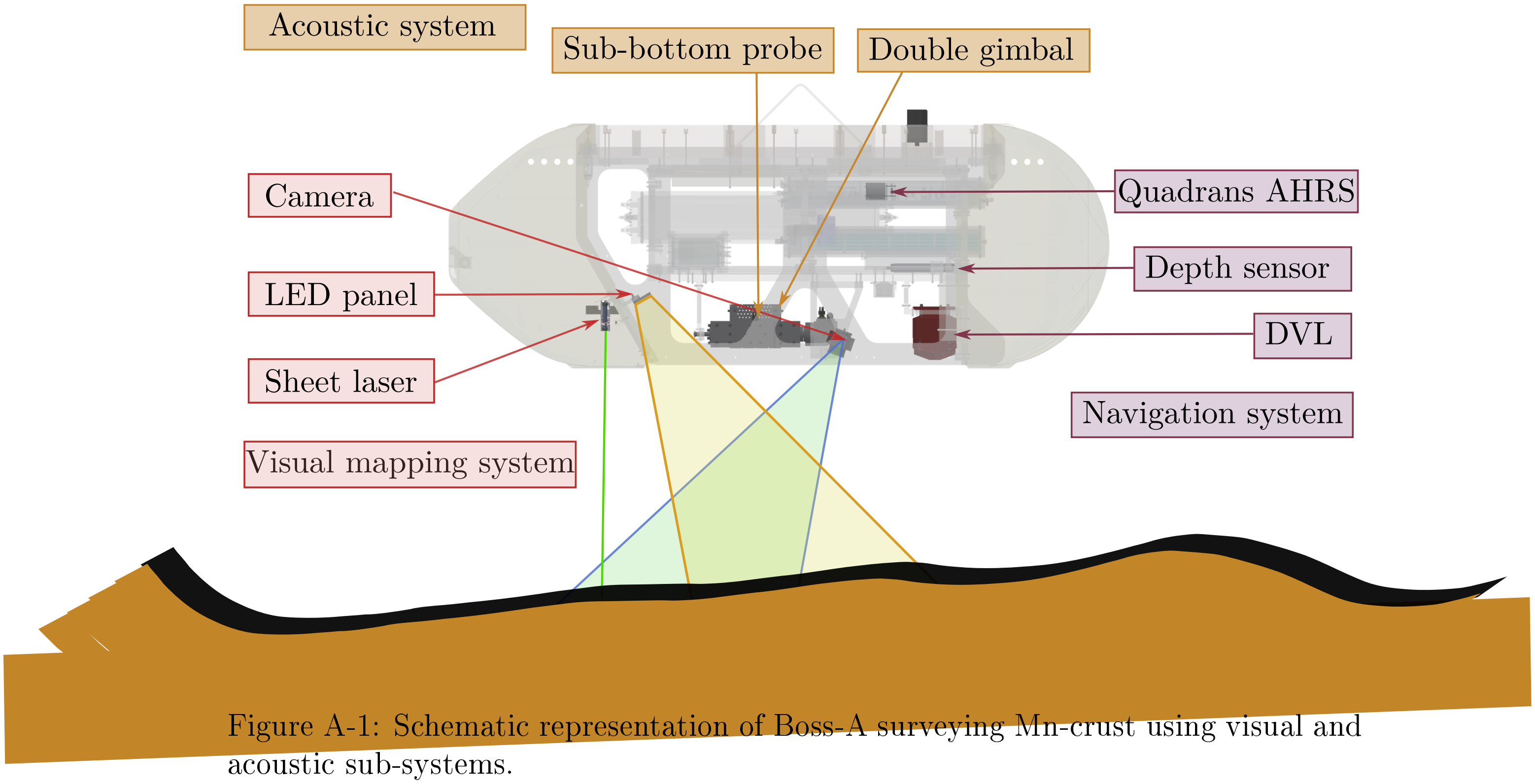

Figure A-1: Schematic representation of Boss-A surveying Mn-crust using visual and acoustic sub-systems.

the mother ship using a Ultra Short BaseLine (USBL) device. This data provides a real time one-way feedback to the researchers on the support vessel about the AUV's location.

An illustration of the mapping scenario and the position of various sensors are shown in Fig. A-1. The AUV follows a preprogrammed path over the seafloor, defined by waypoints, keeping an altitude of $1.5\,m \sim 2\,m$. A Doppler Velocity Log (DVL) is used for localizing the robot, assisted by a depth (pressure) sensor and an

Table A.1: Specifications of the platform (AUV Boss-A)

Dimensions	3.0 m x 0.7 m x 0.7 m
Mass	600 kg
Velocity	1.0 kn (0.5 m/s) - maximum
	0.2 kn (0.1 m/s) - observation
Depth rating	3000 m
Endurance	7 h

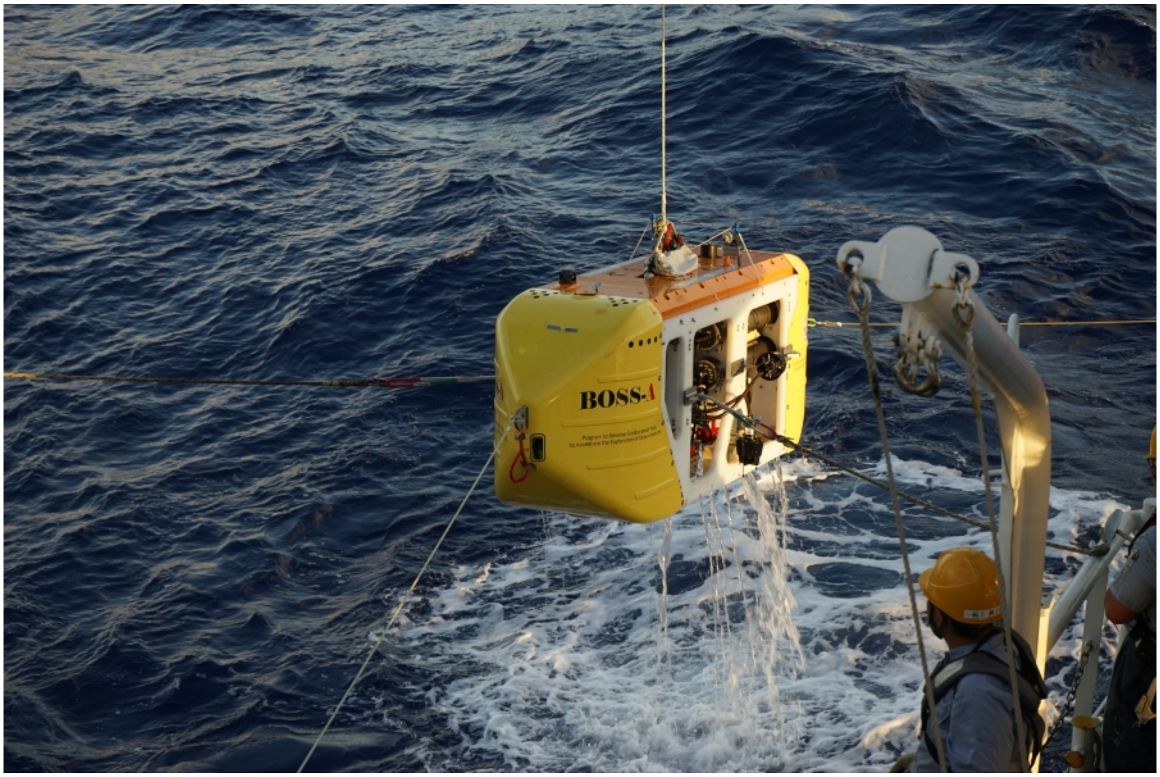

Figure A-2: The AUV BOSS-A being deployed at Takuyo Daigo seamount (Cruise YK17-23C, November 2017, R/V Yokosuka)

Attitude Heading Reference System (AHRS). Critical controls of the robot, such as aborting the mission and skipping of waypoints, is possible through an acoustic link with the ship. The acoustic probe and a double gimbal that constitute the acoustic system, a camera and a sheet laser that are the core components of the visual system and the DVL for navigation are located at the bottom of the robot.

The robot has completed 58 dives in the ocean till date. A photo showing the recovery after a dive is shown in Fig. A-2. For Mn-crust surveys, Boss-A moves at a speed of 10 cm/s, which results in a 3D map with a longitudinal resolution of about 3 mm and thickness measurements with a longitudinal resolution of about 1 cm. Every hour of operation records several tens of gigabytes of data.

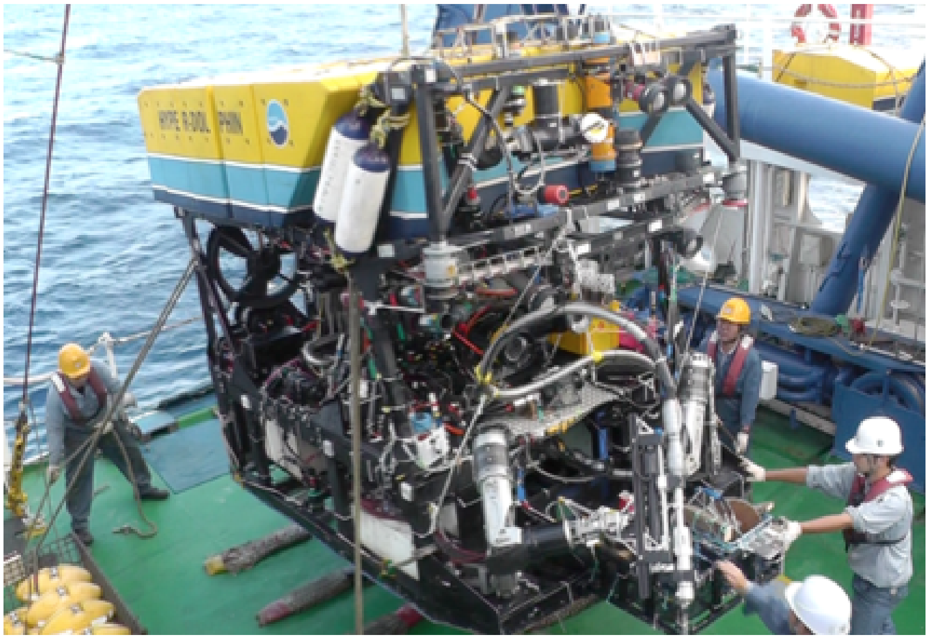

Figure A-3: Hyper-dolphin is a 3000 m rated ROV owned by the Japan Agency for Marine Earth Science and Technology. This ROV was used for sampling Mn-crusts and for deploying the CRC system.

A.2 ROV Hyper-dolphin

ROV Hyper-dolphin, shown in Fig. A-3, was used for surveys of Mn-crusts in the early stages of the survey (JAMSTEC n.d.). It is a 3000 m rated ROV owned by the Japan Agency for Marine Earth Science and Technology (JAMSTEC). Samples were collected using a drill and the robotic arms mounted on the ROV during several cruises (JAMSTEC 2009, 2011, 2012, 2013). These samples are used for validation of the proposed algorithms in chapter 4. This, however has the disadvantage of collecting samples which are easy to be snagged or broken.

The first version of the CRC system was mounted on the payload skid of Hyper-dolphin and conducted surveys along a Mn-crust ridge in 2013 (JAMSTEC 2013). This setup is shown in Fig. A-4. ROV has the advantage of real-time visual feedback to the researchers on the mother ship. However, it suffers from the errors due to manual piloting.

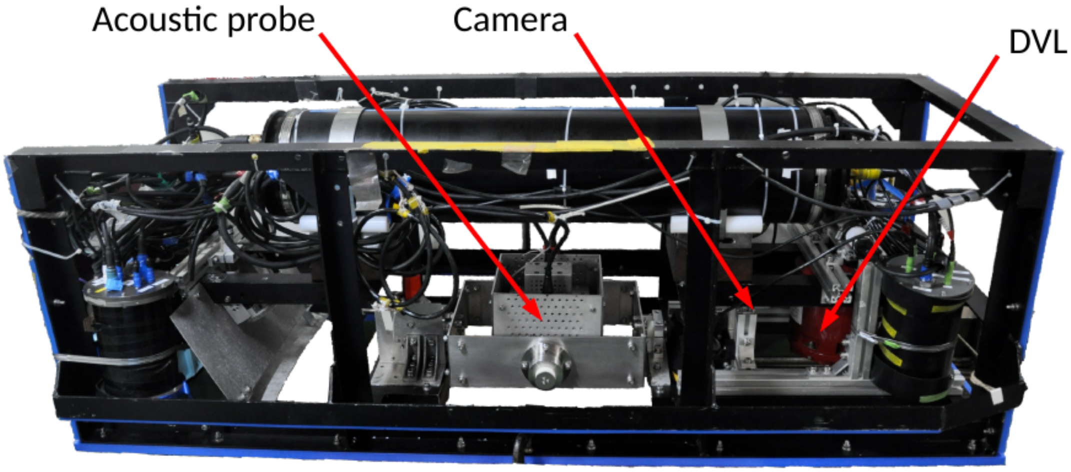

Figure A-4: The sensors were mounted on the ROV using a payload skid shown.

A.3 ROV Kaiko

Kaiko is a 6500 m rated ROV owned by JAMSTEC (Murashima et al. 2004). This was also used for sampling Mn-crusts in locations as deep as 5500 m; which were the deepest Mn-crusts ever detected. However, only samples close to the CRC survey locations is considered in the present research.

Appendix B

Press Release

Copy of the press release from Institute of Industrial Science, The University of Tokyo on the survey of Mn-crusts, which includes the proposed research, dated 2019 March 23 [url : https://www.iis.u-tokyo.ac.jp/ja/news/3079/].

東京大学
生産技術研究所
Institute of Industrial Science,
The University of Tokyo

2019.03.29 プレスリリース

【記者発表】世界初の大規模調査！３台のロボットが連携し、海底３次元画像を取得 ～コバルトリッチクラストの賦存状況の調査への貢献に期待～


航行型 AUV「AE2000f」

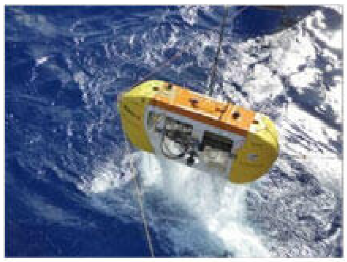
ホバリング型 AUV「BOSS-A」


ROV「QUASER9」

○発表者：

ソーントン ブレア（東京大学 生産技術研究所 准教授）

○発表のポイント：

◆航行型AUV「AE2000f」とROVを用いて、海底面の連続的な高高度３次元画像マッピングを行い、海底面の形状、底質、クラスト被覆状態、棲息生物などの情報を含むデータを、距離にして約７９km、面積にして１平方キロメートル分取得しました。

◆一部の領域では、クラスト賦存量調査を目的に開発されたホバリング型AUV「BOSS-A」を用いて、海底面の連続的な低高度３次元画像マッピングおよびクラスト音響厚み計測を同時に行い、距離にして１８.３km、面積約０.０３平方キロメートル分のデータを取得しました。

◆「BOSS-A」取得データの解析から、厚いクラストが連続的に分布すると推定された領域では、高高度３次元画像マッピングを実施し、広域かつ詳細なマルチレゾリューショナルなデータを取得しました。今後、統合解析により広範囲の正確なクラストの被覆率を算出することが期待されます。

○発表概要：

東京大学 生産技術研究所 ソーントン ブレア 准教授の研究チームは、独立行政法人 石油天然ガス・金属鉱物資源機構（JOGMEC）の委託（注１）を受け、コバルトリッチクラスト（以下、「クラスト」、注２）が分布する、南鳥島南西の拓洋第５海山において、１平方キロメートルにおよぶ面積の海底面の３次元画像を、航行型とホバリング型の２種類のAUV（Autonomous Underwater Vehicle:自律型海中ロボット（注３）およびROV（Remotely Operated vehicle: 遠隔操作無人探査機（注４）を用いて、短期間のうちに効率的に取得しました。

航行型AUV「AE2000f」（注５）に搭載した３次元画像マッピング装置（注６）、ホバリング型AUV「BOSS-A」（注７、注８）およびクラスト厚み計測装置（注９）は、東京大学 生産技術研究所が文部科学省の「海洋資源の利用促進に向けた基盤ツール開発プログラム」において、クラスト賦存量の計測を目的として平成２０年度から開発したもので、これまでも拓洋第５海山で調査を実施してきました。今回の調査で初めて大規模に実施し、非

常に多くの３次元画像データとクラスト厚みの連続データを取得することができました。

今回、面積にして１平方キロメートルにおよぶ、世界初の大規模な海底調査を達成したことで、クラストの被覆状況を効率的に調査できる手法を実現したといえます。また、得られたデータは、拓洋第５海山のクラスト賦存量を正確に推定するための基礎データになることが期待されます。

「AE2000f」に搭載された
３次元画像マッピング装置

東京大学 生産技術研究所が開発した音響厚み
計測装置の２００kHz パラメトリックプローブ

○発表内容：

拓洋第５海山の水深９００m～１,５００m程度の平頂部および肩部にかけての直線を主とする計画測線において、２０１８年１１月１３日～１２月４日の航海期間中（現場海域での調査実施期間：１１月１８日～２９日）、高高度３次元画像マッピング装置を搭載する航行型AUV「AE2000f」（昼間）とROV「QUASAR９（日本サルヴェージ株式会社所有）」（夜間）を用いた海底面の広域連続計測調査（１０m高度、計測幅１０m、cm分解能）、および低高度３次元画像マッピング装置と音響厚み計測装置を搭載するホバリング型AUV「BOSS-A」（昼間）を用いた海底面の詳細連続計測調査（２m高度、計測幅２m、mm分解能）を実施しました。

潜航回数は、「BOSS-A」は６回、「AE2000f」は５回、そしてROV「QUASAR9」は１１回です。

３台のロボット全体で、距離にして１３８km（BOSS-A: １８.３km、AE2000f: ７１.８km、ROV: ４７.９km）、面積にして約１平方キロメートル（BOSS-A:０.０３平方キロメートル、AE2000f: ０.７平方キロメートル、ROV: ０.３平方キロメートル）のデータを取得しました。

海山の南西の肩部にかけての測線を航走した「BOSS-A」の調査では、現場での３次元画像マッピングの解析結果から、計測場所ごとにクラスト分布の特徴に変化が見られました（図１、図２）。音響厚み計測装置のデータの計測結果から、連続的なクラストの被覆及び厚みが分かりました（図３）。

そこで、翌日の夜のROV調査では、クラストが被覆する箇所を調査するため、BOSS-Aの潜航測線と重なる測線を航走させる調査計画を立てました。写真に示すように、ROVが取得した高度１０mからの３次元画像データ（図４）は、BOSS-Aのデータ（図５）と重なる部分が見られます（図６）。今後、統合解析により、クラスト賦存量の推定をより正確にすることが期待されます。

また、BOSS-Aで撮られた画像に写っている生物はROVの画像にでもほぼ同じ位置に写っており、数時間・日ではほとんど動いていないことが分かります。このように、取得した３次元画像データは、クラストの厚みや被覆率を計測できるだけでなく、海底面の詳細な形状、底質そして棲息生物などの多元的な情報を含んでおり、環境影響評価調査などにも応用されることが期待されます。

○問い合わせ先：

東京大学 生産技術研究所
特任研究員　杉松 治美（すぎまつ はるみ）
Tel：03-5452-6487　Fax：03-5452-6489

○用語解説：

注１）JOGMEC委託事業

本調査は、２０１８年5月２５日にJOGMECが公募した委託事業「平成３０年度海洋鉱物資源調査に係るコバルトリッチクラスト賦存状況調査」を受託し実施した。JOGMECは経済産業省の委託を受け、コバルトリッチクラストの調査を実施している。

注２）コバルトリッチクラスト

鉄とマンガンの酸化物からなる海水起源の化学堆積岩。学術的にはマンガンクラスト、鉄マンガンクラストと呼ばれることが多い。海山や平頂海山などの海底において、数cm～１０数cmの厚さで基盤をカバーしており、広い範囲にわたって分布していることが知られている。コバルト（Co）、ニッケル、白金などを含んでいる。

注３）自律型海中ロボット（AUV：Autonomous Underwater Vehicle）

動力源を持ち、プロペラなどを用いてあらかじめ決められたルートに沿って無索で全自動で海中を観測する装置。

注４）遠隔操作無人探査機（ROV：Remotely Operated vehicle）

遠隔操縦式の探査機。ケーブルで探査機とオペレーションシステムがつながれており電力や各種指令を探査機に送り、海底の映像などの情報をリアルタイムで陸上や母船に伝送する。

注５）AE2000f

重量約３７０kgの中型航行型AUV。観測センサとして、高高度３次元画像マッピング装置を搭載する。

注６）３次元画像マッピング装置

海底の３次元画像マッピングを行う計測装置。カメラ、シート状のレーザおよびフラッシュの組み合わせにより構成され、AUVやROVに搭載して、ロボット側のナビゲーションセンサ情報により制御を行い、１.５～１０m程度の高度から海底面の高精度の３次元画像マップを作成することができる。ロボットにナビゲーションセンサが搭載されていいない場合には、別途つなげることが可能である。

注７）BOSS-A

重量約６００kgの中型ホバリング型AUV。観測センサとして、クラストの音響厚み計測装置と低高度３次元画像マッピング装置を搭載し、１.５m高度から全自動計測を行う。ペイロードスペースを広く取っているため、観測センサを入れ替えて別のセンサを搭載して別ミッションへの対応が可能である。

注８）ホバリング型AUV

広範囲を高速で航行することをミッションとする航行型AUVと異なり、運動自由度が高く、定点保持・その場回頭、その場での上下運動が可能なAUV。対象を詳細観測することを主要ミッションとする。

注９）クラスト厚み計測装置

「BOSS-A」には、ジンバル制御を行う音響厚み計測装置が搭載されている。パラメトリック効果で発する

２００kHz（２次波）の音響ビームを高度１～２mで海底面にビームの焦点を自動的に合わせる。ターゲットにあたるビームの直径は２０mm程度で、海底下３０cmまでの内部構造を計測できる。ジンバル制御により超音波が海底面に対して直角に入射するよう自動的に角度を制御する。

○添付資料：

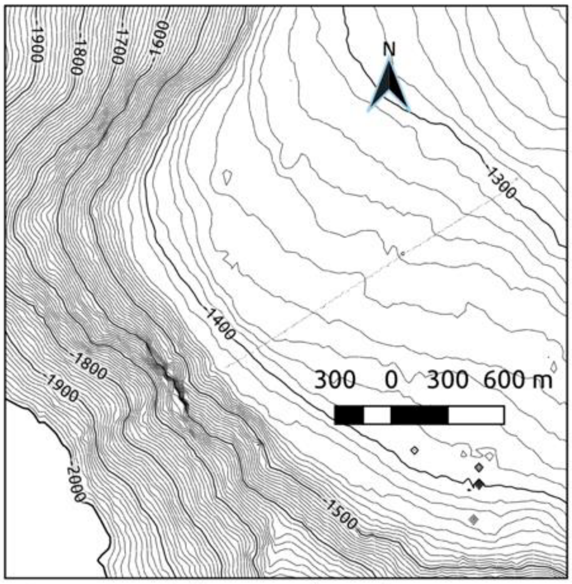

18TAKUYO5LA001 (L1 Transect) Waypoints

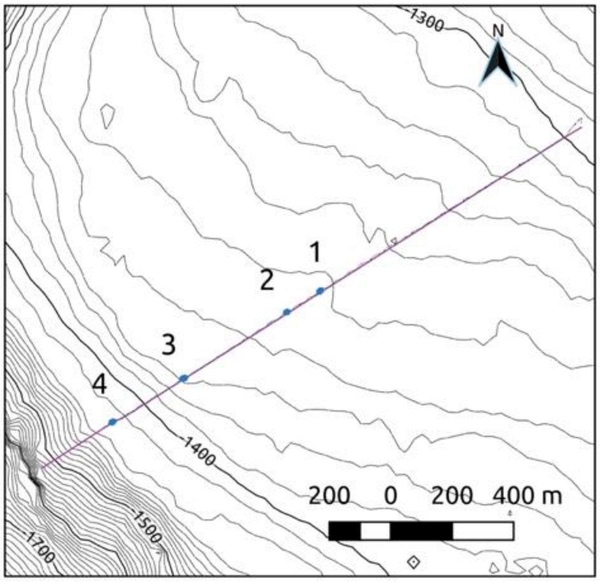

3D Reconstruction Top view

1. Sand and nodules

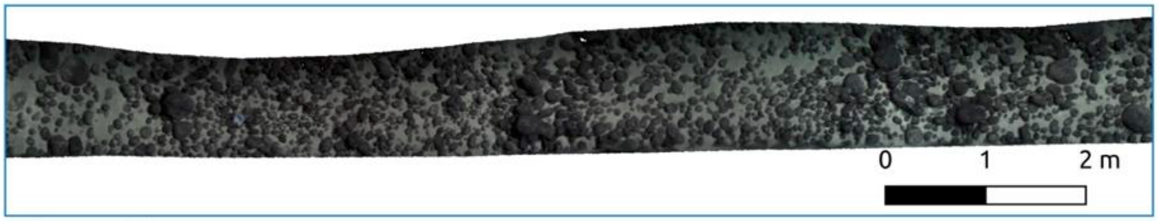

2. Bigger nodules

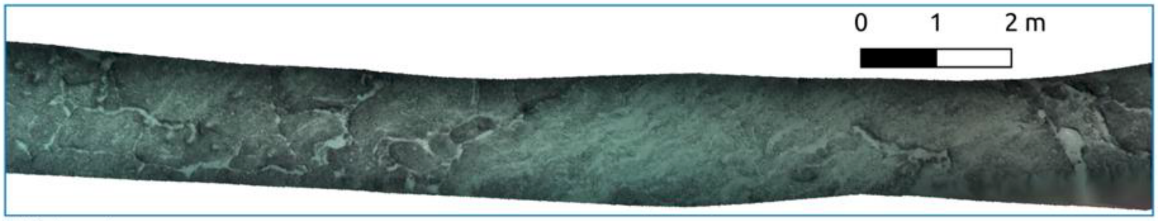

3. Flat crust

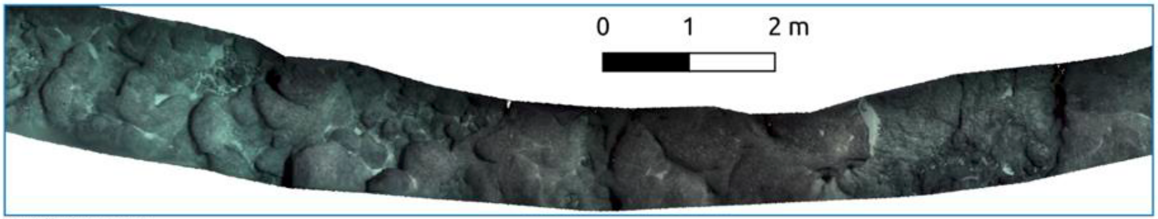

4. Pillowy crust

図１　海山の南西の肩部を下るBOSS-Aの調査では、場所毎にクラスト分布の特徴に変化が見られる。

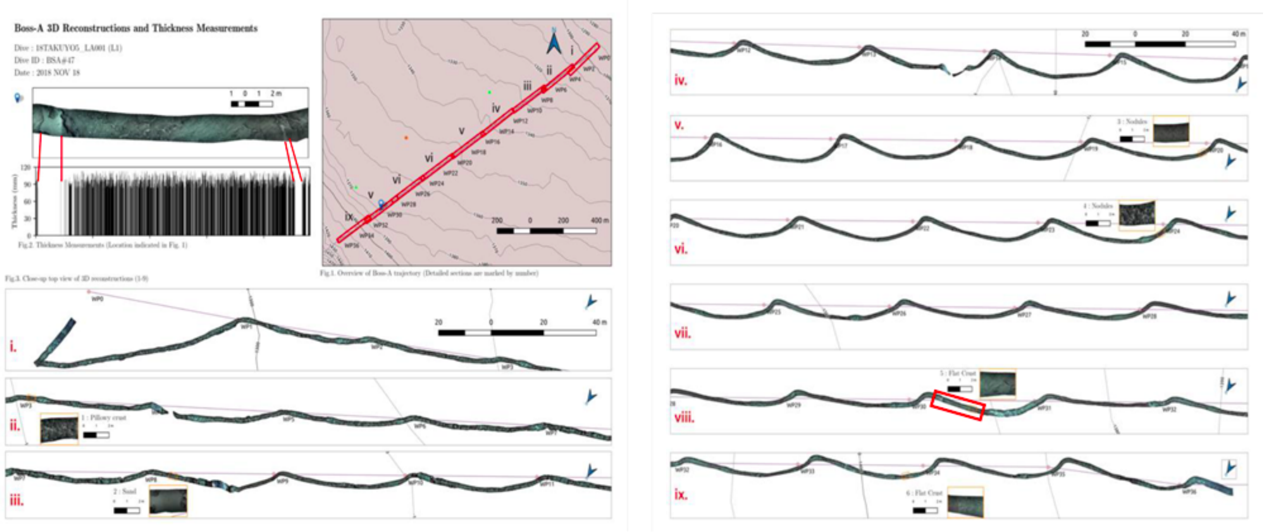

図２　BOSS-Aの計測測線と低高度３次元画像マッピングデータ。右図の枠で示すクラストが被覆する箇所について、クラストの厚み計測データの値を示す（左上の右図）。

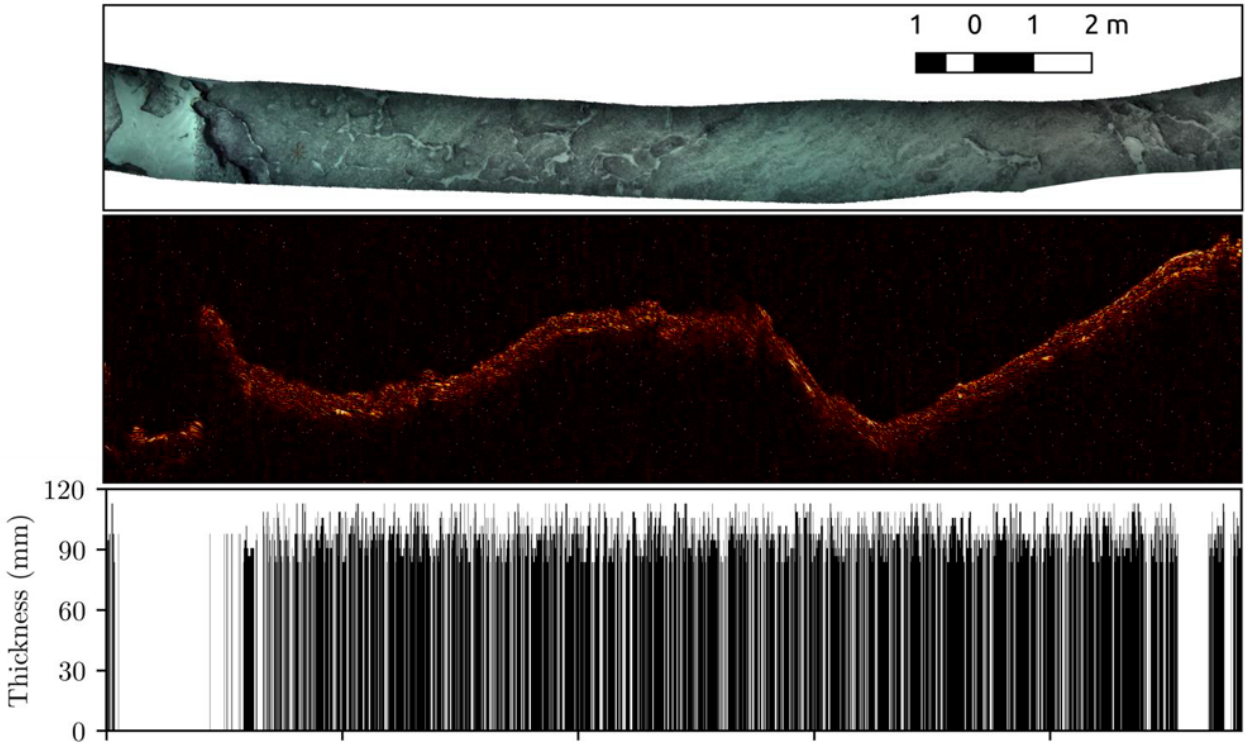

図３　図２の音響厚み計測データの拡大図、クラスト分布が連続する箇所（ロボットの計測時間軸に沿ったデータ表示）の拡大図（上図）、音響厚みデータ（中図）、音響厚み計測解析結果（下図）、音響厚み計測結果では砂地とクラスト被覆部の差がはっきりと示される。

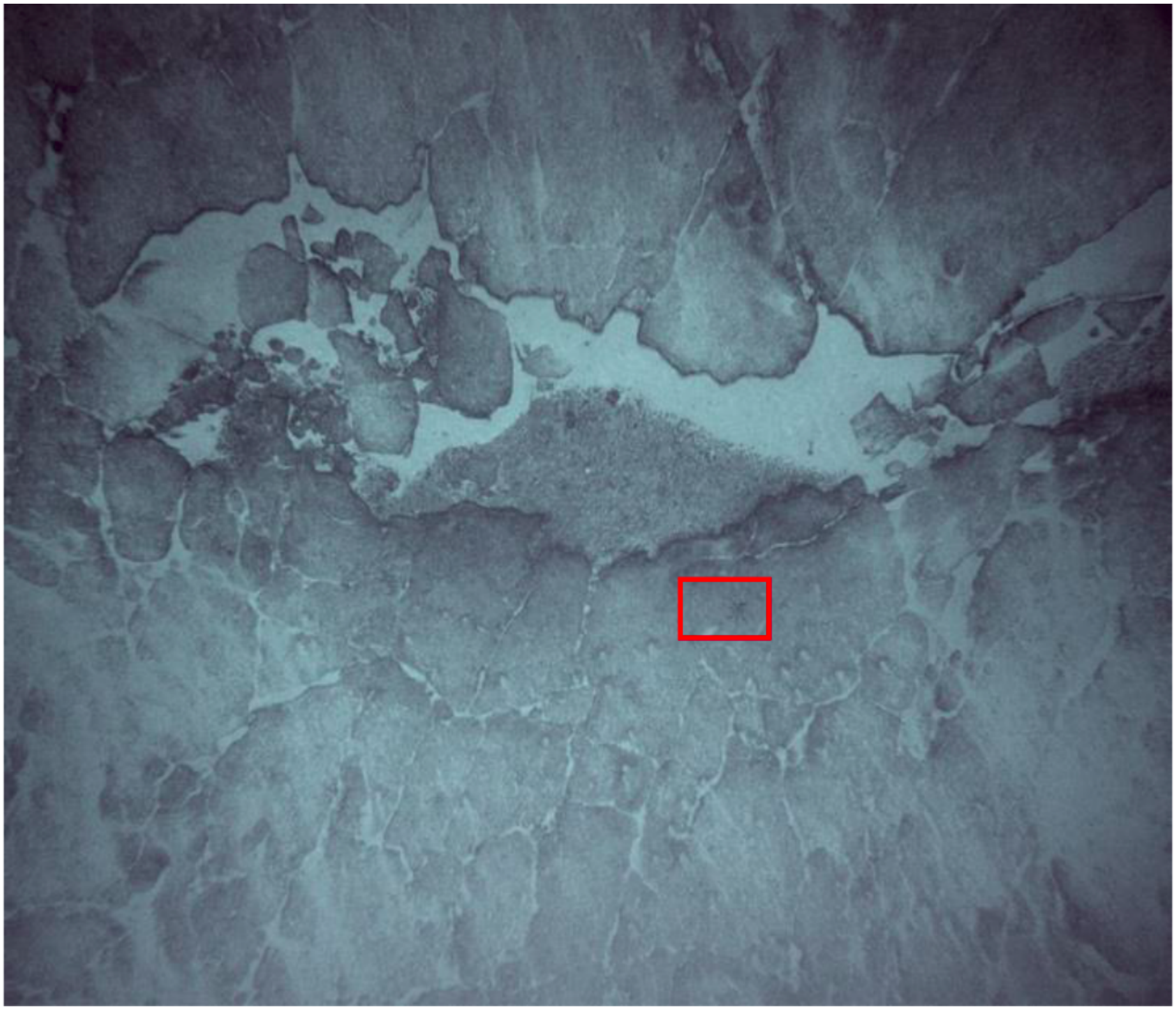

図４　BOSS-Aの調査と重なる測線を航走したROVの調査で取得したデータ。枠内に生物が写っている（図５、図６参照）。

図５　BOSS-Aの調査で取得したデータのうち、クラストが連続的に被覆する箇所のデータ。

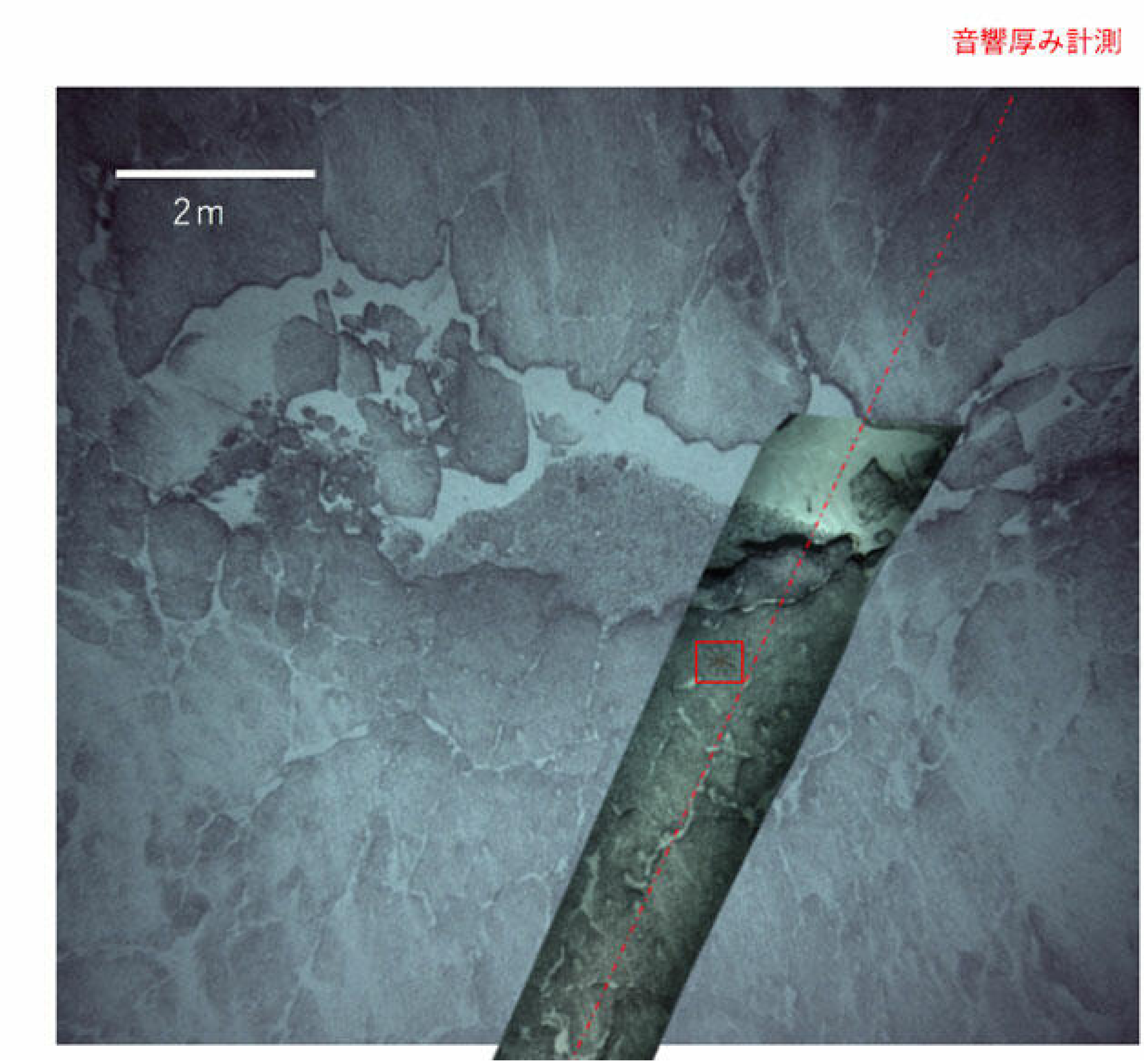

図６　図４と図５のデータはぴったりと重なる、また、両方の画像に写っている底生生物の位置はほとんど変わらない。

Acknowledgments

With hearty gratitude, I thank every being who directly or indirectly contributed to my research, career and life. Mentioning names is very difficult and often dangerous; I had many a hand helping me throughout these years. I may not thank them enough and this page will never be sufficient to list everyone.

I would start by thanking Prof. Kazuo Ishii, my thesis supervisor for his kind guidance. He had been patient and supportive. I thank Prof. Blair Thornton, my supervisor at the Institute of Industrial Science (IIS) of the University of Tokyo for his support. He had clear ideas about research and was hardworking. I thank Ms. Harumi Sugimatsu, senior researcher at IIS for her kind encouragement and support throughout. I also thank Kyushu Institute of Technology and IIS for providing the environment and support for my research that led to this PhD.

Dr. Mehul Sangekar, my friend and colleague guided me at critical points during this PhD. I thank Prof. Ito from the international student support group for her counseling. I thank him and all other colleagues and lab mates at the University of Tokyo and Kyushu Institute of Technology. I would also like to thank the staff at these institutions, especially Ms. Minegishi, Ms. Takenaga, Ms. Mizuguchi, Ms. Tanaka, and Ms. Shirahashi.

I thank the Hyper-Dolphin team, R/V Natsushima crew, R/V Yokosuka crew, and R/V Kairei crew, Japan Agency for Marine-Earth Science and Technology (JAMSTEC) during the NT13-13, KR16-01, and YK17-23C cruises. This work was supported by the Japanese Ministry of Education under the Program for the Development of Fundamental Tools for the Utilization of Marine Resources.

I extend my gratitude to my family and friends, both inside and outside the university for their emotional support and care.

Umesh Neettiyath
Kyushu Institute of Technology
February, 2020

Bibliography

Alevizos, E., Schoening, T., Koeser, K., Snellen, M. & Greinert, J. (2018), 'Quantification of the fine-scale distribution of Mn-nodules: insights from AUV multi-beam and optical imagery data fusion', *Biogeosciences Discussions* (February), 1–29.

Alonso, I., Yuval, M., Eyal, G., Treibitz, T. & Murillo, A. C. (2019), 'CoralSeg: Learning coral segmentation from sparse annotations', *Journal of Field Robotics* **36**(8), 1456–1477.
URL: *https://onlinelibrary.wiley.com/doi/abs/10.1002/rob.21915*

Aplin, A. C. & Cronan, D. S. (1985), 'Ferromanganese oxide deposits from the Central Pacific Ocean, II. Nodules and associated sediments', *Geochimica et Cosmochimica Acta* **49**(2), 437–451.
URL: *https://linkinghub.elsevier.com/retrieve/pii/0016703785900353*

Becker, J. J., Sandwell, D. T., Smith, W. H. F., Braud, J., Binder, B., Depner, J., Fabre, D., Factor, J., Ingalls, S., Kim, S.-H., Ladner, R., Marks, K., Nelson, S., Pharaoh, A., Trimmer, R., Von Rosenberg, J., Wallace, G. & Weatherall, P. (2009), 'Global Bathymetry and Elevation Data at 30 Arc Seconds Resolution: SRTM30_PLUS', *Marine Geodesy* **32**(4), 355–371.
URL: *http://www.tandfonline.com/doi/abs/10.1080/01490410903297766*

Bergstra, J. & Bengio, Y. (2012), 'Random search for hyper-parameter optimization', *The Journal of Machine Learning Research* **13**, 281–305.

Blidberg, D. R., Turner, R. M., Chappell, S. G., Blidberg D.R., R. M. T., Richard Blidberg, D., Turner, R. M. & Chappell, S. G. (1991), 'Autonomous underwater vehicles: Current activities and research opportunities', *Robotics and Autonomous Systems* **7**(2/3), 139–150.

URL: *http://linkinghub.elsevier.com/retrieve/pii/092188909190038M*

Bodenmann, A., Thornton, B., Nakajima, R. & Ura, T. (2017), 'Methods for quantitative studies of seafloor hydrothermal systems using 3D visual reconstructions', *ROBOMECH Journal* **4**(1), 22.

URL: *http://robomechjournal.springeropen.com/articles/10.1186/s40648-017-0091-5*

Bodenmann, A., Thornton, B. & Ura, T. (2012), '3D Seafoor Mapping With Automated Data Analysis', *Sea Technology* (October), 41–46.

Bodenmann, A., Thornton, B. & Ura, T. (2017), 'Generation of High-resolution Three-dimensional Reconstructions of the Seafloor in Color using a Single Camera and Structured Light', *Journal of Field Robotics* **34**(5), 833–851.

URL: *http://doi.wiley.com/10.1002/rob.21682*

Bongiorno, D. L., Bryson, M., Bridge, T. C. L., Dansereau, D. G. & Williams, S. B. (2018), 'Coregistered Hyperspectral and Stereo Image Seafloor Mapping from an Autonomous Underwater Vehicle', *Journal of Field Robotics* **35**(3), 312–329.

URL: *http://doi.wiley.com/10.1002/rob.21713*

Brown, C. J., Smith, S. J., Lawton, P. & Anderson, J. T. (2011), 'Benthic habitat mapping: A review of progress towards improved understanding of the spatial ecology of the seafloor using acoustic techniques', *Estuarine, Coastal and Shelf Science* **92**(3), 502–520.

URL: *http://dx.doi.org/10.1016/j.ecss.2011.02.007*

Bunchuk, A. V., Vovk, A. E., Esipov, I. B. & K, M. E. (1995), 'Determination of acoustic parameters of manganese crusts and nodules.', *Oceanology* **35**(1), 140–142.

Capocci, R., Dooly, G., Omerdić, E., Coleman, J., Newe, T. & Toal, D. (2017), 'Inspection-Class Remotely Operated Vehicles—A Review', *Journal of Marine Science and Engineering* **5**(1), 13.

Caruana, R. & Niculescu-Mizil, A. (2006), An empirical comparison of supervised learning algorithms, *in* 'Proceedings of the 23rd international conference on Machine learning - ICML '06', ACM Press, New York, New York, USA, pp. 161–168.

Chakraborty, B., Kodagali, V. & Baracho, J. (2003), 'Sea-floor classification using multibeam echo-sounding angular backscatter data: a real-time approach employing hybrid neural network architecture', *IEEE Journal of Oceanic Engineering* **28**(1), 121–128.
URL: *http://ieeexplore.ieee.org/document/1190141/*

Chakraborty, B. & Paula, D. (n.d.), 'Understanding seafloor morphology using remote high frequency acoustic methods : an appraisal to modern techniques and its effectiveness', pp. 179–183.

Clark, M. R., Heydon, R., Hein, J. R., Petersen, S., Rowden, A., Smith, S., Baker, E. & Beaudoin, Y. (2013), *Deep Sea Minerals: Cobalt-rich Ferromanganese Crusts, a physical, biological, environmental, and technical review*, Secretariat of the Pacific Community.
URL: *http://dsm.gsd.spc.int/public/files/meetings/TrainingWorkshop4/UNEP_vol1C.pdf*

Corliss, J. B., Dymond, J., Gordon, L. I., Edmond, J. M., von Herzen, R. P., Ballard, R. D., Green, K., Williams, D., Bainbridge, A., Crane, K. & van Andel, T. H. (1979), 'Submarine Thermal Springs on the Galápagos Rift', *Science* **203**(4385), 1073–1083.
URL: *http://www.sciencemag.org/lookup/doi/10.1126/science.203.4385.1073*

Cressie, N. (1990), 'The origins of kriging', *Mathematical Geology* **22**(3), 239–252.
URL: *http://link.springer.com/10.1007/BF00889887*

Du, D., Ren, X., Yan, S., Shi, X., Liu, Y. & He, G. (2017), 'An integrated method for the quantitative evaluation of mineral resources of cobalt-rich crusts on seamounts', *Ore Geology Reviews* **84**, 174–184.
URL: *http://dx.doi.org/10.1016/j.oregeorev.2017.01.011*

Du, D., Wang, C., Du, X., Yan, S., Ren, X., Shi, X. & Hein, J. R. (2017), 'Distance-gradient-based variogram and Kriging to evaluate cobalt-rich crust deposits on seamounts', *Ore Geology Reviews* **84**, 218–227.
URL: *http://dx.doi.org/10.1016/j.oregeorev.2016.12.028*

Du, D., Yan, S., Yang, F., Zhu, Z., Song, Q. & Yang, G. (2018), 'Kriging interpolation for evaluating the mineral resources of cobalt-rich crusts on magellan seamounts', *Minerals* **8**(9), 9–16.

Friedman, A. (2013), Automated interpretation of benthic stereo imagery, PhD thesis, The University of Sydney.
URL: *http://hdl.handle.net/2123/9438*

Gaowen, H., Donghong, L., Chengbin, S., Xiaoming, S., Shuigen, W., Jianping, Z. & Xuehua, Z. (2005), 'An effective method to determine the distribution boundary of cobalt-rich Fe-Mn crusts on a guyot: Synchronous application of Sub-bottom Profiling and Deep-Sea Video Recording', *Journal of China University of Biosciences* **16**(June), 178–182.

Glasby, G. P., Li, J. & Sun, Z. (2015), 'Deep-Sea Nodules and Co-rich Mn Crusts', *Marine Georesources & Geotechnology* **33**(1), 72–78.
URL: *http://www.tandfonline.com/doi/abs/10.1080/1064119X.2013.784838*

Gomes-Pereira, J. N., Auger, V., Beisiegel, K., Benjamin, R., Bergmann, M., Bowden, D., Buhl-Mortensen, P., De Leo, F. C., Dionísio, G., Durden, J. M., Edwards, L., Friedman, A., Greinert, J., Jacobsen-Stout, N., Lerner, S., Leslie, M., Nattkemper, T. W., Sameoto, J. A., Schoening, T., Schouten, R., Seager, J., Singh, H., Soubigou, O., Tojeira, I., van den Beld, I., Dias, F., Tempera, F. & Santos, R. S.

(2016), ‘Current and future trends in marine image annotation software’, *Progress in Oceanography* .

URL: *http://linkinghub.elsevier.com/retrieve/pii/S0079661116301240*

Halbach, P., Pracejus, B. & Maerten, A. (1993), ‘Geology and mineralogy of massive sulfide ores from the central Okinawa Trough, Japan’, *Economic Geology* **88**(8), 2210–2225.

URL: *http://pubs.geoscienceworld.org/economicgeology/article/88/8/2210/21260/Geology-and-mineralogy-of-massive-sulfide-ores*

Hamilton, L. J. & Parnum, I. (2011), ‘Acoustic seabed segmentation from direct statistical clustering of entire multibeam sonar backscatter curves’, *Continental Shelf Research* **31**(2), 138–148.

URL: *http://dx.doi.org/10.1016/j.csr.2010.12.002*

Hari, V. N., Kalyan, B., Chitre, M. & Ganesan, V. (2018), ‘Spatial Modeling of Deep-Sea Ferromanganese Nodules With Limited Data Using Neural Networks’, *IEEE Journal of Oceanic Engineering* **43**(4), 997–1014.

URL: *https://ieeexplore.ieee.org/document/8081801/*

Hashimoto, J., Ohta, S., Gamo, T., Chiba, H., Yamaguchi, T., Tsuchida, S., Okudaira, T., Watabe, H., Yamanaka, T. & Kitazawa, M. (2001), ‘First Hydrothermal Vent Communities from the Indian Ocean Discovered’, *Zoological Science* **18**(5), 717–721.

URL: *http://www.bioone.org/doi/abs/10.2108/zsj.18.717*

He, G., Ma, W., Song, C., Yang, S., Zhu, B., Yao, H., Jiang, X. & Cheng, Y. (2011), ‘Distribution characteristics of seamount cobalt-rich ferromanganese crusts and the determination of the size of areas for exploration and exploitation’, *Acta Oceanologica Sinica* **30**(3), 63–75.

URL: *http://link.springer.com/10.1007/s13131-011-0120-9*

Hein, J. R., Mizell, K., Koschinsky, A. & Conrad, T. A. (2013), ‘Deep-ocean mineral deposits as a source of critical metals for high- and green-technology applications:

Comparison with land-based resources', *Ore Geology Reviews* **51**, 1–14.
URL: *http://dx.doi.org/10.1016/j.oregeorev.2012.12.001 https://linkinghub.elsevier.com/retrieve/pii/S016913681200234X*

Hodkinson, R. & Cronan, D. (1991), 'Regional and depth variability in the composition of cobalt-rich ferromanganese crusts from the SOPAC area and adjacent parts of the central equatorial Pacific', *Marine Geology* **98**(2-4), 437–447.
URL: *https://linkinghub.elsevier.com/retrieve/pii/002532279190115K*

Hong, F., Feng, H., Huang, M. & Wang, B. (2019), An effective method for measuring the thickness of Cobalt-rich Manganese Crust based on the neighborhood information and dual- channel information, *in* '23rd International Congress on Acoustics', number September, Aachen, Germany, pp. 4446–4453.

Hong, Feng, Huang, Wang & Xia (2019), 'China's First Demonstration of Cobalt-rich Manganese Crust Thickness Measurement in the Western Pacific with a Parametric Acoustic Probe', *Sensors* **19**(19), 4300.

Institute of Industrial Science (2019), 2019.03.29, Technical report.
URL: *https://www.iis.u-tokyo.ac.jp/ja/news/3079/%0A*

International Seabed Authority (2012), 'Regulations on Prospecting and Exploration for Cobalt-rich Ferromanganese Crusts in the Area'.

ISBA (2018), 'International seabed authority reaches milestone; makes decisions : 19th session round up'.
URL: *https://www.isa.org.jm/news/international-seabed-authority-reaches-milestone-makes-decisions- 19th-session-round*

Jackson, D. R. & Richardson, M. D. (2007), *High-Frequency Seafloor Acoustics.*

JAMSTEC (2009), R / V Natsushima Cruise Report NT09-02Leg2, Technical report, JAMSTEC.
URL: *http://www.godac.jamstec.go.jp/catalog/doc_catalog/metadataDisp/NT09-02_leg2_all?lang=en*

JAMSTEC (2011), R / V Natsushima Cruise Report NT10-11, Technical report, JAMSTEC.
URL: *http://www.godac.jamstec.go.jp/catalog/doc_catalog/metadataDisp/NT10-11_all?lang=en*

JAMSTEC (2012), R / V Natsushima cruise report NT12-05, Technical report, JAMSTEC.
URL: *http://www.godac.jamstec.go.jp/catalog/doc_catalog/metadataDisp/NT12-05_all?lang=en*

JAMSTEC (2013), R / V Natsushima Cruise Report NT13-13, Technical report, JAMSTEC, Japan Agency for Marin-Earth Science and Technology, Yokosuka.
URL: *http://www.godac.jamstec.go.jp/catalog/doc_catalog/metadataDisp/NT13-13_all?lang=en*

JAMSTEC (n.d.), '4,500 m Class Remotely Operated Vehicle HYPER-DOLPHIN'.
URL: *https://www.jamstec.go.jp/e/about/equipment/ships/hyperdolphin.html*

Jones, D. O., Amon, D. J. & Chapman, A. S. (2018), 'Mining deep-ocean mineral deposits: What are the ecological risks?', *Elements* **14**(5), 325–330.

Joo, J., Kim, S. S., Choi, J. W., Pak, S. J., Ko, Y., Son, S. K., Moon, J. W. & Kim, J. (2020), 'Seabed mapping using shipboard multibeam acoustic data for assessing the spatial distribution of ferromanganese crusts on seamounts in the western pacific', *Minerals* **10**(2), 1–20.

Kalyan, B., Ganesan, V., Chitre, M. & Vishnu, H. (2017), Optimal point planning for abundance estimation of polymetallic nodules, *in* 'Oceans 2017 - Anchorage', number 978, Anchorage, AK, pp. 1–6.

Kubat, M. (2015), *An Introduction to Machine Learning*, Springer International Publishing Switzerland.
URL: *http://link.springer.com/10.1007/978-3-319-20010-1*

Kusumam, K., Krajník, T., Pearson, S., Duckett, T. & Cielniak, G. (2017), '3D-vision based detection, localization, and sizing of broccoli heads in the field', *Journal of Field Robotics* **34**(8), 1505–1518.
URL: *http://doi.wiley.com/10.1002/rob.21726*

Lim, J. W. (2017), Automated Interpretation of Seafloor 3D Visual Mapping Data Obtained Using Underwater Robots, PhD thesis, university of southampton.
URL: *http://eprints.soton.ac.uk/14102/*

Lodge, M. W. & Verlaan, P. A. (2018), 'Deep-Sea Mining: International Regulatory Challenges and Responses', *Elements* **14**(5), 331–336.
URL: *https://pubs.geoscienceworld.org/msa/elements/article/14/5/331/559116/DeepSea-Mining-International-Regulatory-Challenges*

Lüdtke, A., Jerosch, K., Herzog, O. & Schlüter, M. (2012), 'Development of a machine learning technique for automatic analysis of seafloor image data: Case example, Pogonophora coverage at mud volcanoes', *Computers & Geosciences* **39**, 120–128.
URL: *https://linkinghub.elsevier.com/retrieve/pii/S009830041100224X*

Lusty, P. A. J., Hein, J. R. & Josso, P. (2018), 'Formation and Occurrence of Ferromanganese Crusts: Earth's Storehouse for Critical Metals', *Elements* **14**(5), 313–318.
URL: *https://pubs.geoscienceworld.org/msa/elements/article/14/5/313/559108/Formation-and-Occurrence-of-Ferromanganese-Crusts*

Lusty, P. A. J. & Murton, B. J. (2018), 'Deep-Ocean Mineral Deposits: Metal Resources and Windows into Earth Processes', *Elements* **14**(5), 301–306.
URL: *https://pubs.geoscienceworld.org/msa/elements/article/14/5/301/559105/DeepOcean-Mineral-Deposits-Metal-Resources-and*

Marcos, M. S. A. C., Soriano, M. N. & Saloma, C. A. (2005), 'Classification of coral reef images from underwater video using neural networks', *Optics Express* **13**(22), 8766–8771.
URL: *https://www.osapublishing.org/oe/abstract.cfm?uri=oe-13-22-8766*

Mehta, A., Ribeiro, E., Gilner, J. & Woesik, R. V. (2007), Coral reef texture classification using support vector machines, *in* 'Proceedings of the Second International Conference on Computer Vision Theory and Applications', Vol. 2, SciTePress - Science and and Technology Publications, Barcelona, Spain, pp. 302–305.
URL: *https://dblp.org/rec/bib/conf/visapp/MehtaRGW07 http://www.scitepress.org/DigitalLibrary/Link.aspx?doi=10.5220/0002062303020305*

Micallef, A., Krastel, S. & Savini, A., eds (2018), *Submarine Geomorphology*, Springer Geology, Springer International Publishing, Cham.
URL: *http://link.springer.com/10.1007/978-3-319-57852-1*

Michel, J. & Ballard, R. (n.d.), The RMS Titanic 1985 discovery expedition, *in* 'Proceedings of OCEANS'94', Vol. 3, IEEE, pp. III/132–III/137.
URL: *http://ieeexplore.ieee.org/document/364185/*

Miller, K. A., Thompson, K. F., Johnston, P. & Santillo, D. (2018), 'An overview of seabed mining including the current state of development, environmental impacts, and knowledge gaps', *Frontiers in Marine Science* **4**(JAN).

Murashima, T., Nakajoh, H., Yoshida, H., Yamauchi, N. & Sezoko, H. (2004), 7,000m class ROV KAIKO7000, *in* 'Oceans '04 MTS/IEEE Techno-Ocean '04 (IEEE Cat. No.04CH37600)', Vol. 2, IEEE, pp. 812–817.
URL: *http://ieeexplore.ieee.org/document/1405558/*

Neettiyath, U., Sato, T., Sangekar, M., Bodenmann, A., Thornton, B., Ura, T. & Asada, A. (2015), Identification of manganese crusts in 3D visual reconstructions to filter geo-registered acoustic sub-surface measurements, *in* 'Oceans 2015 - MTS/IEEE Washington', IEEE, pp. 1–6.
URL: *http://ieeexplore.ieee.org/document/7404471/*

Neettiyath, U., Thornton, B., Sangekar, M., Ishii, K., Sato, T., Bodenmann, A. & Ura, T. (2017), Automatic Extraction of Thickness Information from Sub-Surface Acoustic Measurements of Manganese Crusts, *in* 'Oceans 2017 - Aberdeen', IEEE,

pp. 1–7.
URL: *http://ieeexplore.ieee.org/document/8084917/*

Neettiyath, U., Thornton, B., Sangekar, M., Nishida, Y., Ishii, K., Sato, T., Bodenmann, A. & Ura, T. (2019), An AUV Based Method for Estimating Hectare-scale Distributions of Deep Sea Cobalt-rich Manganese Crust Deposits, *in* 'OCEANS 2019 - Marseille', IEEE, Marseilles, pp. 1–6.
URL: *https://ieeexplore.ieee.org/document/8867481/*

Nishida, Y., Nagahashi, K., Sato, T., Bodenmann, A., Thornton, B., Asada, A. & Ura, T. (2016), 'Autonomous Underwater Vehicle "BOSS-A" for Acoustic and Visual Survey of Manganese Crusts', *Journal of Robotics and Mechatronics* **28**(1), 91–94.
URL: *doi: 10.20965/jrm.2016.p0091 https://www.fujipress.jp/jrm/rb/robot002800010091/ https://www.fujipress.jp/jrm/rb/robot002800010091*

Otsu, N. (1979), 'A Threshold Selection Method from Gray-Level Histograms', *IEEE Transactions on Systems, Man, and Cybernetics* **9**(1), 62–66.
URL: *http://ieeexplore.ieee.org/lpdocs/epic03/wrapper.htm?arnumber=4310076 http://ieeexplore.ieee.org/document/4310076/*

Pedregosa, F., Varoquaux, G., Gramfort, A., Michel, V., Thirion, B., Grisel, O., Blondel, M., Müller, A., Nothman, J., Louppe, G., Prettenhofer, P., Weiss, R., Dubourg, V., Vanderplas, J., Passos, A., Cournapeau, D., Brucher, M., Perrot, M. & Duchesnay, É. (2011), 'Scikit-learn: Machine Learning in Python', *Journal of Machine Learning Research* **12**, 2825–2830.
URL: *http://arxiv.org/abs/1201.0490*

Ramirez-Llodra, E., Shank, T. M. & German, C. R. (2007), 'Biodiversity and Biogeography of Hydrothermal Vent Species: Thirty Years of Discovery and Investigations', *Oceanography* **20**(1), 30–41.
URL: *https://www.jstor.org/stable/24859973*

Sato, T., Thornton, B., Bodenmann, A., Asada, A. & Ura, T. (2013), Towards real-time control of a double gimbaled acoustic probe for measurement of manganese crusts thickness, *in* '2013 IEEE International Underwater Technology Symposium (UT)', IEEE, pp. 1–5.
URL: *http://ieeexplore.ieee.org/document/6519880/*

Schoening, T., Bergmann, M. & Nattkemper, T. W. (2012), Investigation of hidden parameters influencing the automated object detection in images from the deep seafloor of the HAUSGARTEN observatory, *in* 'Oceans 2012 - MTS/IEEE Hampton Roads', IEEE, pp. 1–5.
URL: *http://ieeexplore.ieee.org/document/6405040/*

Schoening, T., Jones, D. O. B. & Greinert, J. (2017), 'Compact-Morphology-based poly-metallic Nodule Delineation', *Scientific Reports* **7**(1), 13338–13349.
URL: *http://dx.doi.org/10.1038/s41598-017-13335-x http://www.nature.com/articles/s41598-017-13335-x*

Stehman, S. V. (1997), 'Selecting and interpreting measures of thematic classification accuracy', *Remote Sensing of Environment* **62**(1), 77–89.
URL: *https://linkinghub.elsevier.com/retrieve/pii/S0034425797000837*

Stokes, M. D. & Deane, G. B. (2009), 'Automated processing of coral reef benthic images', *Limnology and Oceanography: Methods* **7**(2), 157–168.
URL: *http://doi.wiley.com/10.4319/lom.2009.7.157*

Takaya, Y., Yasukawa, K., Kawasaki, T., Fujinaga, K., Ohta, J., Usui, Y., Nakamura, K., Kimura, J. I., Chang, Q., Hamada, M., Dodbiba, G., Nozaki, T., Iijima, K., Morisawa, T., Kuwahara, T., Ishida, Y., Ichimura, T., Kitazume, M., Fujita, T. & Kato, Y. (2018), 'The tremendous potential of deep-sea mud as a source of rare-earth elements', *Scientific Reports* **8**(1), 1–8.
URL: *http://dx.doi.org/10.1038/s41598-018-23948-5*

Thornton, B., Asada, A., Bodenmann, A., Sangekar, M. & Ura, T. (2013), 'Instruments and methods for acoustic and visual survey of manganese crusts', *IEEE Journal of Oceanic Engineering* **38**(1), 186–203.

Thornton, B., Asada, A., Ura, T., Ohira, K. & Kirimura, D. (2010), 'The development of an acoustic probe to measure the thickness of ferro-manganese crusts', *OCEANS'10 IEEE Sydney, OCEANSSYD 2010* .

Thornton, B., Bodenmann, A., Asada, A., Ura, T., Sangekar, M., Ohira, K. & Kirimura, D. (2011), Acoustic and visual survey of manganese crusts using an underwater vehicle at #5 Takuyo seamount, *in* '2011 IEEE Symposium on Underwater Technology and Workshop on Scientific Use of Submarine Cables and Related Technologies', IEEE, pp. 1–9.
URL: *http://ieeexplore.ieee.org/document/5774098/*

Thornton, B., Takahashi, T., Sato, T., Sakka, T., Tamura, A., Matsumoto, A., Nozaki, T., Ohki, T. & Ohki, K. (2015), 'Development of a deep-sea laser-induced breakdown spectrometer for in situ multi-element chemical analysis', *Deep Sea Research Part I: Oceanographic Research Papers* **95**, 20–36.
URL: *http://dx.doi.org/10.1016/j.dsr.2014.10.006 https://linkinghub.elsevier.com/retrieve/pii/S0967063714001897*

Thornton, B., Ura, T., Sangekar, M. & Ohira, K. (2009), 'A case study to demonstrate remote acoustic measurement of ferro-manganese crust thickness', *Ocean Engineering Symposium* .

Unpingco, J. (2016), *Python for Probability, Statistics, and Machine Learning*, Springer International Publishing, Cham.
URL: *http://link.springer.com/10.1007/978-3-319-30717-6*

Usui, A., Graham, I. J., Ditchburn, R. G., Zondervan, A., Shibasaki, H. & Hishida, H. (2007), 'Growth history and formation environments of ferromanganese deposits on the Philippine Sea Plate, northwest Pacific Ocean', *Island Arc* **16**(3), 420–430.
URL: *http://doi.wiley.com/10.1111/j.1440-1738.2007.00592.x*

Usui, A., Nishi, K., Sato, H., Nakasato, Y., Thornton, B., Kashiwabara, T., Tokumaru, A., Sakaguchi, A., Yamaoka, K., Kato, S., Nitahara, S., Suzuki, K., Iijima, K. & Urabe, T. (2017), 'Continuous growth of hydrogenetic ferromanganese crusts since 17 Myr ago on Takuyo-Daigo Seamount, NW Pacific, at water depths of 800–5500 m', *Ore Geology Reviews* **87**, 71–87.
URL: *http://dx.doi.org/10.1016/j.oregeorev.2016.09.032 https://linkinghub.elsevier.com/retrieve/pii/S0169136816302062*

Usui, A. & Someya, M. (1997), 'Distribution and composition of marine hydrogenetic and hydrothermal manganese deposits in the northwest Pacific', *Geological Society, London, Special Publications* **119**(1), 177–198.
URL: *http://sp.lyellcollection.org/cgi/doi/10.1144/GSL.SP.1997.119.01.12 http://sp.lyellcollection.org/lookup/doi/10.1144/GSL.SP.1997.119.01.12*

Wakita, N. (2010), 'Development of Autonomous Underwater Vehicle (AUV) for Exploring Deep Sea Marine Mineral Resources', *Mitsubishi Heavy Industries Technical Review* **47**(3), 73–80.

Wessel, P., Sandwell, D. & Kim, S.-S. (2010), 'The Global Seamount Census', *Oceanography* **23**(01), 24–33.
URL: *https://tos.org/oceanography/article/the-global-seamount-census*

Weydert, M. (1991), 'Design of a system to assess manganese nodule resources acoustically', *Ultrasonics* **29**(2), 150–158.
URL: *https://linkinghub.elsevier.com/retrieve/pii/0041624X9190045A*

Weydert, M. M. P. (1985), 'Measurements of the acoustic backscatter of manganese nodules', *The Journal of the Acoustical Society of America* **78**(6), 2115–2121.
URL: *http://asa.scitation.org/doi/10.1121/1.392671*

Weydert, M. M. P. (1990), 'Measurements of the acoustic backscatter of selected areas of the deep seafloor and some implications for the assessment of manganese nodule resources', *The Journal of the Acoustical Society of America* **88**(1), 350–366.
URL: *http://asa.scitation.org/doi/10.1121/1.399910*

XPRIZE, S. O. D. (2019), 'DISCOVERING THE MYSTERIES OF THE DEEP SEA'.
URL: *https://oceandiscovery.xprize.org/prizes/ocean-discovery*

Yamazaki, T. & Sharma, R. (1998), 'Distribution characteristics of co-rich manganese deposits on a seamount in the central Pacific Ocean', *Marine Georesources & Geotechnology* **16**(4), 283–305.
URL: *http://www.tandfonline.com/doi/abs/10.1080/10641199809379973*

Yamazaki, T., Sharma, R. & Tsurusaki, K. (1994), 'Microtopographic analysis of cobalt-rich manganese deposits on a mid-pacific seamount', *Marine Georesources & Geotechnology* **12**(1), 33–52.
URL: *https://doi.org/10.1080/10641199409388252 http://www.tandfonline.com/doi/abs/10.1080/10641199409388252*

Yeo, I. A., Dobson, K., Josso, P., Pearce, R. B., Howarth, S. A., Lusty, P. A. J., Bas, T. P. L. & Murton, B. J. (2018), 'Assessment of the Mineral Resource Potential of Atlantic Ferromanganese Crusts Based on Their Growth History, Microstructure, and Texture', *Minerals* **8**(8), 1–19.
URL: *http://www.mdpi.com/2075-163X/8/8/327*

Yoshino, S., Thornton, B., Takahashi, T., Takaya, Y. & Nozaki, T. (2018), 'Signal preprocessing of deep-sea laser-induced plasma spectra for identification of pelletized hydrothermal deposits using Artificial Neural Networks', *Spectrochimica Acta - Part B Atomic Spectroscopy* **145**, 1–7.
URL: *https://doi.org/10.1016/j.sab.2018.03.015*

Good judgment comes from experience, and a lot of that comes from bad judgment.

-Will Rogers

The real voyage of discovery consists not in seeking new landscapes, but in having new eyes.

-Marcel Proust

Now the words are over
and the pain they bring is gone.
Now you have gone to rest
in the arms of the Beloved.

-Rumi